A COMPARISON OF ELECTRON-PROTON AND POSITRON-PROTON ELASTIC SCATTERING AT FOUR-MOMENTUM TRANSFERS UP TO 5.0 (GeV/c)^2

Thesis by

Jerry Mar

In Partial Fulfillment of the Requirements

For the Degree of

Doctor of Philosophy

California Institute of Technology

Pasadena, California

1969

(Submitted July 18, 1968)

ACKNOWLEDGMENTS

I wish to thank Drs. Jerry Pine and Barry Barish of the Caltech Users Group; Drs. Hobey DeStaebler, Dave Coward, John Litt, Adolph Minten* and Dick Taylor of the Stanford Linear Accelerator Center; and Marty Breidenbach of the Massachusetts Institute of Technology - people who were vital in making this experiment a success. I would in particular like to thank Drs. Pine and Barish for providing constant encouragement, physical assistance and dependable advice.

Invaluable assistance was also provided by Dr. Henry Kendall and Paul Kirk of M.I.T., Stewart Loken of Caltech, as well as Ed Taylor and the other members of the Spectrometer Group at SLAC.

Special thanks go out to Roger Miller of SLAC, who expertly and with great persistence, provided the positron beam.

I would also like to thank Keith Doty and Dick Early of SLAC for assisting before and after the experiment, as well as Phyllis Nilsson and Bill Peterson, who assisted in the data analysis.

The financial support of the U.S. Atomic Energy Commission and the National Research Council of Canada is gratefully acknowledged.

---

*Present address: CERN, Geneva, Switzerland.

ABSTRACT

A comparison of elastic electron-proton and positron-proton scattering has been made at eight different values of 4-momentum transfer squared, ranging from 0.20 to 5.0 $(GeV/c)^2$. The object of the comparison is to determine whether the ratio (R) of the radiatively corrected positron-proton cross section to the electron-proton cross section differs measurably from 1.

An $R \neq 1$ result can be interpreted as being due to the two-photon exchange contribution, since the interference between the first order scattering amplitude and the two-photon exchange amplitude occurs with opposite signs for electrons and positrons.

The data were obtained using positron and electron beams from the Stanford Linear Accelerator at two energies. Comparisons were made at 4 GeV for scattering angles of 12.5, 20.0, 27.5, and 35.0 degrees, and at 10 GeV for 2.6, 5.0, 12.5, and 15.0 degrees. The incident beam was passed through a liquid hydrogen target and the scattered electrons detected in either the SLAC 8-GeV/c or 20-GeV/c magnetic spectrometers.

The accuracy to which R was determined ranged from ±1.6% for the measurement at 4 GeV, 12.5° to ±10.8% at 4 GeV, 35°. The measurements, after radiative corrections, are consistent with R=1 within one standard error. Limits for the size of the two-photon amplitude and the consequences of these limits on theoretical two-photon estimates, are given.

TABLE of CONTENTS

TABLES

Page

I. INTRODUCTION

Electron-nucleon elastic scattering experiments to date have been interpreted using the single photon exchange model (see Fig. 1). If one assumes the electron behaves as a Dirac particle and one writes the most general Hermitian expression consistent with Lorentz invariance for the nucleon-photon vertex in Fig. 1, then the one-photon model gives the following expression for the electron-nucleon scattering cross section in laboratory coordinates:

$$\left(\frac{d\sigma}{d\Omega}\right) = \sigma_{Mott}\left(\frac{G_E^2(q^2) + \tau G_M^2(q^2)}{1+\tau} + 2\tau G_M^2(q^2)\tan^2\frac{\theta}{2}\right)$$

where: $$\sigma_{Mott} = \left(\frac{m r_o}{2E_o \sin^2\frac{\theta}{2}}\right)^2 \frac{E'}{E_o}\cos^2\frac{\theta}{2}, \qquad \tau = -\frac{q^2}{4M^2}$$

and where:

q^2 = four-momentum transfer squared ($q^2 < 0$ for spacelike q^2)

E_o = incident electron energy

E' = scattered electron energy

θ = electron scattering angle

r_o = classical electron radius = 2.82×10^{-13}cm.

m = electron rest mass

M = nucleon rest mass

$G_E(q^2)$, $G_M(q^2)$ functions of q^2 only

This expression, known as the Rosenbluth formula[1], has been widely

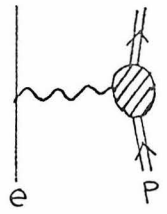

FIGURE 1: One-Photon Model

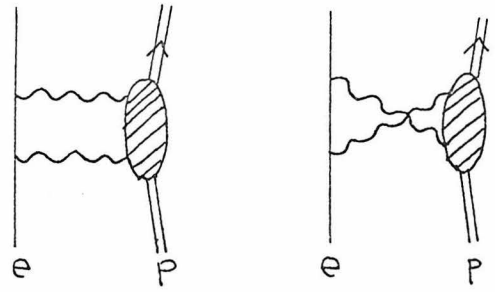

FIGURE 2: Two-Photon Terms

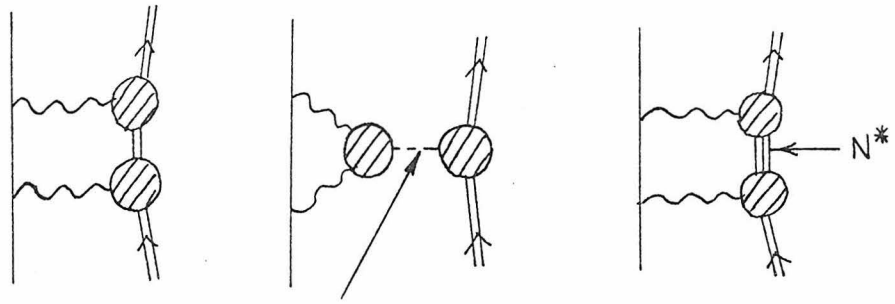

Double Single-Photon Vertices

Resonance in the Annihilation Channel

Resonance Along the Nucleon Line

FIGURE 3: Possible Resonant Contributions to Two-Photon Amplitude

used in the interpretation of electron-nucleon elastic scattering data. The expressions G_E and G_M, called the electric and magnetic form factors, respectively, are used to describe the electromagnetic structure of nucleons and much importance has been given to the empirical fits to G_E and G_M.

With the considerable interest in nucleon electromagnetic form factors, a question arises - is the Rosenbluth formula correct? Is the single photon exchange model valid in all kinematical regions for which there is elastic e^-p data? It is possible that the one-photon exchange term is insufficient, particularly in the high q^2 region. It may be necessary to include higher order terms, such as the two-photon exchange terms in Fig. 2.

Because of the additional vertices, one expects the two-photon amplitude to be smaller than the single-photon amplitude by order $\alpha=1/137$. However, the two-photon amplitude may be larger because of resonant enhancements. When two photons are exchanged we can have, in addition to two single-photon vertices, resonances in the annihilation channel or along the nucleon line as shown in Fig. 3. A discussion of theoretical estimates of such contributions occurs in Chapter VI.

A two-photon term will alter the Rosenbluth expression for the scattering cross section but may do so in a manner that it is difficult to determine from e^-p data alone. Whereas the Rosenbluth cross section is of the form:

$$\left(\frac{d\sigma}{d\Omega}\right) = \sigma_{Mott}\left(a(q^2) + b(q^2)\tan^2\frac{\theta}{2}\right),$$

the modified cross section including the two-photon contributions may still be of this form, but with different $a(q^2)$ and $b(q^2)$. If so, it can still be fitted with the Rosenbluth formula, but gives incorrect values for the electromagnetic form factors.

Even if the two-photon terms result in some alteration in the cross section from the single-photon form above, a significant departure from the above behavior may occur only in kinematic regions where the cross section is so low that a measurement of this deviation is difficult. This in fact is predicted to occur by some theoretical estimates of the elastic cross section with two-photon terms (this is discussed further in Section B of Chapter VI).

A measure of the real part of the two-photon amplitude can be obtained by comparing the cross sections for elastic scattering of positrons off nucleons with that of electrons off nucleons. This is because the interference between the single-photon term and the two-photon term occurs with opposite signs for electrons and positrons. This can be easily seen if one remembers the electron*-photon coupling is characterized by either +e for positrons or -e for electrons.

---

* The term "electron" will be used to mean either electron or positron except when a distinction is apparent from the context.

Looking at Fig. 4, if we call A=A'+C, then the electron-nucleon and positron-nucleon cross sections are:

$$\sigma^- \propto |-A+B|^2 \qquad \text{and} \qquad \sigma^+ \propto |A+B|$$

respectively. Therefore, the ratio of positron-nucleon and electron-nucleon elastic cross sections becomes:

$$R = \frac{\sigma^+}{\sigma^-} = \frac{|A+B|^2}{|-A+B|^2} = \frac{|A|^2 + |B|^2 + 2\,\mathrm{Re}(A^*B)}{|A|^2 + |B|^2 - 2\,\mathrm{Re}(A^*B)}$$

$$\cong 1 + 4\,\frac{\mathrm{Re}(A^*B)}{|A|^2}$$

Using the normal phase convention in which A is real, we have:

$$\boxed{R \cong 1 + \frac{4\,\mathrm{Re}B}{A}}$$

The measurement of this quantity, R, was the object of this experiment.

It should be mentioned that the radiative corrections to e^-p and e^+p elastic scattering are different, and will cause R to deviate from 1 even if σ^+ were equal to σ^- (this is discussed in detail in Section E, part 1, in Chapter III). Therefore, in the discussion above, R is the ratio of radiatively corrected cross sections.

In an experiment to measure R, the elimination of e^+/e^- asymmetries is of greatest importance. For this reason it is important to measure the relative positron and electron incident energy and beam charge to high accuracy. A shift in e^+ to e^- incident energy or a difference in the e^+ and e^- collection efficiency in the beam charge monitors, will result in R differing from 1 even if there is no two-photon contribu-

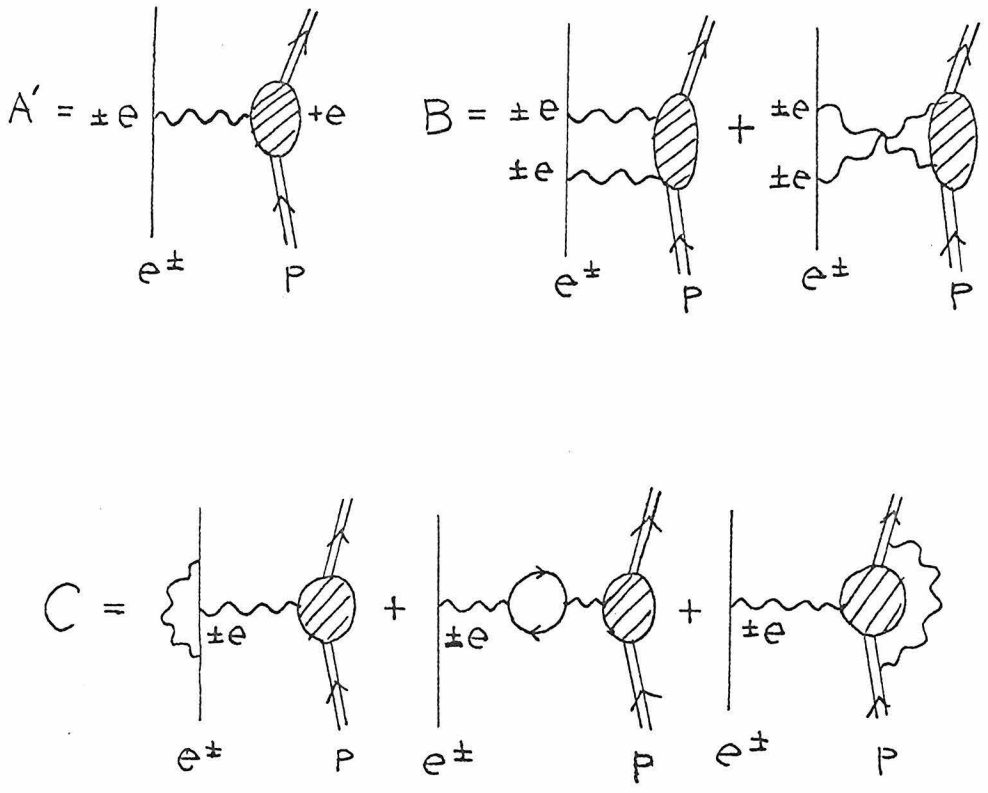

FIGUR E 4:

A=Lowest Order Single-Photon Diagram
B=Lowest Order Two-Photon Diagrams
C=Second Order Single-Photon Diagrams

tion. This can also be caused by a relative shift in the direction of the incident e^+ and e^- beam, as this will cause σ^+ to be at a different angle from σ^-. Thus it is also necessary to maintain the incident beam direction with considerable care. The control and measurement of these quantities for this experiment are discussed in Chapter II.

The background present during a measurement of R will in general be different for e^+ and e^-, and unless eliminated, will alter R. In this experiment the pion background presented the greatest problem (as the pion contamination is greater for e^+ than for e^-, cf. Section D, Chapter III) and a large part of the detection apparatus was used solely to discriminate between pions and electrons (Section F, Chapter II).

Previous experiments of R by other experimenters[2] have dealt with the q^2 region below 1.5 $(GeV/c)^2$. For the most part, their measurements (which are shown in Fig. 67 in Chapter V) agree with R=1.

In this experiment, measurements of R were made out to a q^2 of 5.0 $(GeV/c)^2$. R was also measured for moderate q^2 at smaller electron scattering angles than previously explored. The results are given in Chapter V.

II. EXPERIMENTAL METHOD

A. Summary

The positron and electron beams were made by passing an electron beam, with energy about 5.5 GeV, into a 2.2-inch thick water-cooled copper radiator positioned one-third of the way along the SLAC accelerator to form the beams for the experiment. In this way, for each data point the positron and electron beams were similar with regard to transverse phase space, energy spectrum and intensity. This technique was important in minimizing the effects of possible systematic errors.

The full energy spread of the beams varied from 0.5% to 1.0%. To increase intensity, the 1.0% width was used for most of the data. The average intensity varied from 6×10^9 $e^{\pm}$/sec to 4×10^{11} $e^{\pm}$/sec. The incident beam direction was maintained to better than ±0.1 mrad.

The beam charge was measured with a toroid current transformer and a Faraday cup. Two thin-foil secondary emission monitors were also used. The ratio of positron to electron charge measured by the toroid differed from the ratio measured by the Faraday cup by up to 1.5%. Comparisons with the secondary emission monitors indicated that the Faraday cup was more likely to be in error than the toroid. Various arguments tend to support this conclusion, but the discrepancy is not fully understood. As a consequence, the toroid was used as the standard for determining beam charge and a systematic error in R, equal to the observed disagreement between Faraday cup and toroid, was assigned

for each data point.

The SLAC 8-GeV/c magnetic spectrometer was used to analyze particles scattered from a 27 cm diameter vertical cylinder of liquid hydrogen. For the small angles (2.6° and 5.0°), the SLAC 20-GeV/c spectrometer was used with a 7 cm diameter target. The solid angle acceptances into these systems were approximately 0.8 msr and 0.06 msr, respectively.

The detection systems of both the 8-GeV/c spectrometer and the 20-GeV/c spectrometer were very similar in nature. Both systems contained momentum (p) and angle (θ) scintillation counter hodoscopes and a total absorption shower counter for π-e discriminator. The energy loss (dE/dX) in a counter positioned after 0.5 radiation lengths of lead was used to improve the π-e discrimination for the data at 35°. Pion contamination was reduced to less than 2% by requiring the pulse heights in the shower and dE/dX counters to be greater than certain minima.

An event, defined as anything that passed through the hodoscope and/or produced a large pulse in the total absorption counter, was logged on tape by a digital computer provided an earlier event had not occured in the same beam pulse. The electronics in this experiment was such that the the event logging rate was limited to a maximum of one event per beam pulse. The presence of numerous "flags" in the electronics allowed us to later select only events that have passed through both the hodoscope and the total absorption

counter (we also required the dE/dX counter for the 35° data) in the data analysis.

The ratio, R, of elastic e^+p and e^-p elastic scattering cross sections, was determined from the ratio of the number of e^+ and e^- counts normalized to beam charge, in select regions of the p and θ hodoscopes. These counts were obtained by averaging over a series of corrected measurements that alternated between positrons and electrons. This minimized biases due to long term drifts.

The general physical arrangement of the apparatus for this experiment is shown in Fig. 5.

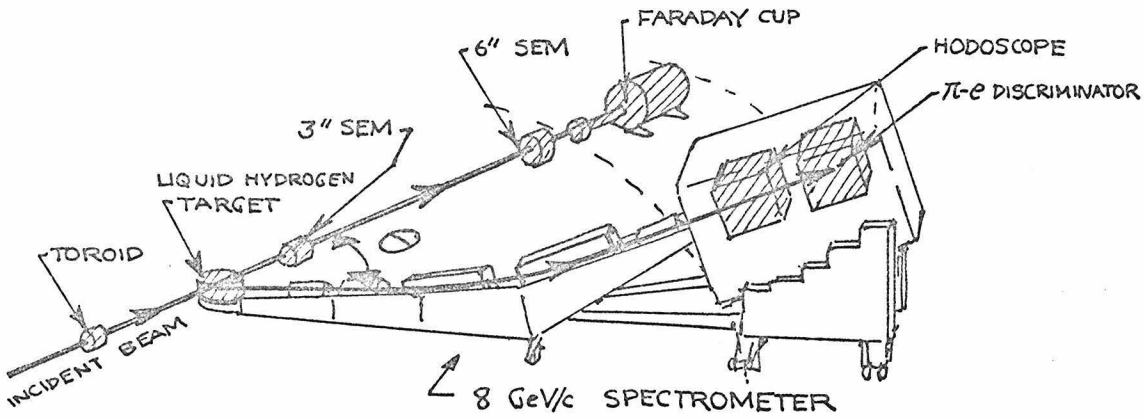

(a)
8-GeV/c System
(used for $\theta \geq 12.5°$ data)

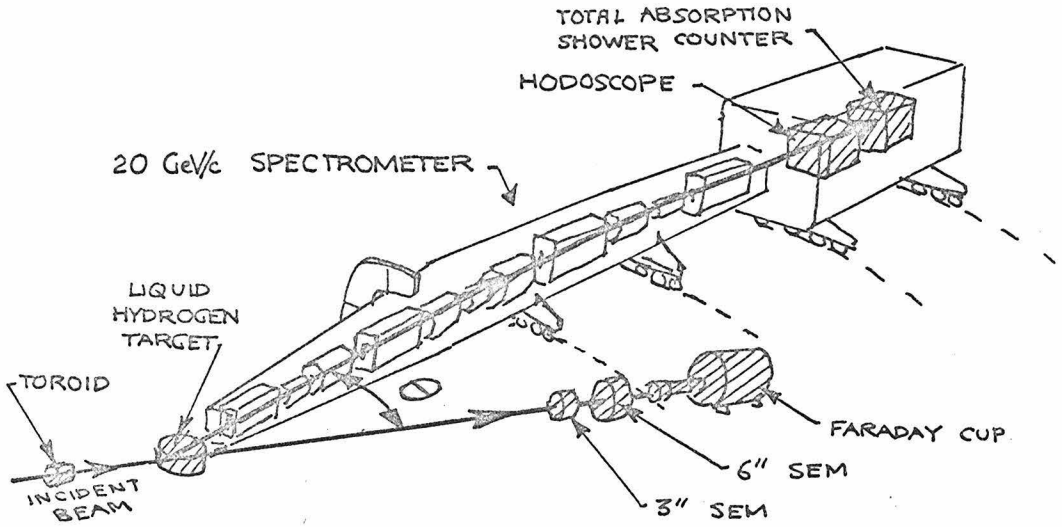

(b)
20-GeV/c System
(Used for $\theta < 12.5°$ data)

FIGURE 5: Physical Arrangement of Apparatus in This Experiment

B. Positron Source

Both the positrons and electrons were generated using the positron radiator[3] of the Stanford Linear Accelerator Center. The radiator was a water cooled 2.25 inch (3.8 r.l.) thick copper block (see Fig. 6) positioned one third the length of the accelerator from the electron gun.

Electrons accelerated to about 5.5 GeV were passed through the copper block to produce a shower of low energy electrons and positrons. After drifting a short distance, the electrons and positrons were passed through a tapered solenoid whose axial field gradient was small enough that the magnetic flux enclosed by a spiraling particle was an adiabatic invariant. The decreasing axial field of the tapered solenoid (B_{max}=18.2 KG, B_{min}=2.4 KG, length=25 inches) reduced the transverse momentum at the expense of increasing the beam radius. This can be seen below:

$$Br^2 = \text{const.} \Longrightarrow \frac{B(z_1)}{B(z_2)} = \frac{r(z_2)^2}{r(z_1)^2}$$

but $$r = \frac{P_t}{qB} \Longrightarrow \frac{P_t^2}{B} = \text{const.}$$

$$\Longrightarrow \frac{B(z_1)}{B(z_2)} = \frac{P_t(z_1)^2}{P_t(z_2)^2}$$

where:

r = radius of orbit

P_t = transverse momentum

$$\frac{P_t(z_1)^2}{P_t(z_2)^2} = \frac{r(z_2)^2}{r(z_1)^2} = \frac{B(z_1)}{B(z_2)}$$

However, since the radius of the beam emerging from the radiator was very small, this increased radius was not detrimental and was more than

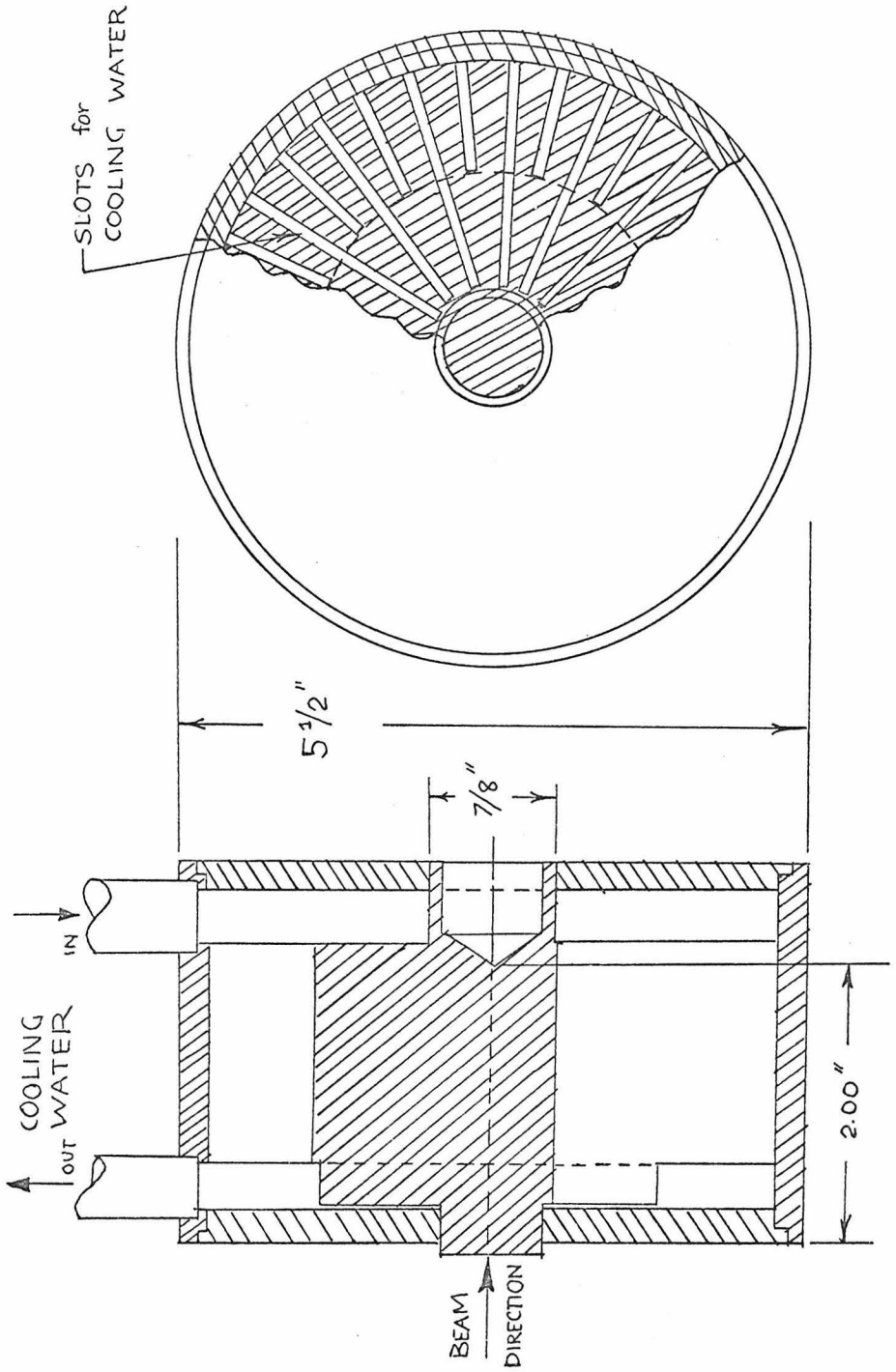

FIGURE 6:

Positron Radiator

compensated by the increased transmission due to the lower transverse momentum.

The beam then passed through a long (25 feet) uniform field (B = 2.4 KG) solenoid where it was held together and accelerated through two 10 foot sections of disk loaded waveguide. The uniform solenoid allowed the particles to reach a high enough energy that finite spaced quadrupoles could be used to continue the focusing. The spacing of the quadrupoles (S-1 to S-13 in Fig. 7) was proportional to the particle energy in order to maintain a constant admittance. The reason for such a spacing is intuitively clear if one remembers the transverse momentum, P_t, stays constant. Thus as the electron energy increases, the transverse velocity $v_t = P_t/m_o\gamma$ decreases. Therefore the distance $\ell = z_2 - z_1$ an on-axis particle at z_1 can travel before hitting the accelerator wall is:

$$\ell \simeq \frac{P(z_1)+P(z_2)}{2m} \frac{ma}{P_t} = E_{avg} \frac{a}{2P_t c}$$

Where:

a = radius of the accelerator beam pipe

These specially placed quadrupoles were continued until the needed quadrupole spacing was equal to the spacing of a standard accelerator sector, which has a quadrupole doublet at the end of each sector.

In the case of positron-proton scattering, the RF from the klystrons before the radiator is approximately* 180^o out of phase with

---

*The positrons emerging from the radiator are nonrelativistic and slip slightly in phase.

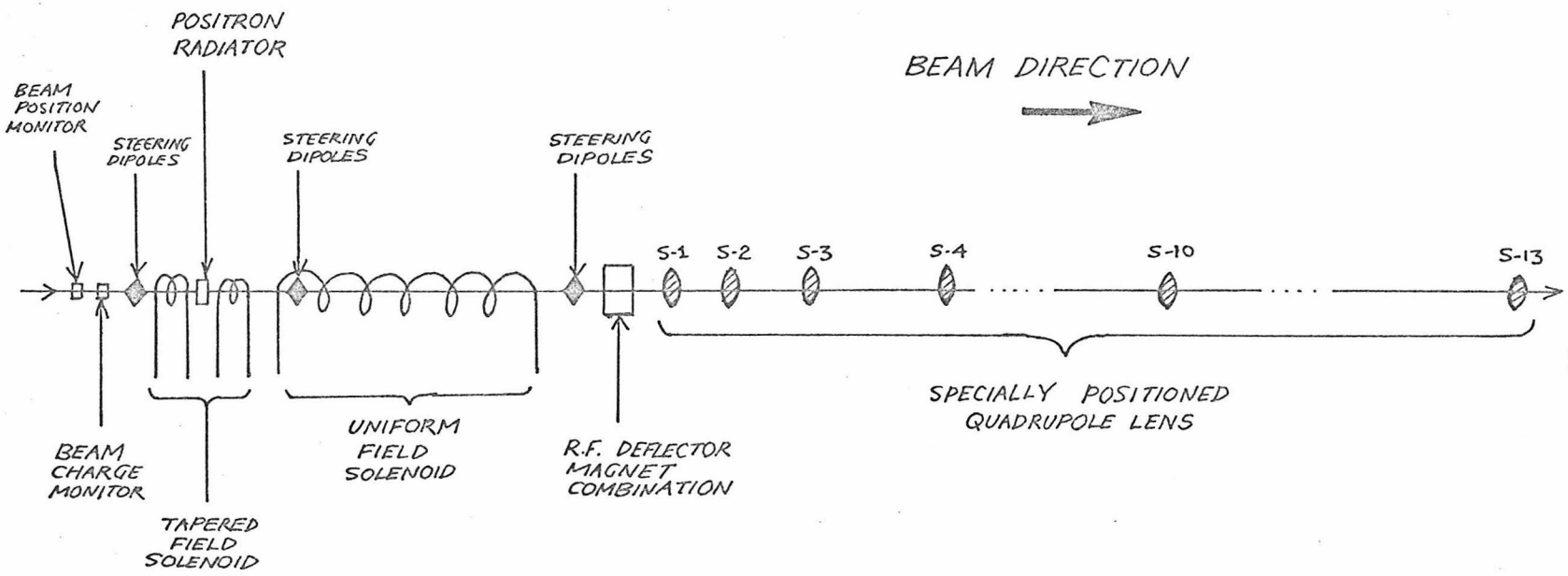

FIGURE 7: Schematic of the Positron Source

that after the radiator. Thus, except for those electrons that have slipped in phase by 180^{o}, only the positrons are accelerated and the electrons are decelerated. To remove the phase slipped electrons, the beam was passed through an RF deflector[4] and a magnet, positioned just before the first quadrupole lens. The phase of the RF deflector (operated in the HEM_{11} mode) was such that both electron and positron bunches were deflected in the same direction with the magnetic field direction chosen so that only the positrons were deflected back. The electrons, which have received two impulses in the same direction, were deflected into the wall about 10 feet downstream.

In the case of electron-proton scattering, the klystrons are not phase shifted 180^{o} and the RF deflector-magnet combination is chosen so as to deflect the phase slipped positron bunches into the wall while maintaining the electron beam. This electron beam was used instead of the direct electron beam in order to have comparable positron and electron beams, with regard to transverse phase space, energy spectrum and intensity.

The optical system beginning at the radiator enabled us to produce beams with the 5 to 15 MeV electrons and positrons emerging from the radiator.The yield (ratio of positron current in the experimental area, with a full energy width of 1%, to incident electron current into the radiator) was $\sim$1/2%. The maximum beam power into the radiator was $\sim$75 KW and the beam intensity at the target varied from 1.18×10^{10}/sec to 3.87×10^{10}/sec for e^{+} and 6.09×10^{9}/sec to 4.27×10^{10}/sec for e^{-}.

C. Beam Switchyard

After the particles from the positron source were accelerated to the desired energy, the beam was deflected into the "A" line (see Fig. 8) of the beam switchyard, where a further deflection and a passage through collimators allowed only those particles with energy in the range $E_o-\Delta E_o/2$, $E_o+\Delta E_o/2$ to be transmitted to the experimental area. This latter energy selection was important as the energy spectrum of the beam incident to the switchyard was very broad (full width $\lesssim 1\frac{1}{2}\%$ $\Delta E_o/E_o$) whereas the desired full width of the energy spectrum in the experimental area was $\gtrsim 1\% \Delta E_o/E_o$. Thus the switchyard was used as a magnetic spectrometer to select the energy and energy spectrum of the experimental beam.

A 180^o rotation flux loop[5] (flip coil) was used to sample the magnetic field inside a reference magnet identical to the energy defining magnets, and whose current line was connected in series with the energy defining magnets. The measurement was used by a computer to set the energy acceptance of the switchyard.

Because of the long path length between the switchyard bending magnets and the energy defining collimator, there is a possibility of the earth's magnetic field causing an energy shift in the positron beam relative to the electron beam. This has been explored in detail in Appendix A where it is shown to have a negligible effect on E_o.

Because a small shift in angle of the incident beam would produce a sizable shift in the counting rate, care was exercised in maintaining

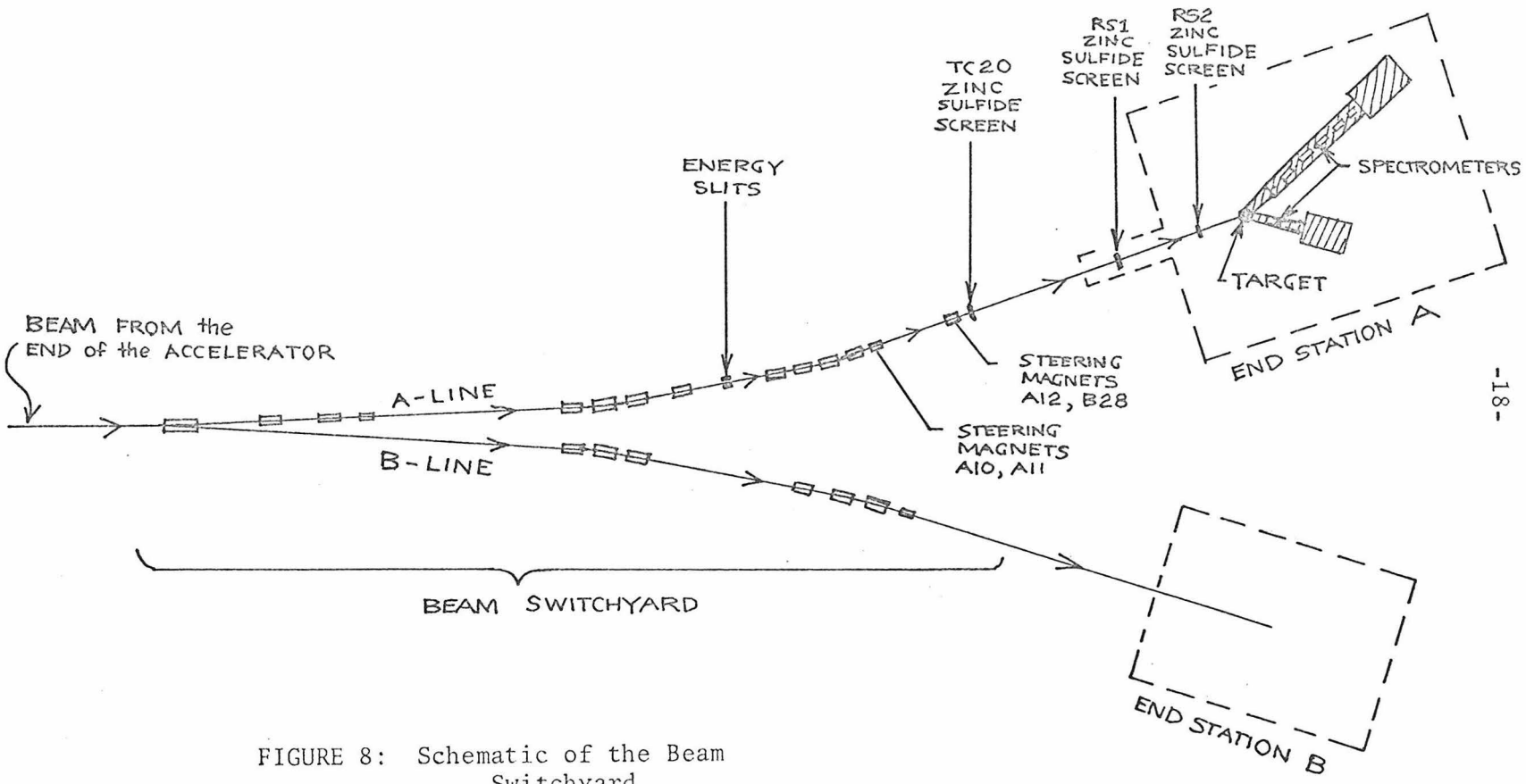

FIGURE 8: Schematic of the Beam Switchyard

the beam direction. Referring to Fig. 8, final beam steering was accomplished by first centering the beam on a retractable zinc sulfide screen (TC20) 164.7 feet upstream of the target, using steering dipoles A10 and A11, and then using magnets A12 and B28, immediately before TC20, to center the beam on a thin zinc sulfide screen (RS2) 15.2 feet upstream of the target. Since A12 and B28 were close to TC20, this defined two points over a 150-foot baseline. The beam path was slightly curved between the two points because of the earth's field. Since the curvature was in the opposite direction for electrons as for positrons, a systematic correction had to be applied for it.

During data collection, the screen TC20 was removed but RS2 and a similar screen, RS1 (see Fig. 8), were left in as a continuous monitor of the steering and shape of the beam.

Both RS1 and RS2 consisted of a ZnS coated aluminum foil stretched between two pneumatically driven rollers, so that a fresh portion of the screen could be rolled into the beam whenever the screen become darkened. All screens were viewed with closed circuit television.

D. Target

The liquid hydrogen targets[6] used in this experiment were of the condensation type. The liquid hydrogen in the target cell was maintained about 15 psi above atmospheric pressure so that its boiling point was about 23°K. The cell was maintained at ~20°K. by placing it in contact with a copper plate which in turn was in contact with a large reservoir of liquid hydrogen. Heat deposited by the beam caused the warm hydrogen to rise and be cooled by the copper interface.

A simplified diagram of the hydrogen target construction is shown in Fig. 9. The reservoir, with its attached target cell and dummy cell, could be raised and lowered by means of an air piston. With the reservoir fully lowered, the beam passed through the target cell filled with liquid hydrogen. With the reservoir in the middle position (uppermost position with moveable stop in Fig. 9 in), the beam passed through a similar target cell that was empty of liquid hydrogen. When the reservoir was in its uppermost position (moveable stop in Fig. 9 out), the beam missed both cells. In this experiment the dummy cell was inserted in the beam for studying backgrounds.

Acoustic and differential temperature measurements were performed on such targets with average electron currents up to 17 microamps, and the indications were that the corrections for bubbling in the liquid hydrogen were small for currents below 1 microamp. Since the average beam current in this experiment was less than 0.06 microamps, the corrections are expected to be negligible for this data. This was checked

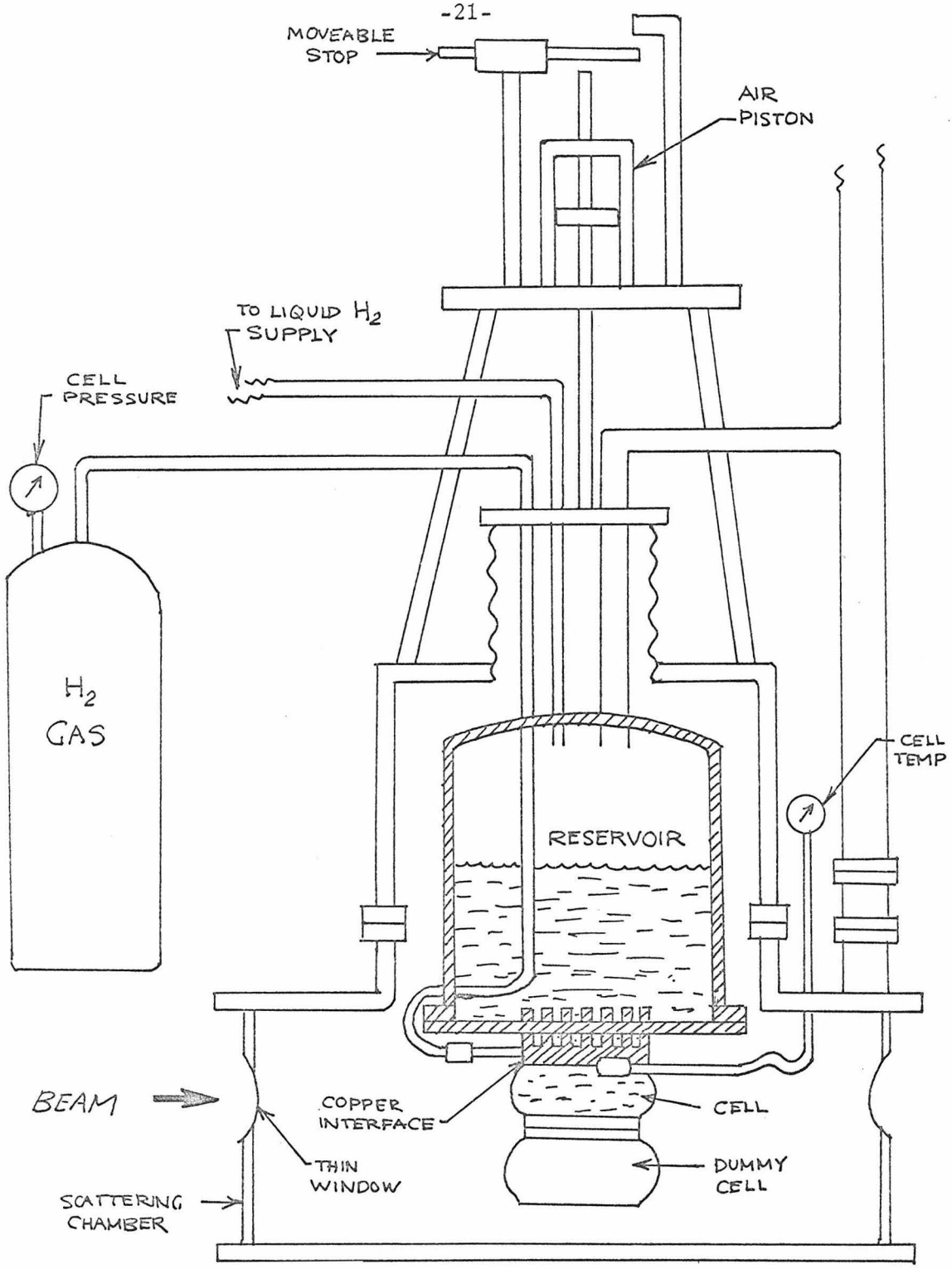

FIGURE 9:
Liquid Hydrogen
Target

by seeing whether or not the experimental cross section changed when the beam intensity was varied from 42 nanoamps to 9 nanoamps. The cross section was observed to change by less than 1%, the statistical uncertainty in the measurements. From pressure measurements the inferred liquid hydrogen density in the targets was 0.07035 grams/cm^3.

The diameters of the target cells used in this experiment were 27.56 cm and 7.016 cm. The 27.56 cm target was used for all the data with $\theta \geq 12.5^{\circ}$. At the time the small angle data ($\theta=2.6^{\circ}$ and 5.0°) was taken, the existing target was the 7.016 cm one.

E. Beam Charge Monitors

The primary standard for determining the beam charge was a toroid current transformer. A Faraday cup was used as a secondary standard. Two thin-foil secondary emission monitors were also used to measure the beam charge over short periods to provide a running check on the toroid and Faraday cup.

The physical locations of the monitors during the collection of the large ($\theta \geq 12.5^{o}$) and small ($\theta \leq 5.0^{o}$) angle data are shown in Fig. 10 and Fig. 11, respectively.

1. Toroid

The toroid beam charge monitor operates in a straightforward manner. A pulsed electron or positron beam passing through the center of the toroid (see Fig. 12) induces a current in the windings of the toroid, where the induced voltage is proportional to the rate of change of beam current. Hence, for a fixed beam pulse length, the induced voltage is proportional to the beam current. By electronically integrating this current, we can obtain a measure of the total beam charge over any particular period.

The toroid transformer[7] used in this experiment is shown in Fig. 12. It consisted of two separate transformers, each made up of four 1/2 inch thick ferrite rings, wound with 48 turns of insulated copper wire. Each toroid was surrounded by an electrically insulated aluminum case that acted both as a Faraday shield and a physical support. Only

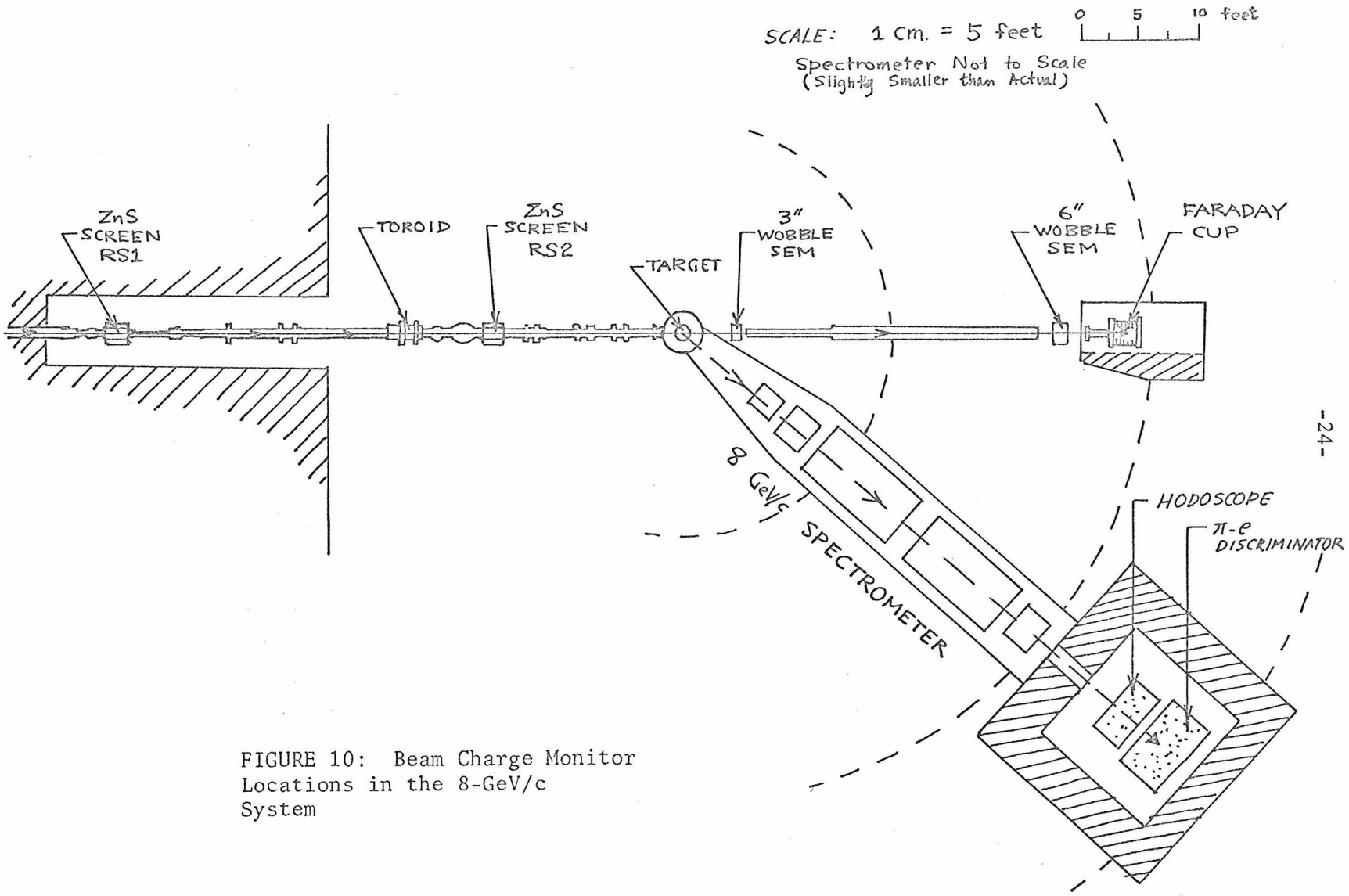

FIGURE 10: Beam Charge Monitor Locations in the 8-GeV/c System

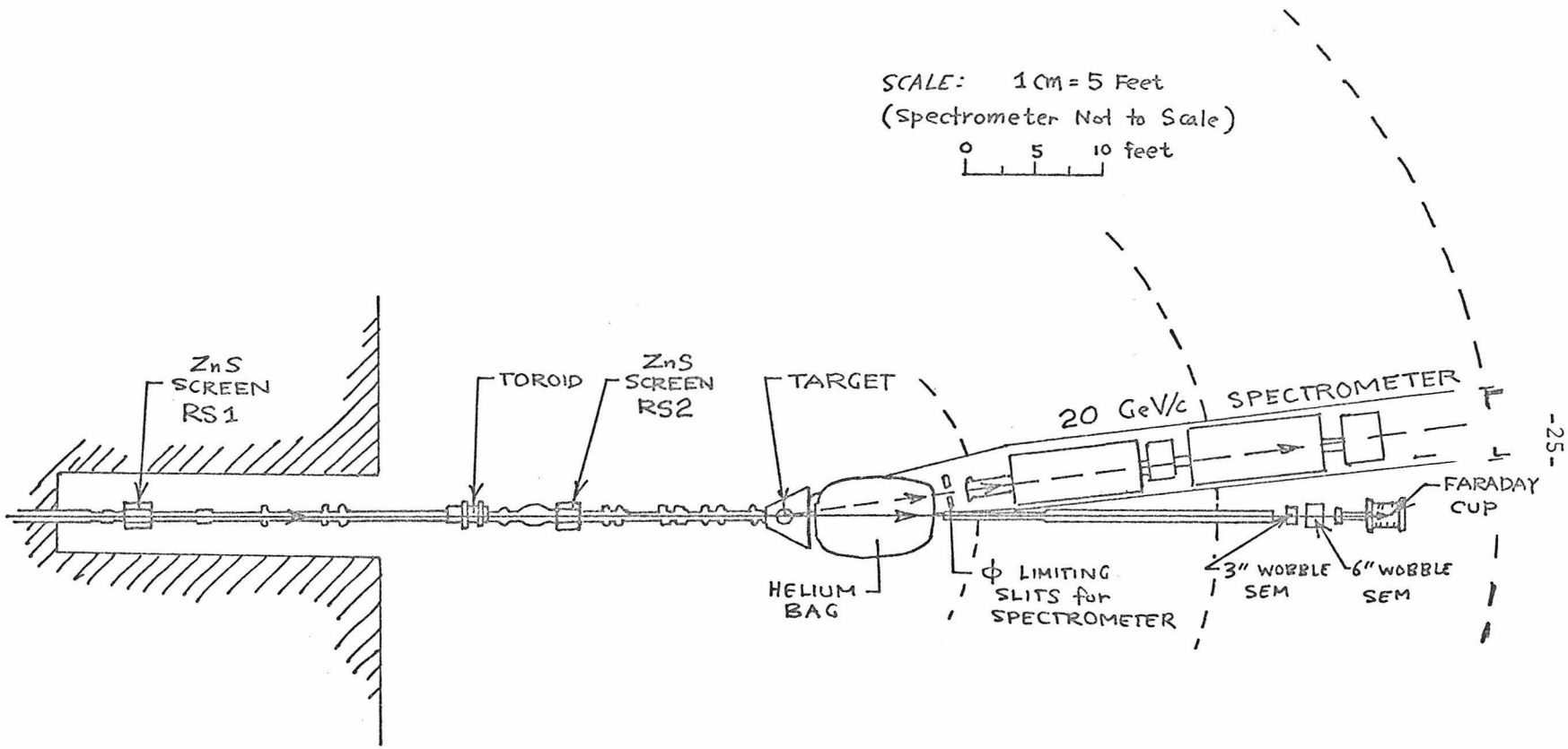

FIGURE 11: Beam Charge Monitor Locations in the 20-GeV/c System

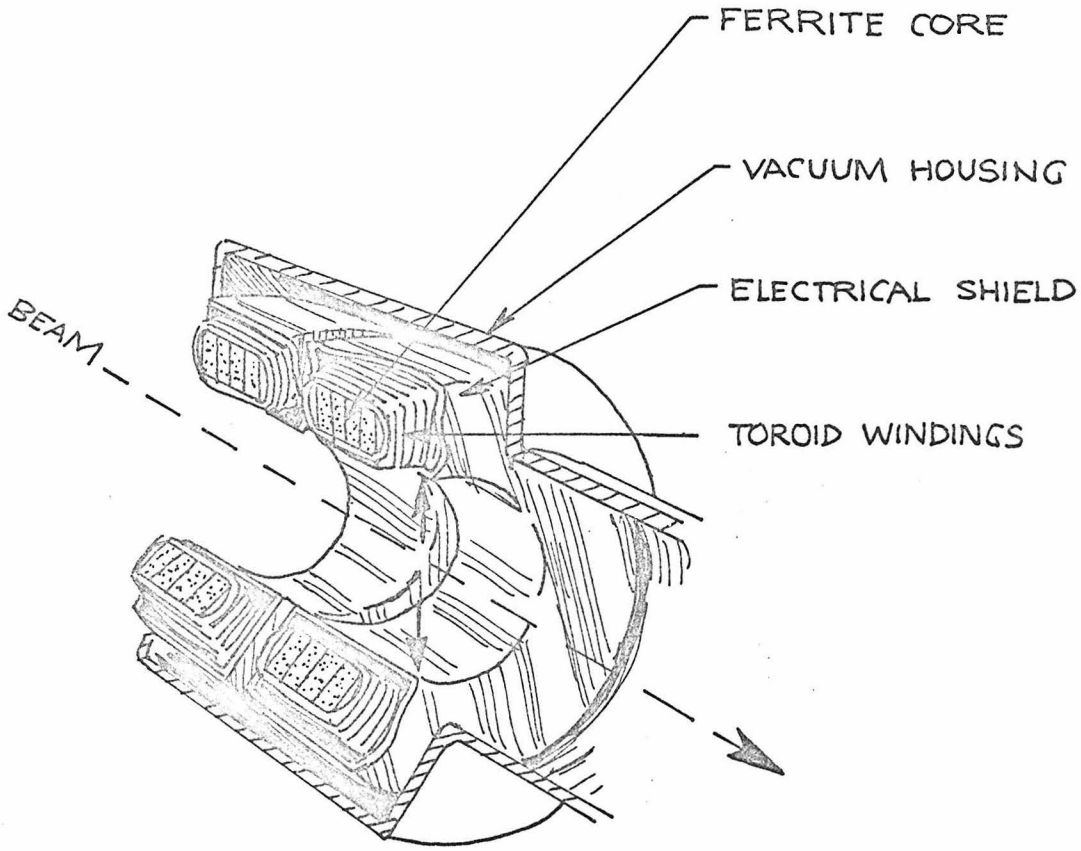

FIGURE 12: Cutaway
Diagram of Toroid Current
Transformer

one of the toroids was used to integrate the charge. The other toroid served as an intensity monitor and provided a signal for a video display of the beam structure as a function of time. The beam aperture of the toroid was 3 inches.

The linearity and reproducibility of the toroid was nominally better than 0.1%. However, the reliability of the monitor decreased for small beam currents due to the existence of drift currents in the electronics of the charge integrator. The drift currents were generally around 0.05 nanoamps. Since most of the data was taken with average beam currents around 40 nanoamps, the drift corrections were small. Only the $\theta \leq 5^{o}$ data were taken with average beam currents as low as 1 nanoamp, and for this data the Faraday cup was used as the monitor.

The relative charge integration efficiency for electrons versus positrons was measured by injecting pulses into a test winding on the toroid, with and without the toroid output leads reversed. The toroid asymmetry was also checked directly with positron and electron beams. In all cases the asymmetry was found to be less than 0.2%.

2. Faraday Cup

The Faraday cup is essentially an insulated charge collector, constructed so as to stop a beam entirely and thus be able to collect and measure all the beam's charge. The Faraday cup in this experiment was connected to a Cary Model 31 integrator, which continuously transferred charge collected in the Faraday cup to high precision

capacitors. By this procedure, the potential of the Faraday cup was maintained constant and the problem of charge leakage was transferred from the Faraday cup to the controlled environment of the integrator capacitors. To minimize charge leakage in these capacitors, the charge was never allowed to accumulate beyond 3×10^{-8} Coulombs (using a 10^{-6} farad capacitor) before the capacitors were zeroed.

The construction of the Faraday cup[8] is shown in Fig. 13. The Faraday cup placed 72 radiation lengths of material into the beam line and had a radius equal to 46 radiation lengths of material. The hole in the center of the lead block of the cup (Fig. 13) and the carbon plug at the bottom of the hole were to minimize charge losses due to backward-going shower electrons and backward secondary electrons. The entrance window was placed at the front of a long snout to prevent secondary electrons emitted from the window from entering the cup. Additional discrimination against secondary electrons was provided by permanent magnets that produced a field of greater than 250 gauss in a three-inch long region near the entrance of the snout. The field was sufficient to prevent electrons with energies below $\sim$1.5 MeV from getting into the cup. A copper, instead of lead, core was used in the center of the cup to enable the cup to absorb more power without damage.

The nominal operating pressure inside the cup was about 10^{-6} torr. At this pressure, the production and collection of ions in the gas inside the Faraday cup should have affected the charge collection

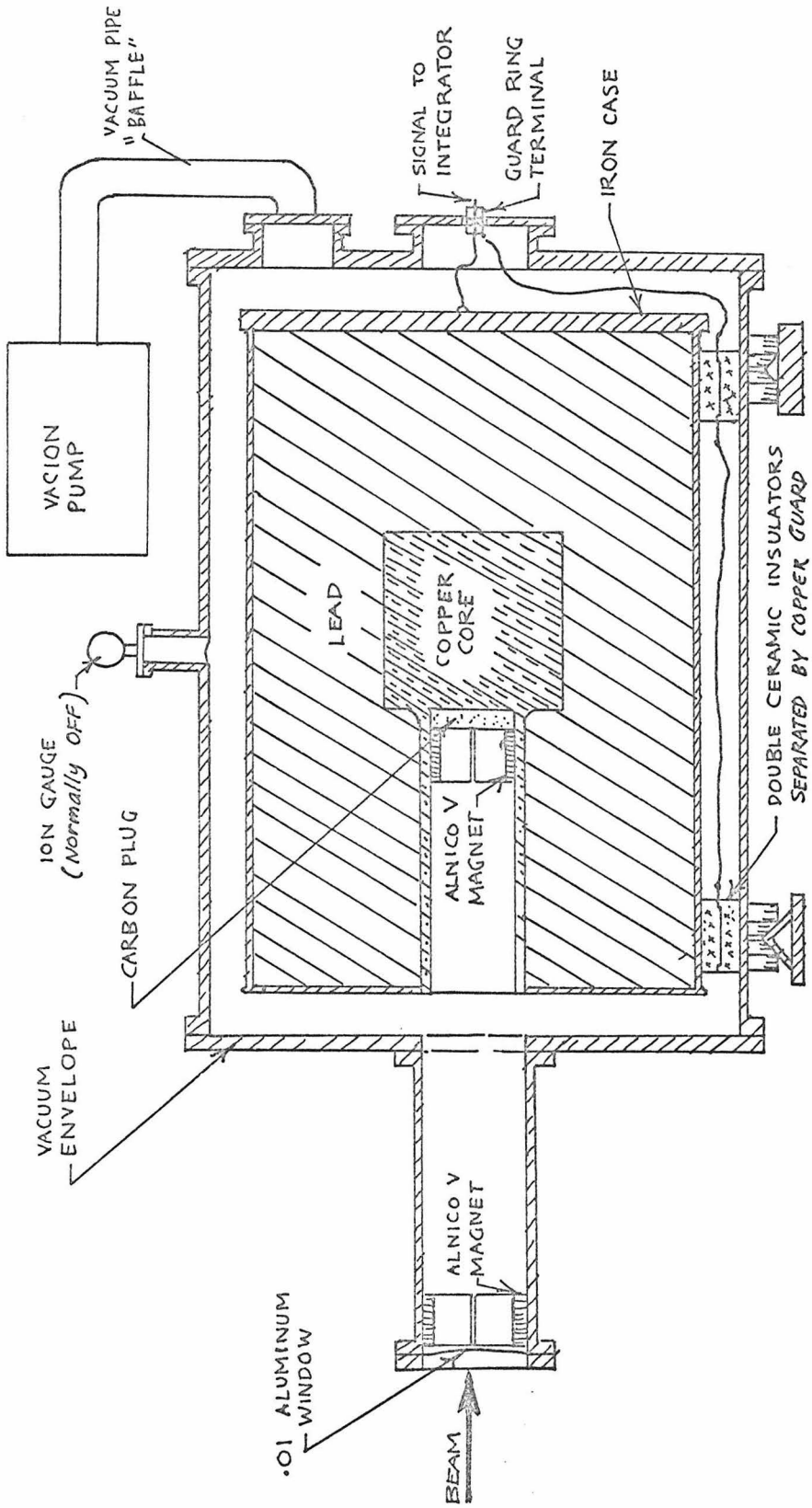

FIGURE 13
Cross section diagram of the Faraday cup

accuracy by less than ±0.1%.

Tests[8] carried out using electrons with energies from 200 MeV to 15 GeV indicate the absolute charge collection efficiency of the Faraday cup to be (100.0±0.2)% over this range. The difference in efficiency between electrons and positrons was thought to be less than ±0.1% at the energies of this experiment.

3. Secondary Emission Monitors

The secondary emission monitor (SEM) is very similar to an ion chamber except that there are no ions. Like an ion chamber, the SEM consists of a series of parallel plates, orientated perpendicular to the beam (see Fig. 14), with alternate plates at a high potential with respect to the remaining plates. However, unlike an ion chamber, the plates are placed in a vacuum so that ion formation between the plates is negligible.

When an electron (or positron) beam passes through the plates, secondary electrons are emitted into the regions between the plates. The strong electric field between the plates will cause the secondary electrons to go to the positive (i.e., least negative) plates, where the charge is integrated to give a measure of the beam charge.

Unlike ion chambers, which are sensitive to changes in gas density and ion saturation, the SEM suffers from none of this since it operates in a vacuum. However, one problem does exist with SEM's. The efficiency for the formation of secondary electrons at any given point in the SEM decreases with time because of thermal effects where the beam passes through. This phenomenon was minimized in our SEM's by having both SEM's continually moving in a sinusoidal manner perpendicular to the beam. In this way, the beam did not remain at any spot of the SEM for more than an instant.

Two "wobbling" SEM's were used in this experiment.

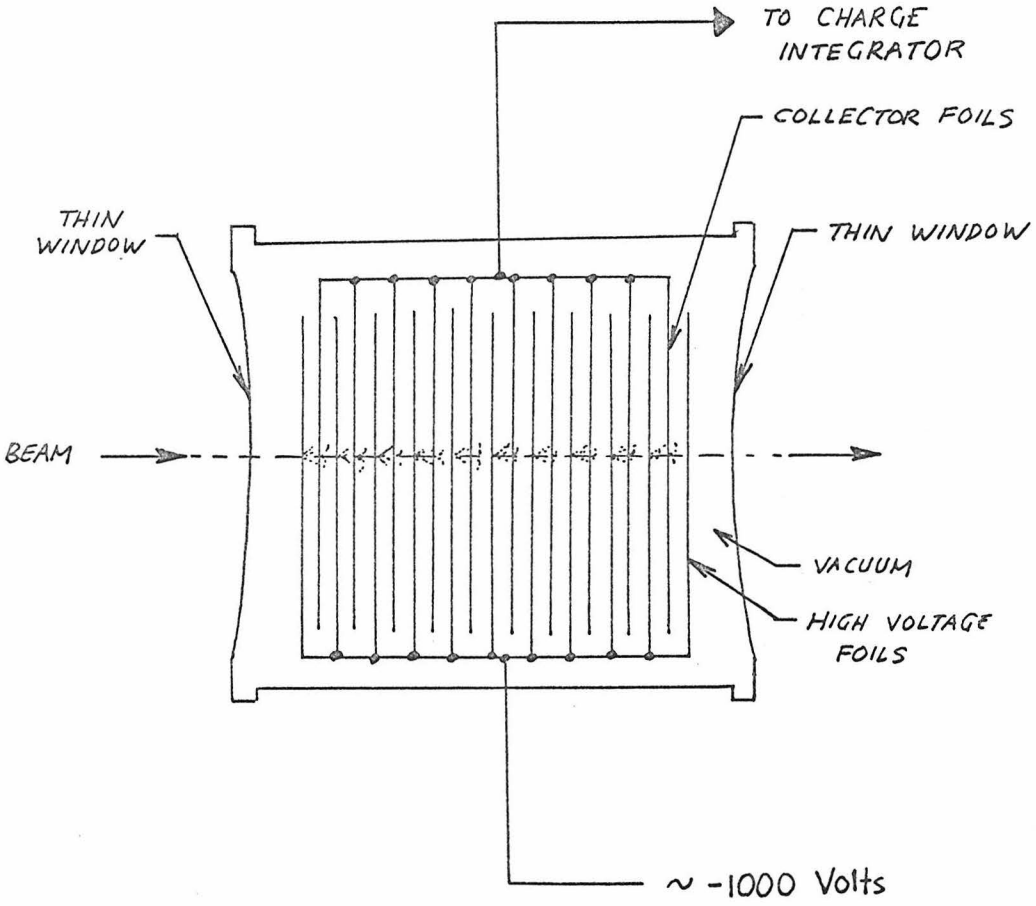

FIGURE 14: Typical Secondary Emission Monitor

One SEM had a 6 inch diameter useful aperture and consisted of seven collector foils between eight high voltage foils. Each foil consisted of 0.0002 inch aluminum which had $\sim$500Å of gold evaporated on both sides. The gap between plates was 1/2 inch. The collector and high voltage foils were isolated electrically by grounded guard rings. The complete SEM with its windows placed 0.0047 radiation lengths of material into the beam line. The vacuum of this device was typically 10^{-7} mm Hg. The charge collection efficiency of this SEM during this experiment was 58%.

The other SEM had a useful aperture of 4 inches (diameter) and consisted of three collector foils between four high voltage foils. Each foil consisted of 0.00025 inch aluminum that had been evaporated on both sides with $\sim$500Å of gold. The gap between plates was 1/4 inch. As in the 6 inch SEM, the collector and high voltage plates were electrically isolated by grounded guard rings. The complete SEM placed 0.0033 radiation lengths of material into the beam. The device was typically run with a vacuum of 10^{-6} mm Hg. The charge collection efficiency of this SEM during this experiment was 26%.

4. Discrepancy Between Faraday Cup and Toroid

Although separate measurements of the e^+/e^- asymmetry in the monitor efficiencies indicate it to be less than 0.2%, the apparent asymmetry during the experiment was greater than this. The ratio of beam charge measured by the toroid (Q_{Tor}) over that measured by the Faraday cup (Q_{FC}) differed by about 1.5% between positrons and electrons. In all cases: $(Q_{FC}/Q_{Tor})_- \geq (Q_{FC}/Q_{Tor})_+$.

This may be explained by the different locations of the toroid and Faraday cup. The toroid was $\sim$22 feet upstream of the target whereas the Faraday cup was $\sim$30 feet downstream of the target. Electrons passing through material after the toroid,bremsstrahlung and produce a cone of low energy gammas about the central beam line. Some of these photons will hit the walls around the snout of the Faraday cup (see Fig. 13) and the resulting Compton collisions in the walls may knock electrons into the charge collecting cup inside. This would add to the electron charge and subtract from the positron charge and explain the asymmetry observed.

This interpretation is also in agreement with comparisons made with two secondary emission monitors. Tests at 4 GeV between the two secondary emission monitors indicated the Faraday cup collection efficiency was asymmetric by $\sim$1%.

Because of this, we used the toroid as the primary standard for measuring the beam charge. However, the discrepancy between $(Q_{FC}/Q_{Tor})_+$ and $(Q_{FC}/Q_{Tor})_-$ is not well understood and a systematic error in R,

equal to the observed disagreement between $(Q_{FC}/Q_{Tor})_+$ and $(Q_{FC}/Q_{Tor})_-$ for each data point, was assigned for the monitor uncertainty.

F. Spectrometers

Two magnetic spectrometers, each with its own set of detectors and electronics, were used in this experiment (see Fig. 15 and Fig. 16). Because of its large solid angle acceptance, the SLAC 8-GeV/c spectrometer[9] was used to collect most of the data ($\theta \gtrsim 12.5^{\circ}$ data). The SLAC 20-GeV/c spectrometer[10], with a much smaller solid angle acceptance, was used for the $\theta=2.6^{\circ}$ and 5.0° data, where the elastically scattered electron momenta were greater than 9.6 GeV/c.

1. 8-GeV/c Spectrometer System

a. General

The 8-GeV/c spectrometer consisted of 2 quadrupoles, followed by 2 bending magnets, followed by another quadrupole. The optics of the system was such that particles were deflected in the vertical direction, and focusing from the center of the target to the focal planes was parallel-to-point in the horizontal plane and point-to-point in the vertical plane. This type of focusing was used to enable two orthogonal counter arrays to increase the momentum (p) and angle (θ) resolution. The physical positioning of the magnets and their thin lens equivalents are shown in Fig. 15 and Fig. 17.

At the horizontal focal plane (θ-focal plane) a 55 element scintillation-counter hodoscope was used to provide a scattering angle resolution of ± 0.15 mrad. The vertical focal plane (p-focal plane), which was tilted at a 15° angle to the central ray to minimize chro-

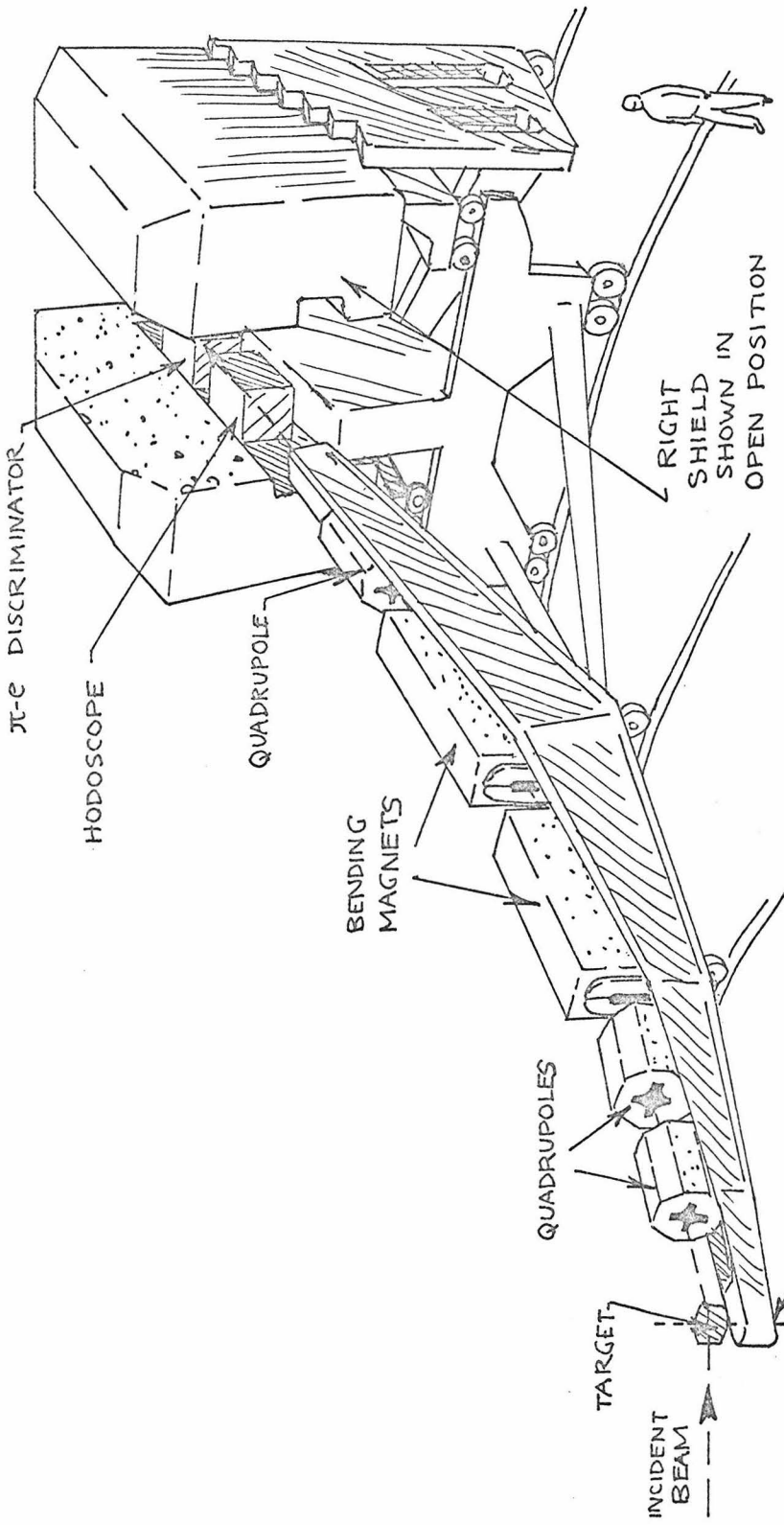

FIGURE 15: 8-GeV/c Spectrometer

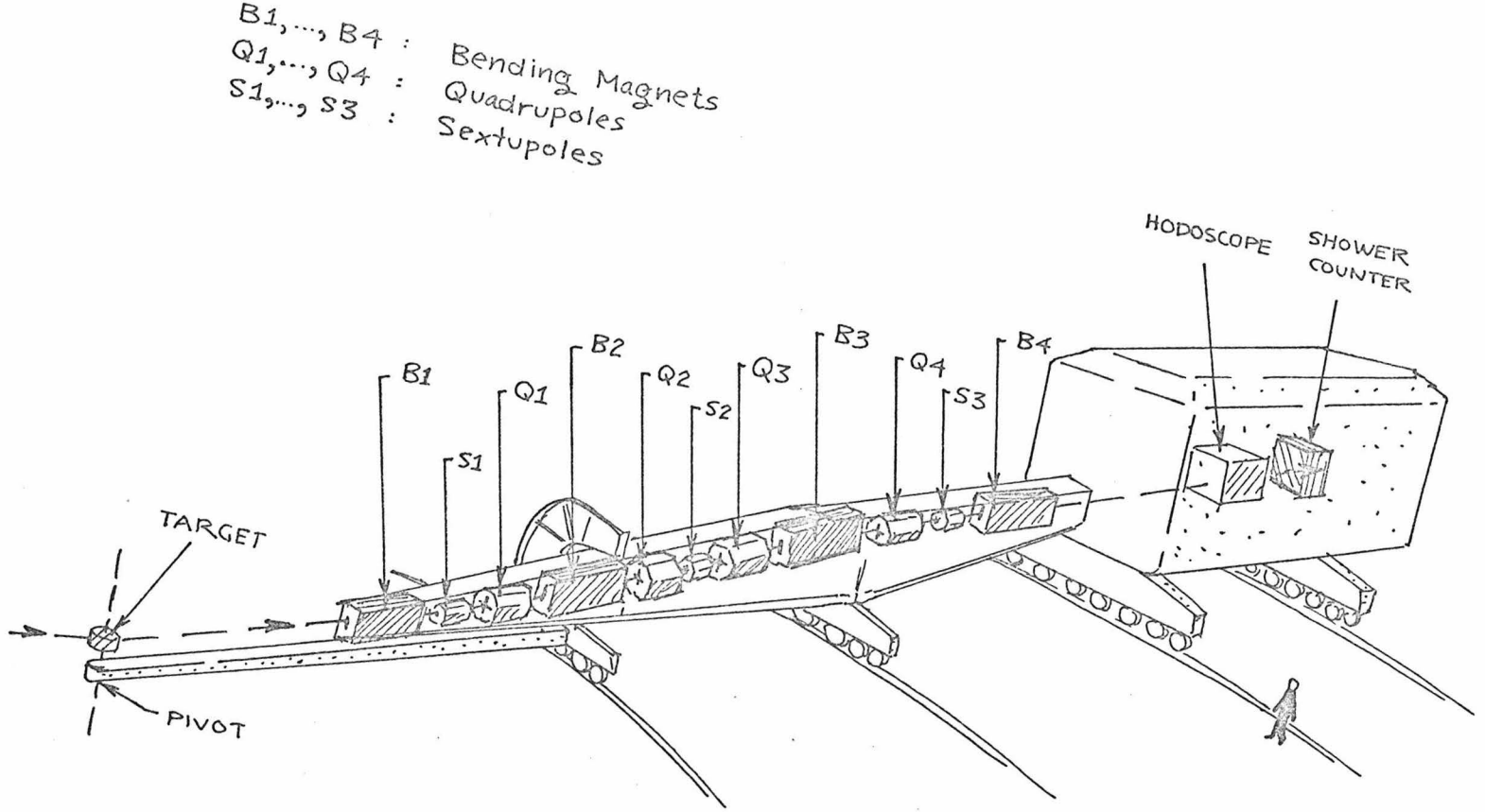

FIGURE 16: 20-GeV/c Spectrometer

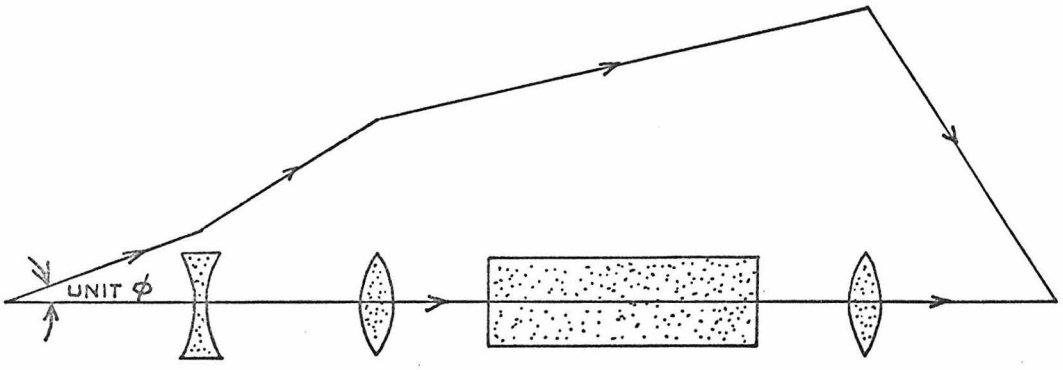

Vertical Plane

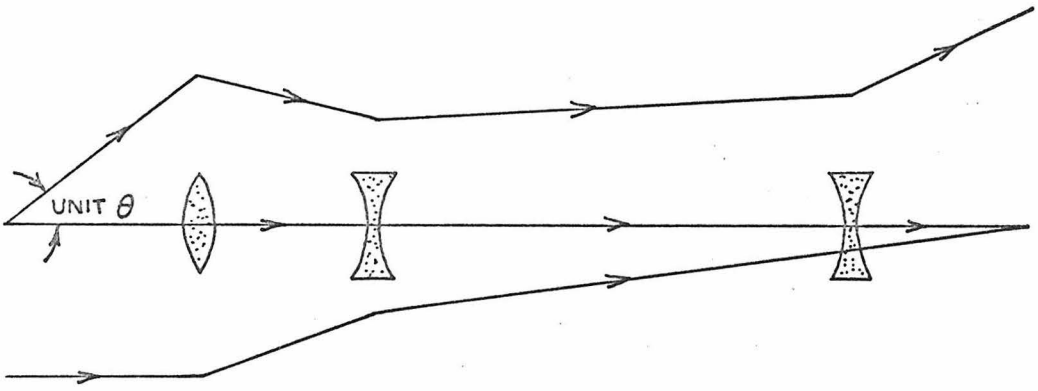

Horizontal Plane

FIGURE 17: Thin Lens Equivalents
of the 8-GeV/c Spectrometer

matic aberrations, contained a 41-element scintillation-counter hodoscope to provide a momentum resolution of ±0.05% Δp/p.

The solid angle acceptance into a given region of the θ-p hodoscope plane has been studied by both optics tests and counter measurements using the elastic peak as a probe; in addition, theoretical calculations have been made. The results of these studies agree well with the following empirical fit to the azimuthal angular acceptance (Δφ):

$$\Delta\phi(\vartheta,\delta) = (59 - 0.47\vartheta^2)(1 - 0.04\delta^2)$$

Where: ϑ = scattering angle relative to the center of the θ-hodoscope, in milliradians.
i.e.

$$\vartheta = (\theta - \theta_c)$$

θ = scattering angle in mrad
θ_c = angle corresponding to the center of the θ-hodoscope

δ = momentum position relative to the center of the p-hodoscope, in %Δp/p.
i.e.

$$\delta = 10^2\left(\frac{P - P_c}{P}\right)$$

P = scattered momentum
P_c = momentum corresponding to the center of the hodoscope

Since the total θ-acceptance of the hodoscope was 15.6 mrad, using this expression for Δφ we obtain the total solid angle acceptance for δ=0 to be 0.76 msr.

The overall characteristics of the 8-GeV/c spectrometer are shown in Table I.

For a given scattering angle and momentum, transport calculations

CHARACTERISTIC	8-GeV/c Spectrometer	20-GeV/c Spectrometer
Maximum Momentum	8 GeV/c	20 GeV/c
Momentum (p) Resolution	±0.05% $\Delta p/p$	±0.05% $\Delta p/p$
Scattering Angle (θ) Resolution	±0.15 mrad	±0.13 mrad
Solid Angle ($\Delta\Omega$) Acceptance	0.77 msr	0.058 msr
Total p Acceptance	4.0%	3.5%
Total θ Acceptance	15.6 mrad	7.5 mrad
Total Azimuthal Angular Acceptance	59 mrad	4 mrad
Distance from target to θ-focus	21.5 m.	42.5 m.
Distance from target to p-focus	22.0 m.	43.0 m.

TABLE I.

Overall Characteristics of 8-GeV/c and 20-GeV/c Spectrometers as used in This Experiment

indicate that the solid angle acceptance is constant for horizontal beam displacements (x_o), perpendicular to the central axis of the spectrometer, up to ±10 cm. Since the largest target used in this experiment was 27.56 cm in diameter and the largest scattering angle was 35^o, the greatest x_o encountered was $\pm(27.56/2)\sin(35^o)=\pm 7.9$ cm. Hence solid angle variation with longitudinal scattering position in the target should not be a problem.

Because of the large ϕ-acceptance (59 mrad at the center of the θ-p hodoscope), electrons scattering at an angle θ relative to the incident beam do not necessarily enter a definite θ-hodoscope bin. This can be easily seen by referring to Fig. 18. In Fig. 18 the actual scattering angle is θ, but because of the finite ϕ angle, the event falls into the θ-hodoscope bin corresponding to an angle θ'. However, since the ϕ-acceptance is the same for e^+ and e^-, such an effect does not affect our determination of R.

b. Monitoring the Spectrometer Fields

The bending magnets in the 8-GeV/c spectrometer were monitored continuously in two ways. An on-line SDS 9300 digital computer continuously monitored the current supplied to the magnets (including the quadrupoles) by comparing the voltages read across shunts to a standard table of voltages corresponding to the particular momentum setting. A deviation in any of the voltages by ±0.2 millivolts would cause the computer to signal the operator. In addition to this current monitoring, a nuclear magnetic resonance (NMR) probe was placed in

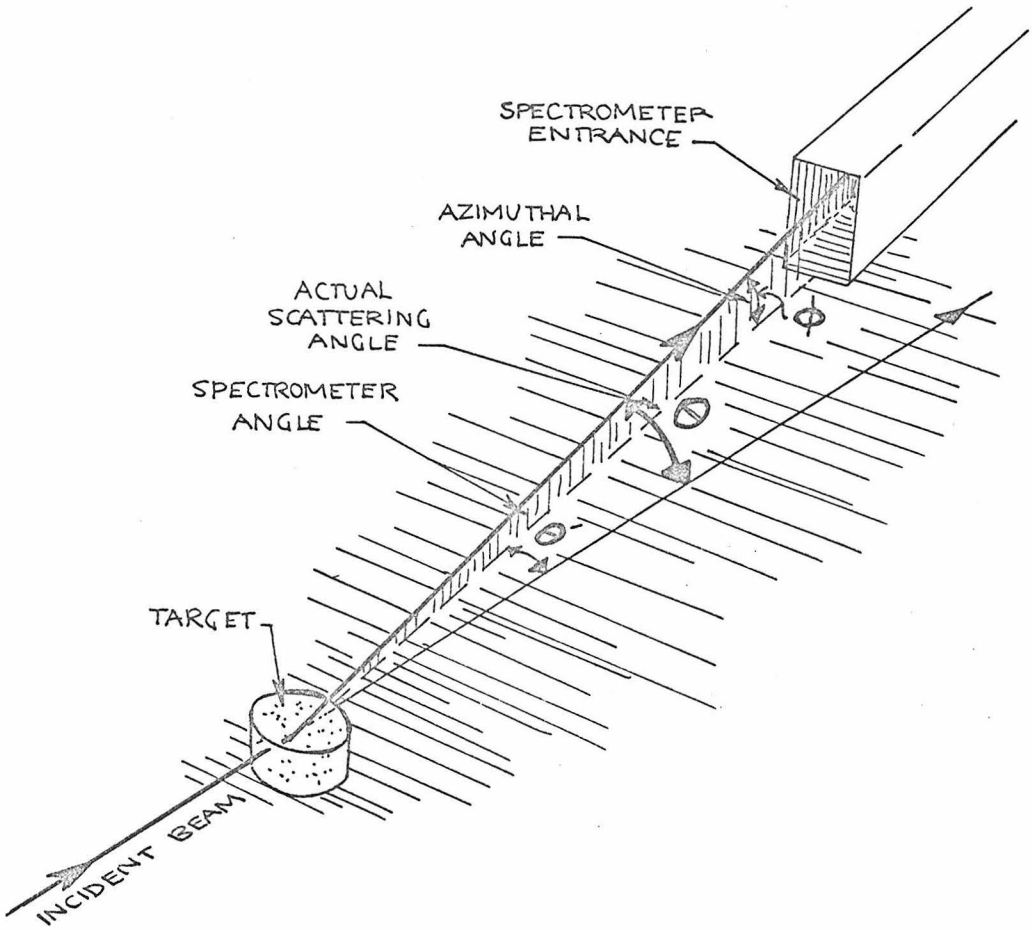

FIGURE 18:
ϕ-θ Mixing in the
Spectrometer

each of the two bending magnets. The resonant frequencies of the H_2, Li_7 and D_2 samples in the probe extended over a wide enough range that a direct measurement of the magnetic fields was possible for all settings used in this experiment. The control panel and readout for the NMR were remotely located in the counting house and thus allowed us to monitor the bending magnet fields throughout the data collection.

c. Spectrometer Detectors

The detection system in the 8-GeV/c spectrometer consisted of a hodoscope and a pion-electron discriminator.

The hodoscope consisted of the p and θ counter arrays previously mentioned, as well as a set of 5 trigger counters at the very front of the hodoscope and 5 trigger counters at the rear. The geometry of the hodoscope is shown in Fig. 19.

Because of the close proximity of the p-hodoscope phototubes, the positioning of the p-hodoscope scintillators was facilitated by the use of flexible epoxy joints between the scintillators and the phototubes. Conventional hard epoxy joints were used to attach the scintillator in all other counters.

The scintillator material was NE102 in all cases and the phototubes were RCA 7767's for the p-counters, RCA 6199's for the θ-counters, and RCA 8575's for the trigger counters.

The π-e discriminator is shown in Fig. 20. The only portion of the π-e discriminator used in this experiment was the total absorption (TA) shower counter and one dE/dX counter.

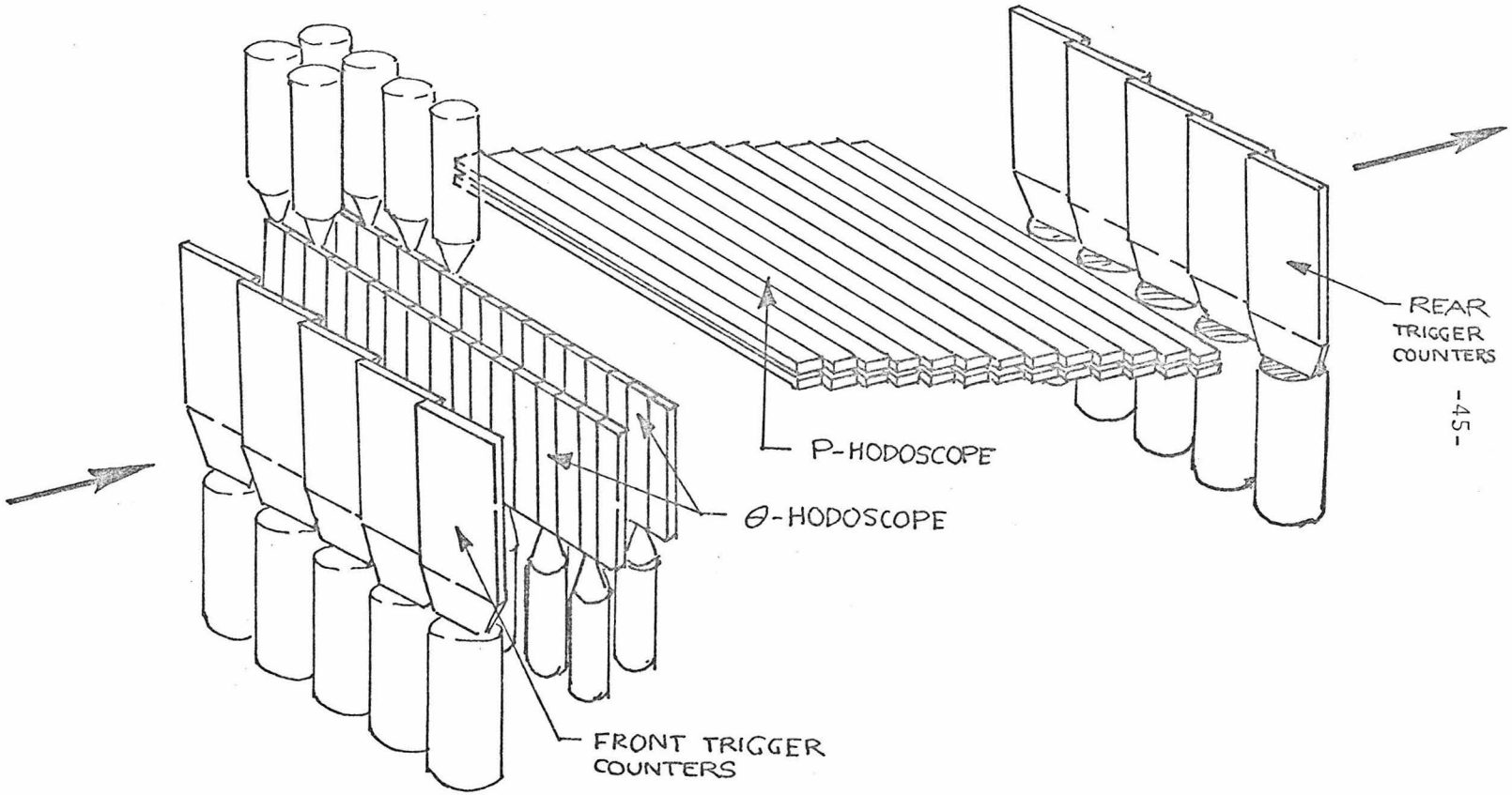

FIGURE 19: Geometry of 8-GeV/c Hodoscope

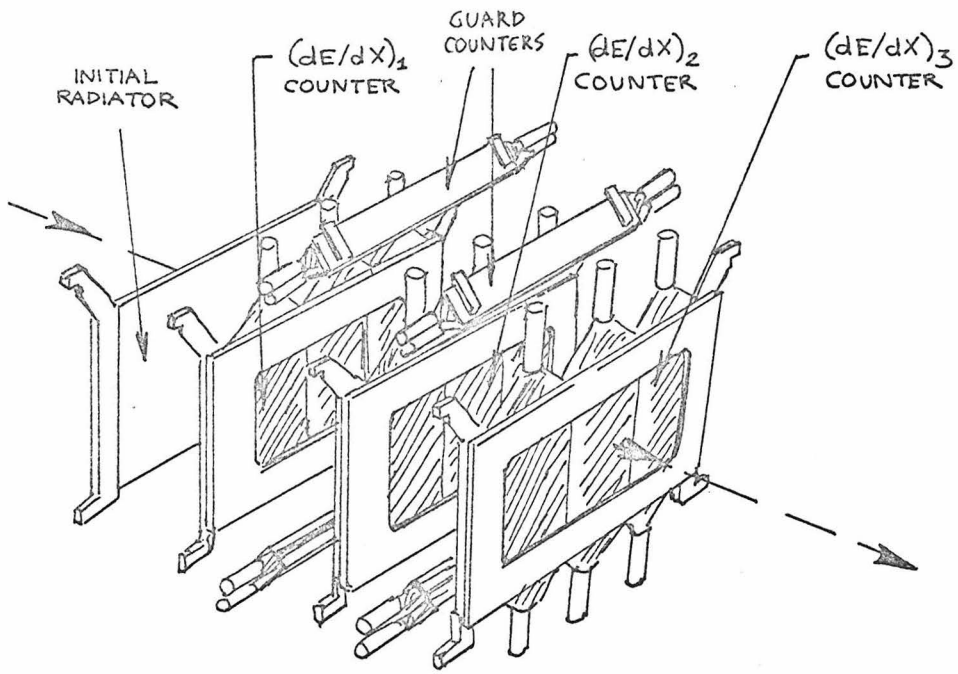

Front Section

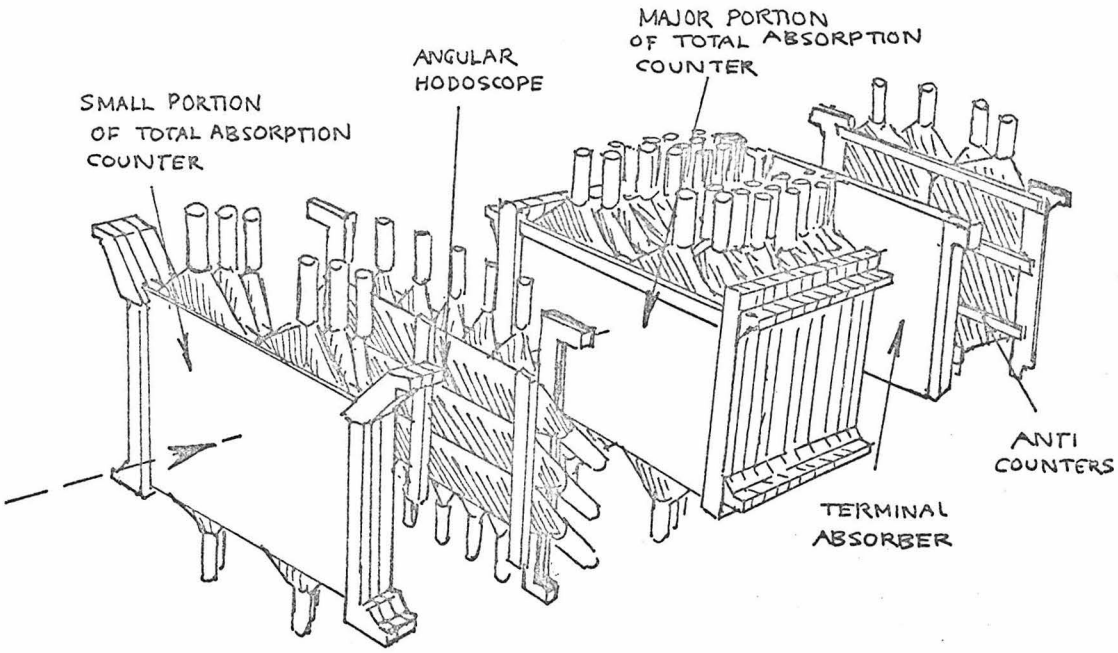

Rear Section

FIGURE 20: 8-GeV/c π-e Discriminator

The total absorption counter was made up of 16 lead-lucite slabs, which put 18 radiation lengths of material in the scattered particles path. The lucite was viewed by 64 phototubes whose outputs were linearly combined into a single output. The 18 radiation lengths were sufficient to cause an electron or positron to shower and lose almost all its energy and thus create a large output pulse - but not for a heavier mass pion.

Thus a discrimination between pions and electrons was made by requiring the TA pulse height to be greater than some minimum.

The dE/dX counter used was $(dE/dX)_1$ in Fig. 20, which was a combination of three $12^{15}/_{64}'' X 12^{31}/_{64}'' X^{1}/_{2}''$ scintillators placed behind a 0.5 r.l. thick lead sheet (labelled "initial radiator" in Fig. 20). An incoming electron has a high probability of showering in the initial radiator and sending two or more electrons (or positrons) through the dE/dX counter, whereas the probability of a pion doing this is very small. Thus a further discrimination between pions and electrons can be made by requiring the dE/dX pulse height to be greater than some minimum.

d. 8-GeV/c Electronics

As we mentioned at the beginning of this chapter (Section A), the electronics limited the event logging rate to a maximum of one event per pulse. The electronics was also used to transfer information regarding coincidences between counters and blocks of counters, pulse heights, and various counting rates (scalers) onto magnetic tape. This

enabled us to apply more stringent electronic conditions (e.g. requiring more coincidences to be satisfied than were required for data logging) during the data analysis. Details of how the electronics performed these functions will now be described.

An overall block schematic of the electronics for the 8-GeV/c system, as used in this experiment, is shown in Fig. 21.

The anode from each hodoscope photomultiplier was connected to a particular discriminator-coincidence circuit-discriminator (DCD) chain as shown in the lower part of Fig. 21. The DCD unit is functionally a discriminator with a fast gate and was utilized in the following manner.

An event, defined by a coincidence between the front and rear trigger counters (FT and RT in Fig. 21) and/or a large pulse in the TA counter, caused the toggle in Fig. 21 to switch to a "set" state. As the toggle transfered to the set state, a 40 nsec wide pulse was sent to the master fan (see Fig. 21) where it was fanned out so as to appear at each of the coincidence circuit inputs of the DCD's. If a signal appeared at the front discriminator of a DCD chain during the 40 nsec period when this was applied, an output appeared from the coincidence circuit, which triggered the rear discriminator in the DCD chain. The outputs from the DCD's were stored in the fast buffer (see Fig. 21), where it was later read into the computer.

Once the toggle was in a "set" state, it would not respond to any further signals at the set input until a pulse was applied to the

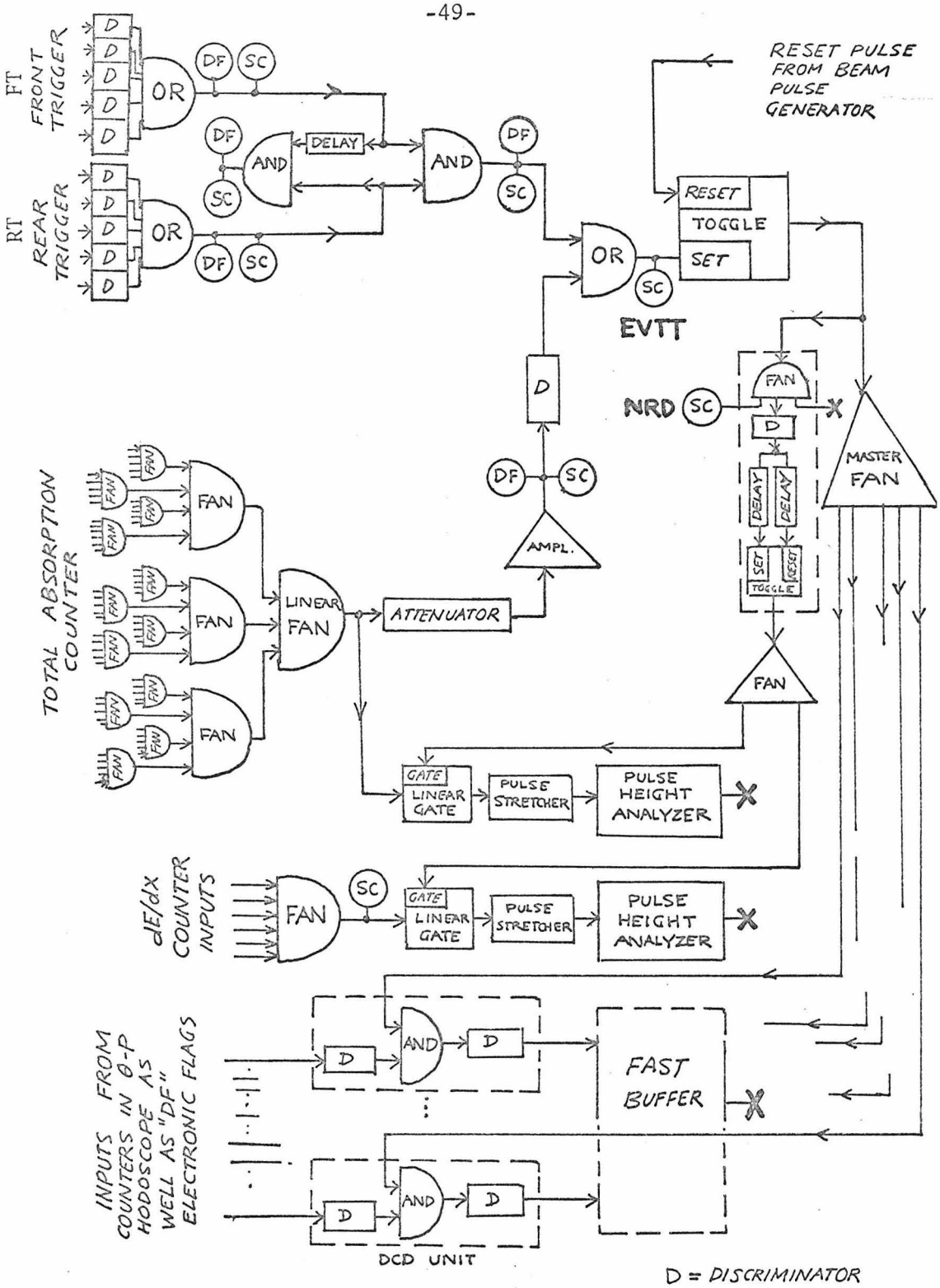

FIGURE 21: 8-GeV/c Electronics

toggle input labelled "reset" in Fig. 21. Thus the event rate was limited to a maximum of one per pulse.

At the same time that a 40 nsec pulse was generated along the master fan, a second output from the toggle was used to generate a wider pulse which opened the linear gates (see Fig. 21) for 60 nsec, allowing pulses from the TA and dE/dX counters to pass into their respective pulse height analyzers.

Scalers were attached to various points in the electronics (indicated by (SC) in Fig. 21) to monitor rates. In addition, DCD units of the type mentioned above, were attached to various spare outputs in the electronics (indicated by (DF) in Fig. 21). A signal at one of these outputs caused a particular binary bit in the fast buffer to be set, which was later read into the computer (and stored on tape) as an "electronic flag."

Between beam pulses, the fast buffer and the pulse height analyzer address registers were read by the on-line computer and the counter, pulse height and electronic flag information was transferred onto magnetic tape.

A separate data channel of the computer was used to sample occasional events and to do some on-line analysis. The size of the sample depended on the data rate as priority was given to the data logging. The on-line analysis included line printer and scope displays showing population distributions versus counter location, pulse height, missing mass of the undetected particles, position in the θ-p hodoscope plane,

as well as provided a continually revised estimate of the elastic cross section deduced from the sampling. Examples of the type of on-line scope displays are shown in Fig. 22.

The pulse height analyzers were Nuclear Data model 23-4, 128 channel analyzers. The DCD units were specially built Chronetics model 121A's. All other discriminators were model 120's. The dual input AND/OR units were Chronetics model 103's. The active fan-ins (the 4-fold fan-ins in Fig. 21) were Chronetics model 118's and the active fan-outs (fan-outs with 4 outputs in Fig. 21) were Chronetics model 108's. The passive fan-ins as used in the dE/dX counters and the last four fan-ins for the TA were Chronetics model 118 transformer fans. The remaining TA fan-ins were Chronetics model 44R resistive fan-ins.

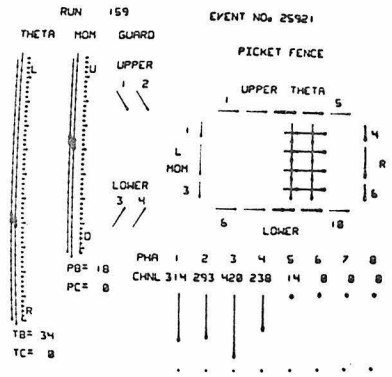

Single Event Display

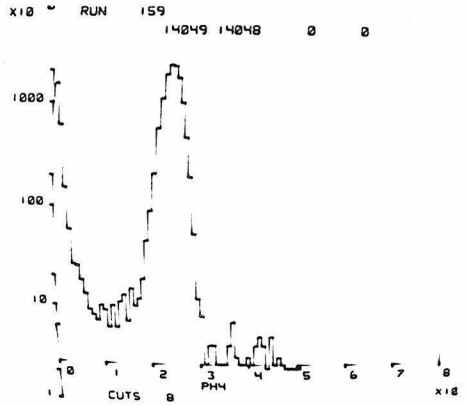

TA Pulse Height Event Distribution

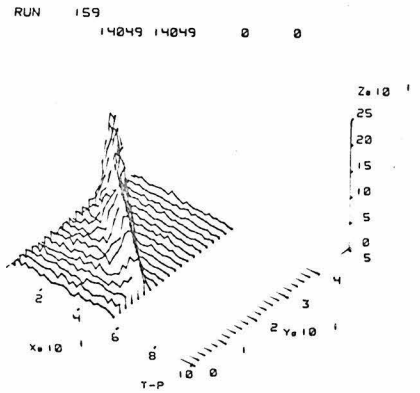

θ-p Hodoscope Two Dimensional Histogram

FIGURE 22: Examples of On-Line Scope Displays

2. 20-GeV/c Spectrometer System

a. General

The 20-GeV/c spectrometer, as used for this experiment, was similar to the 8-GeV/c spectrometer. The spectrometer consisted of four bending magnets, four quadrupoles and three sextupoles, physically arranged as shown in Fig. 16. As in the 8-GeV/c system, the optics are arranged so that particles are deflected in the vertical direction with point-to-point focusing in the vertical plane and parallel-to-point focusing in the horizontal plane. The thin lens equivalents of the magnets are shown in Fig. 23.

A 32-element scintillation counter hodoscope was placed in the horizontal (θ-measuring) focal plane to provide an angular resolution of ± 0.13 mrad. In the vertical (p-measuring) focal plane a 40-element scintillation counter hodoscope was used to provide a momentum resolution of $\pm 0.05\%$ $\Delta p/p$. As in the 8-GeV/c system, the p-focal plane was tilted (at a 43° angle with respect to the central ray) to minimize chromatic aberrations.

The azimuthal angular acceptance ($\Delta\phi$) was limited to $\sim\pm 3.9$ mrads by tungsten slits placed near the entrance window to the spectrometer. Thus, θ-ϕ mixing of the kind described earlier was even less than in the 8-GeV/c system.

The overall characteristics of the 20-GeV/c spectrometer are shown in Table I.

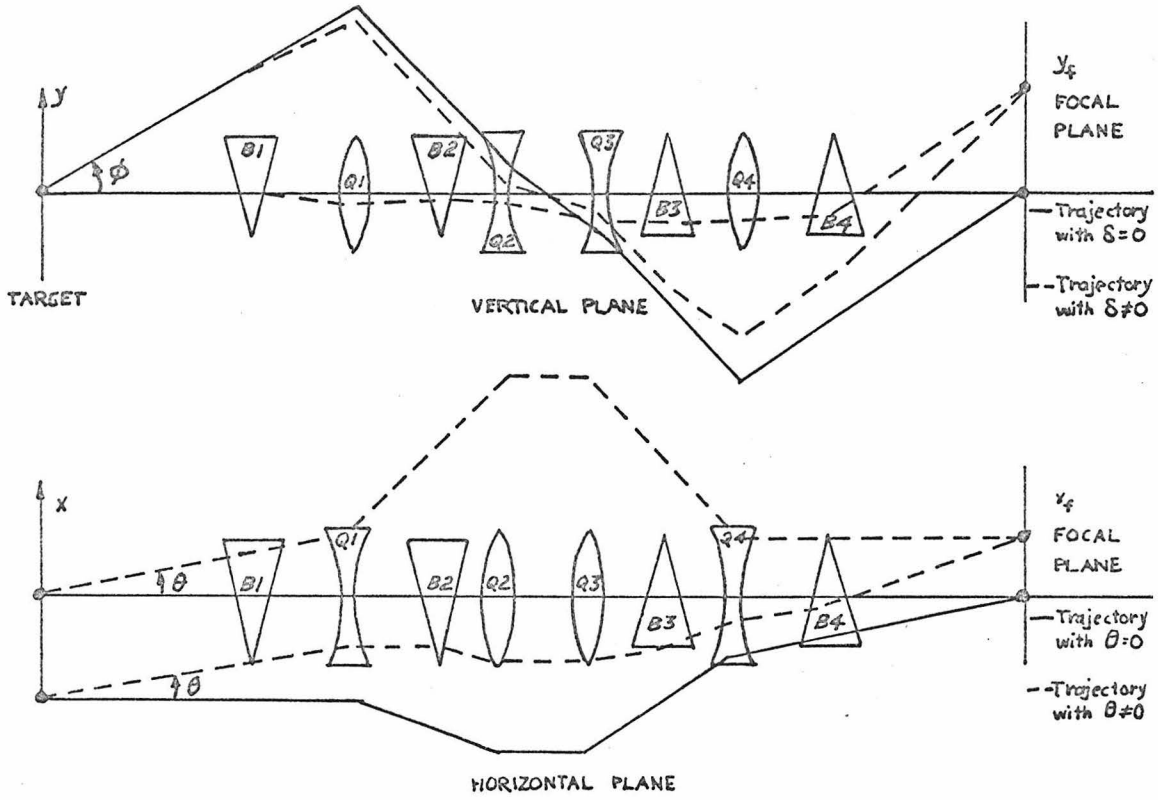

FIGURE 23: Thin Lens Equivalents of
Magnets in 20-GeV/c Spectrometer

b. Monitoring the Spectrometer Fields

The magnets in the 20-GeV/c spectrometer were monitored only by checking the current supplied to the magnets. As in the 8-GeV/c system, the on-line SDS 9300 computer monitored the current by reading the shunt voltages and comparing them to a standard table of voltages corresponding to that momentum setting. A deviation in any voltage by ±0.2 millivolts would cause the computer to signal the operator.

c. Spectrometer Detectors

The detection system in the 20-GeV/c spectrometer, as used in this experiment, consisted of only a hodoscope and a total absorption counter.

The hodoscope consisted of the θ and p hodoscope arrays described earlier, as well as three trigger counters (see Fig. 24). The first two trigger counters were in front of both θ and p hodoscopes and the last trigger counter was just behind the p-hodoscope.

The construction of the counters in the 20-GeV/c system was similar to those in the 8-GeV/c system. The scintillator material was NE102 in all cases and the phototubes were RCA 7767's for the θ and p counters, and RCA 8575's for the trigger counters.

The total absorption counter in the 20-GeV/c spectrometer consisted of a lead-scintillator sandwich made up of 8.76 r.l. of lead and 16 scintillators (see Fig. 24).

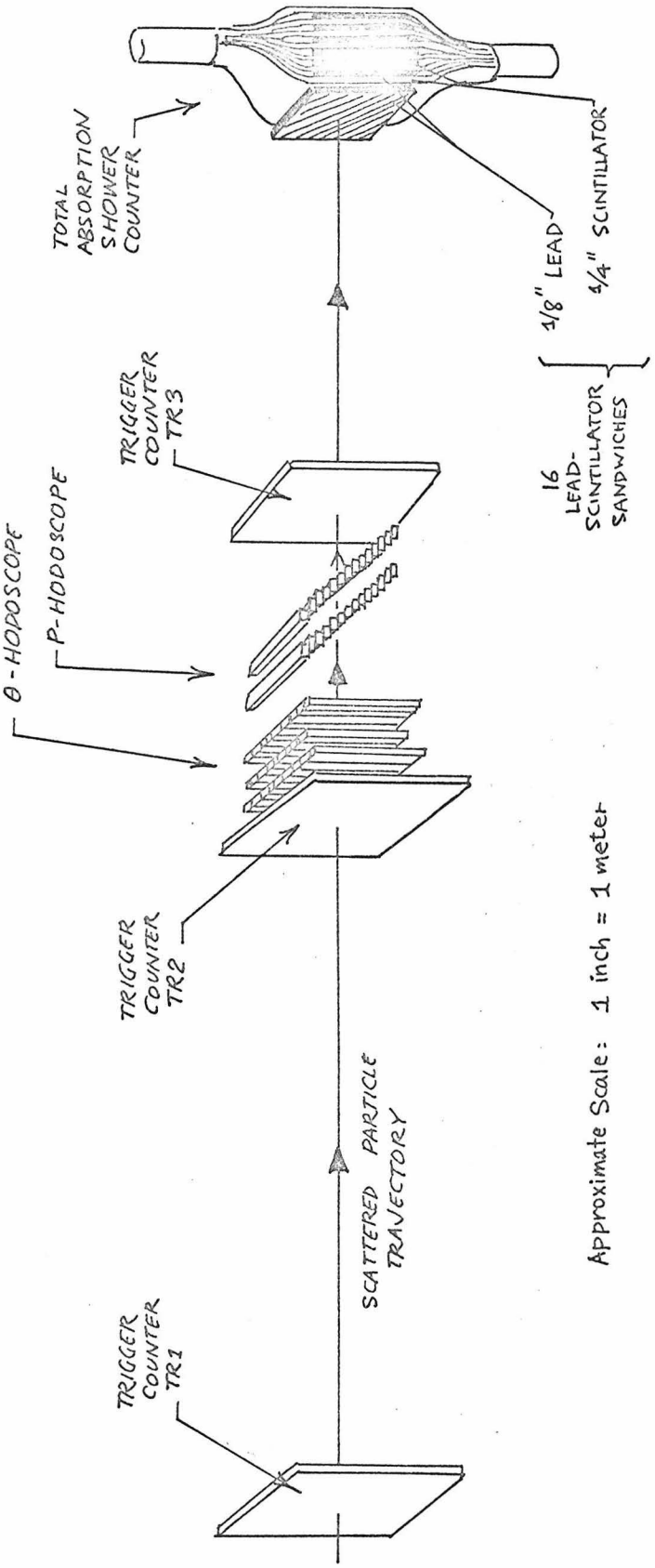

FIGURE 24:
Detection system in the
20-GeV/c spectrometer

d. 20-GeV/c Electronics

The electronics for the 20-GeV/c system, as used for this experiment, was very similar to that of the 8-GeV/c system. A block schematic of the 20-GeV/c electronics is shown in Fig. 25. Except for the absence of a dE/dX counter and the use of three trigger counters instead of two, the electronics was identical.

The mode of operation was completely analogous to the 8-GeV/c system. An event, defined by a coincidence between three trigger counters (TR1, TR2 and TR3 in Fig. 25) and/or a large pulse in the TA counter, caused the toggle to switch to a "set" state. As the toggle transferred to the set state, a 40 nsec wide pulse was sent to the master fan where it was distributed to the fast gate inputs of the DCD's, thus enabling the fast buffer to store information giving the location of the counters that fired during the 40 nsec. A separate fan was used to provide the fast gate input signals for the DCD's acting as electronic flags (see Fig. 25).

As in the 8-GeV/c system, the toggle remained in a "set" position and was unresponsive to further "set" pulses, until it was reset just prior to the next beam pulse. Thus again the event rate was limited to a maximum of one per beam pulse.

As in the 8-GeV/c system, a 60 nsec wide pulse was generated at the same time as the 40 nsec pulse was, and was used to open the linear gate connecting the total absorption counter to the pulse height analyzer.

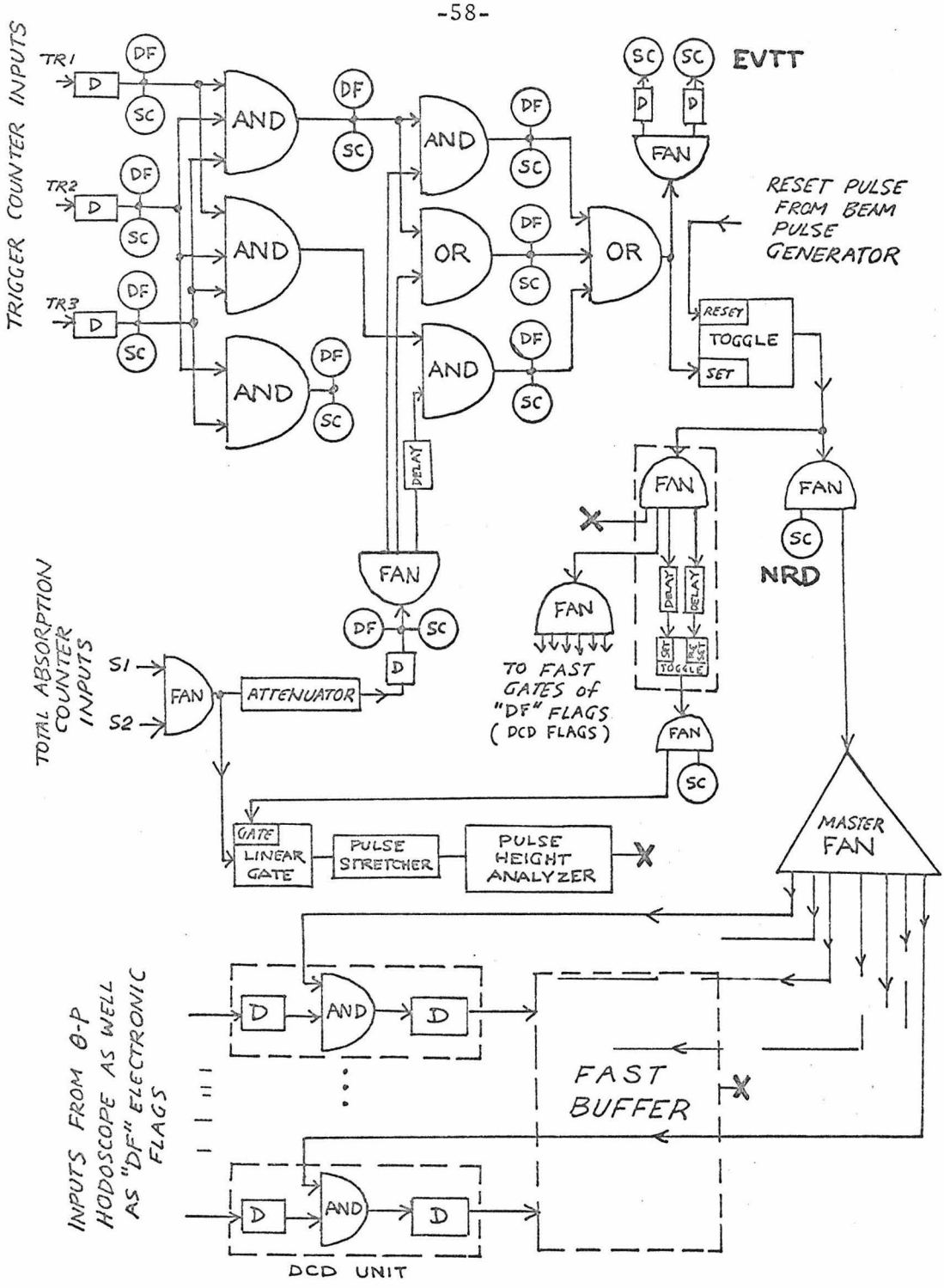

FIGURE 25: 20-GeV/c Electronics

D = DISCRIMINATOR
X = TO COMPUTER
SC = SCALER
DF = ELECTRONIC FLAG

The data logging was performed with the same SDS 9300 computer used in the 8-GeV/c system, and on-line analysis of data samples was performed whenever the data rate allowed.

The electronics used in the 20-GeV/c system were of the same type and manufacture as used in the 8-GeV/c system.

III. DATA ANALYSIS

A. Summary

This experiment concerned itself entirely with determining $R=d\sigma^+/d\sigma^-$ and no attempt was made to determine the absolute cross section, $d\sigma/d\Omega$, with any accuracy. The data was analyzed with this in mind.

As we mentioned earlier, R was determined from the number of electrons and positrons in a standard area in the background-subtracted θ-p hodoscope plane which contained the elastic peak. Electrons were distinguished from pions by requiring pulse heights in the total absorption and dE/dX counter to be greater than certain minima. The background subtractions were approximately 2% and had negligible effects upon the values of R. Corrections were made for small variations in incident energy and scattering angle as well as for electronic and computer losses. Corrections were also made for drift currents in the toroid beam charge monitor.

B. Distribution of Counts in the θ-p Plane

To explain precisely what counts in the θ-p plane were used to determine R, it is necessary to describe the distribution of counts in the θ-p plane. This will now be done.

In this experiment the kinematical conditions are the following: an electron or positron of known incident energy, E_o, scatters off a stationary proton. If the collision were truly elastic, i.e.,

$$e^{\pm}p \rightarrow e^{\pm}p \quad ,$$

then knowledge of the scattering angle, θ, of the electron would be sufficient to determine the scattered electron's momentum exactly. That is to say, there exists a curve in momentum-angle space on which all such scattered events will land. This curve, called the "elastic peak," is shown as a dashed line in the diagram (Fig. 26) of the θ-p space spanned by the θ and p hodoscopes.

However true elastic scattering occurs with essentially zero probability because of unavoidable radiative effects. In fact the scattering cannot occur without some low energy photon, i.e.,

$$e^{\pm}p \rightarrow e^{\pm}p\,\gamma \quad ,$$

being emitted[11].

One can obtain an intuitive feeling for this from the classical radiation of accelerated charges. The very act of scattering represents an acceleration (of both the electron and proton) and therefore unavoidably results in some radiation from the particles.

Aside from this intrinsic radiative loss, the electrons pass

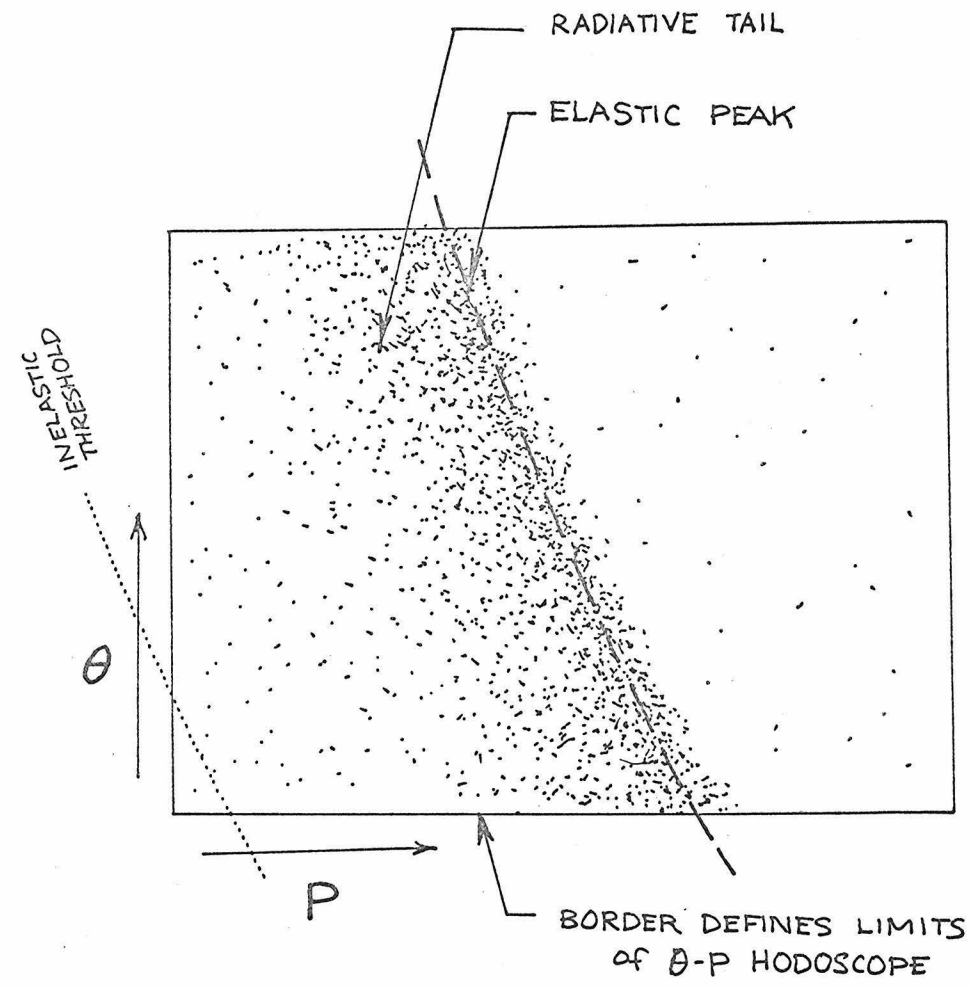

FIGURE 26: Typical Event Distribution
In the θ-p Hodoscope Plane - Dots
Represent Typical Events

through various materials such as vacuum windows, air, liquid hydrogen, etc. both before and after scattering. Long range Coulomb interactions between the electron's charge and the charges of the atoms inside the material will impart numerous little "accelerations" to the passing electron, also causing the electron to radiate.

Both this latter form of radiation, called Bremsstrahlung, and the previous intrinsic radiation, cause the scattered electrons to possess less energy than if they were truly elastic. Thus the scattered electrons will distribute themselves to the left of the dashed line in Fig. 26. The population decreases rapidly as one moves away from the elastic peak because the probability for radiating a photon decreases rapidly as the photon energy increases.

Such an event distribution is shown in Fig. 26 by the little dots, which represent scattered electrons. The clustering of events on both sides of the elastic peak may appear contrary to what was said earlier, but it is not really. This is because the incident energies of the electrons in the beam are not at a fixed E_o, but are instead distributed about E_o (full width $\leq 1\%$ $\Delta E_o/E_o$). Thus the dashed line in Fig. 26 really represents the mean elastic peak position of a distribution of elastic peaks. This explains why, although scattered electrons always appear to the left of their own elastic peak, they may appear to the right of the dashed line in Fig. 26. The few dots to the far right of the dashed line in Fig. 26 represent background.

Since true elastic scatterings do not actually occur, it is tra-

ditional to term "elastic," events that are elastic except for the radiative losses just described.

Since theoretical calculations of the elastic scattering cross sections (e.g., the Rosenbluth formula described earlier) deal with true elastic events and do not include radiative effects, it is necessary to correct the experimental "elastic" cross section before comparing with theory.

These radiative corrections will always increase the experimental cross sections, as they compensate for those "elastic" events that have lost so much energy that they cannot get into the apparatus (i.e., the events that fall outside the θ-p hodoscope plane because of radiative effects).

It should be mentioned that inelastically scattered electrons in general will land to the left of the elastic peak in Fig. 26. For example, electrons from the reactions:

$$e^{\pm}p \rightarrow e^{\pm}p\,\pi^{o} \qquad \text{and} \qquad e^{\pm}p \rightarrow e^{\pm}n\,\pi^{+}$$

will lie to the left of the line labelled "inelastic threshold" in Fig. 26.

C. The Quantity N/Q

Having discussed the θ-p plane, we can now discuss which counts in the θ-p plane were used to represent the experimental cross section. For a given experimental run, we will call the total number of such counts divided by the total beam charge, N/Q. After applying various corrections to the N/Q's, the ratio of the N/Q's for positrons and electrons was used to obtain R.

The quantity N equals the number of scattered particles whose total absorption counter and dE/dX counter pulse heights are greater than certain minima, that have produced a coincidence in the trigger counters, and that have landed in the θ-p hodoscope region R_s shown in Fig. 27.

The region R_s is a canonical area defined relative to the elastic peak. Thus A, B and C in Fig. 27 are fixed in all the runs of a given point.

Defining R_s relative to the elastic peak rather than the θ-p hodoscope plane has the advantage of reducing variations in N due to movements of the elastic peak. The elastic peak moved slightly between runs for the same data point because of small shifts in the incident beam energy, the spectrometer angle and the magnetic fields of the spectrometer. If R_s had been defined relative to the hodoscope plane, a shift in elastic peak position, say to the left in Fig. 27, would have the effect of eliminating a segment of counts in the radiative tail, which would have affected N considerably. However, by de-

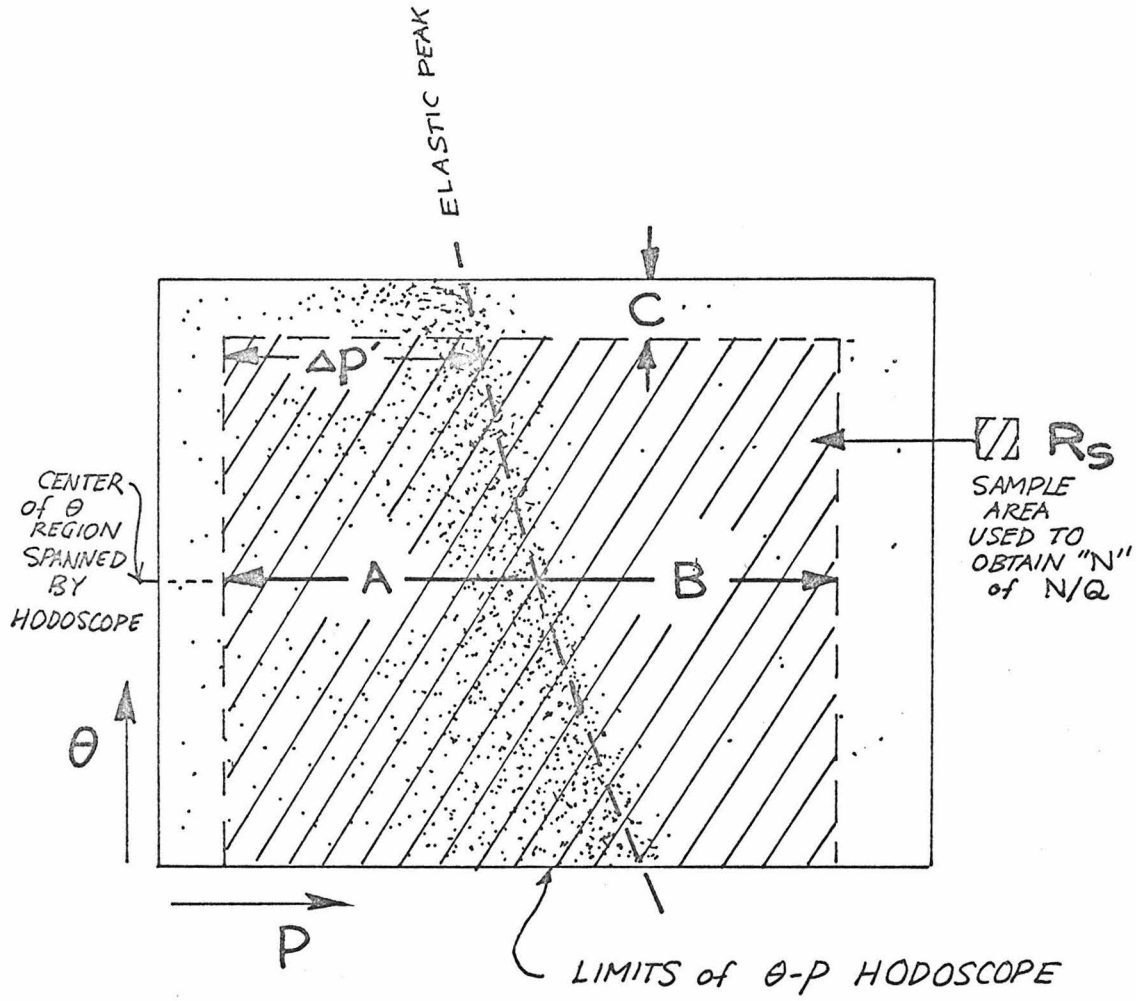

FIGURE 27: Diagram defining sample area, R_s, used to obtain "N" of N/Q. Quantities A, B, and C are fixed for all the runs of a given data point.

fining R_s relative to the elastic peak, the only variation in N due to a movement of the elastic peak would be that due to the change in solid angle acceptance. This effect is discussed later where it is shown to be negligible.

The values of A and B are chosen so that R_s remains on the θ-p hodoscope plane for all runs of a given data point.

The elimination of counts from a strip of width C (see Fig. 27) was necessary when the slope of the elastic peak allowed the peak to approach too closely to the left edge of R_s. The radiative corrections are very large and less reliable when $\Delta p'$ in Fig. 27 approaches the width of the elastic peak. A nonzero C was required only for the data points E_o=10 GeV, θ=12.5^o and E_o=10 GeV, θ=15.0^o.

The different R_s's used in this experiment are shown in Fig. 28.

The position of the elastic peak in a given run was obtained by first sliding all the events to the central θ in R_s (see Fig. 29), then plotting the event distribution v.s. p on semi-logarithmic paper, and then comparing the peak positions with a standard template. The uncertainty in the peak position and the corresponding uncertainty in N by this method, was found to be very small as is shown later in the discussion on errors. A typical slid-distribution is shown in Fig. 30.

N/Q is obtained by simply dividing N by the total incident beam charge. The corrections applied to N/Q will be described later.

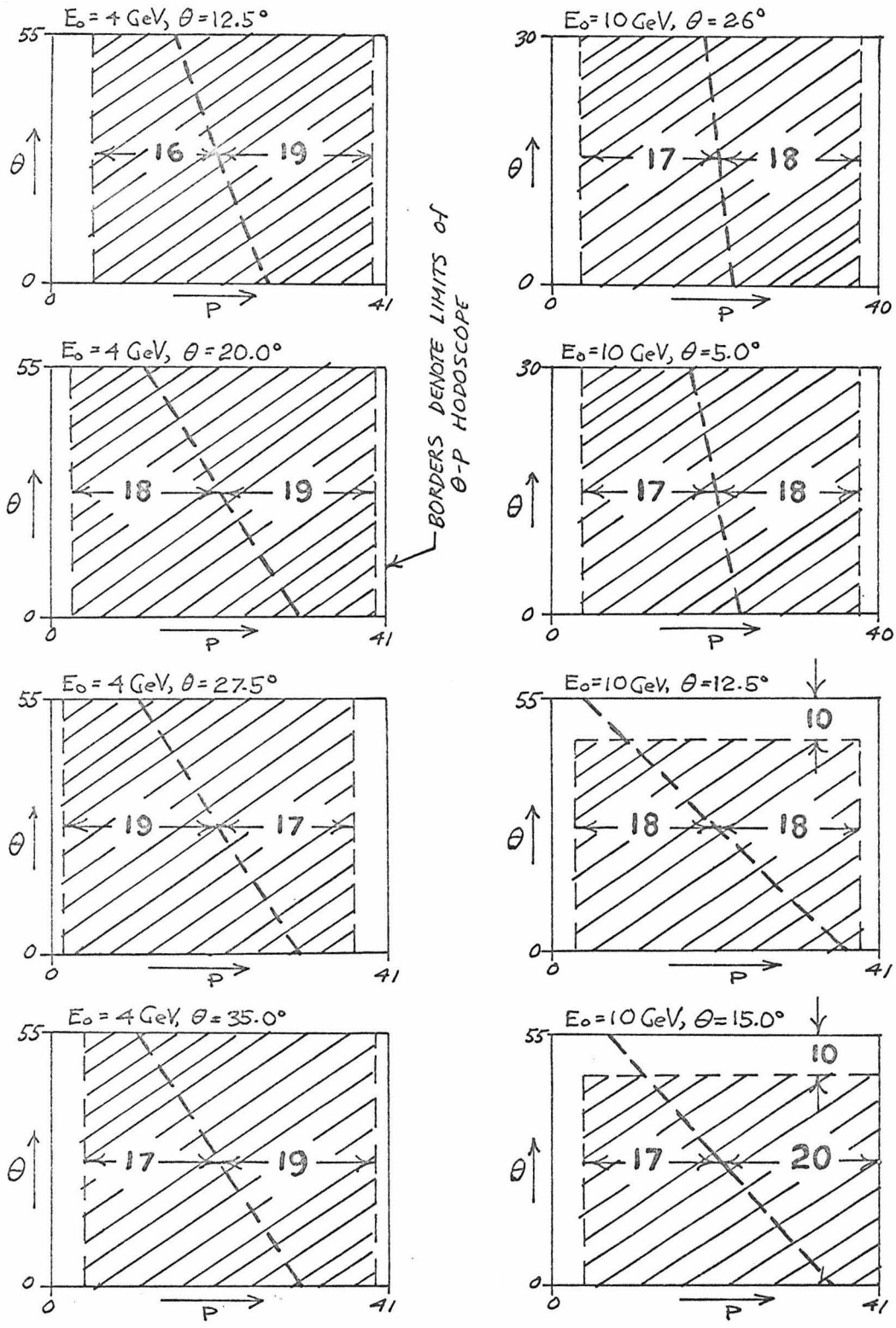

FIGURE 28: The R_s sample regions used for each data point

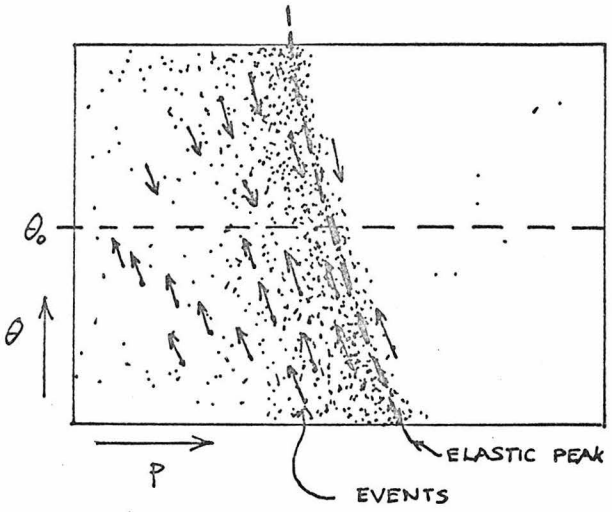

FIGURE 29: Sliding events in θ-p hodoscope plane to a common angle, θ_o

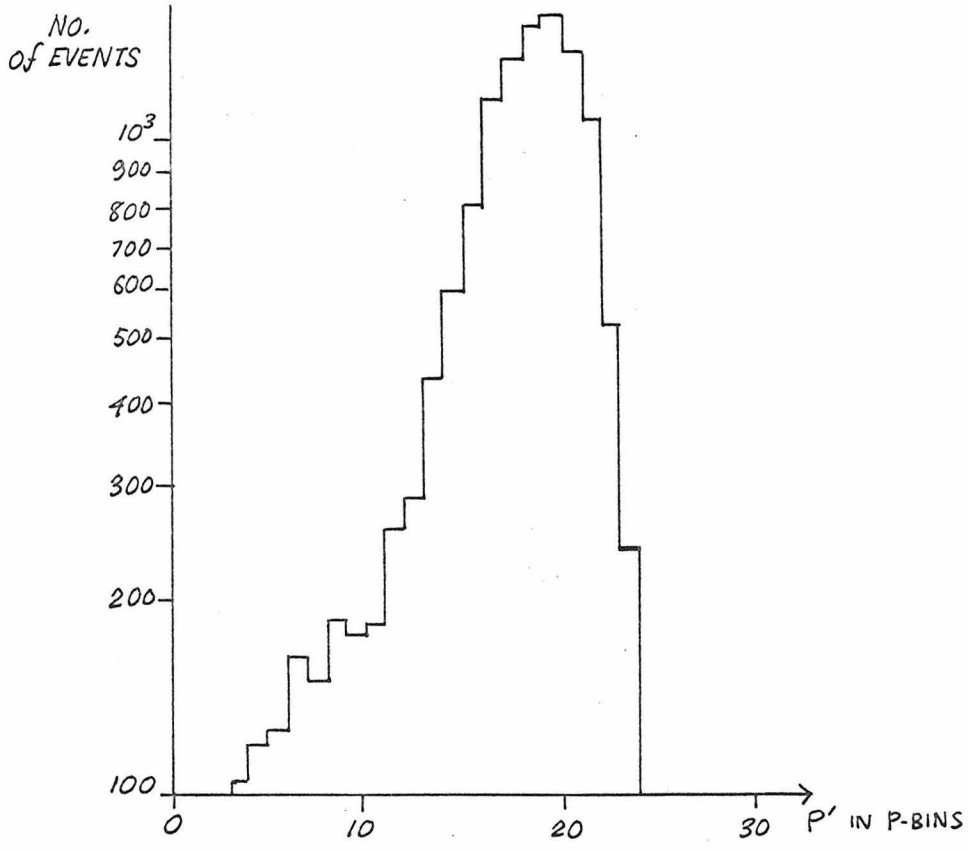

FIGURE 30: Typical slid-distribution

D. Pion Rejection

In the preceding, we assumed that N of N/Q included only electron events. It is worthwhile at this point to describe the method used to reject pions from the data.

As was mentioned earlier, pion events were identified from electron events by measuring the pulse heights in a total absorption (TA) shower counter and a dE/dX counter. It turned out that the shower counter provided adequate π-e rejection in all except the largest angle data ($\theta=35^{o}$), where the use of a dE/dX counter was necessary.

A typical pulse height spectrum observed in the TA counter is shown in Fig. 31a. The peak of the pion distribution is clearly separated from the electron peak; however, the two distributions are very close. The peak labelled "pedestal" in Fig. 31a is caused by an internally generated square pulse which the TA pulse adds to (see Fig. 32). This "false" peak was used to distinguish zero pulse height events (i.e., no events) from events with pulse heights greater than the maximum channel of the analyzer (which are put in channel "0"). The pedestal also provided a monitor of the gain stability of the pulse height analyzer.

If one now looks at only those events that have fired the set of trigger counters and which appear in both the θ and the p hodoscopes, then the pion and electron distributions separate considerably (see Fig. 31b).

By requiring the pulse heights to be greater than the "TA CUT"

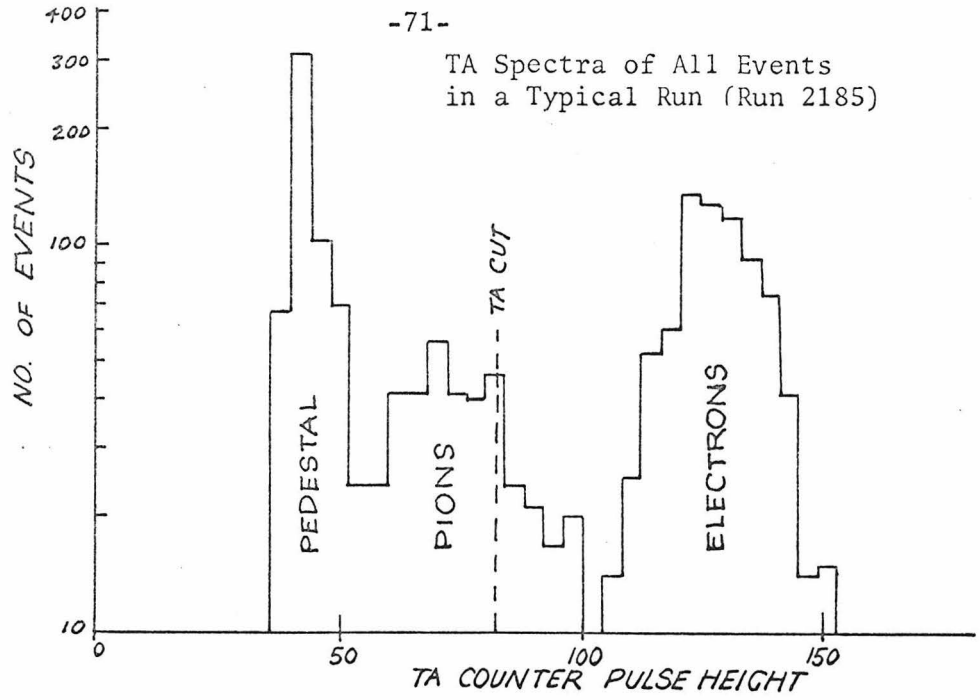
TA Spectra of All Events
in a Typical Run (Run 2185)
NO. OF EVENTS
400
300
200
100
10
0
50
100
150
TA COUNTER PULSE HEIGHT
PEDESTAL
PIONS
TA CUT
ELECTRONS

(a)

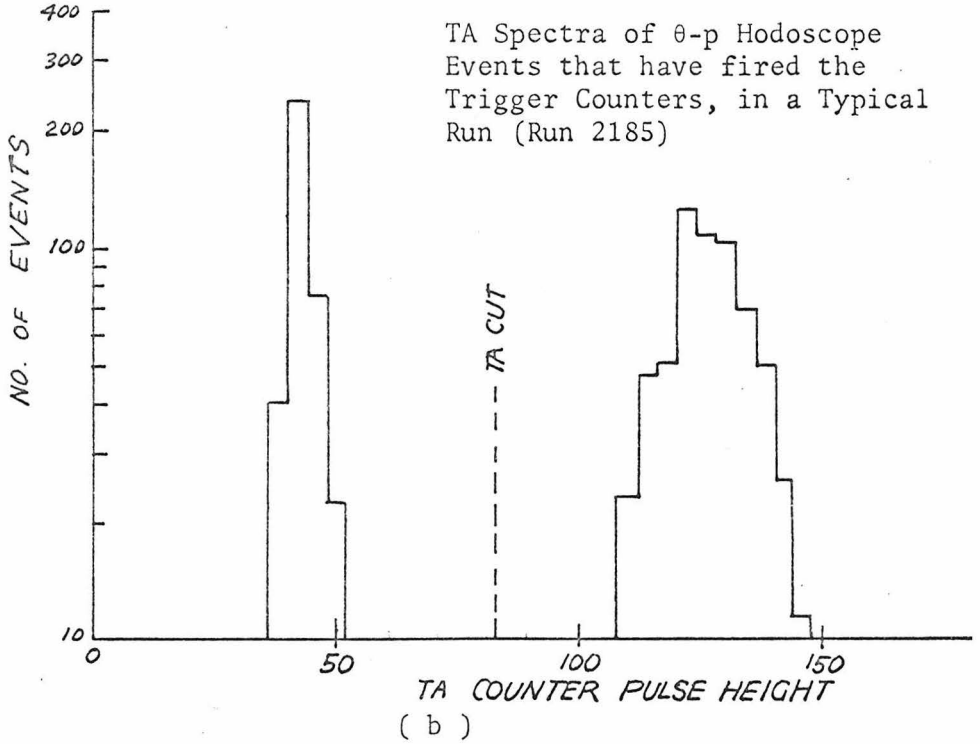
TA Spectra of θ-p Hodoscope
Events that have fired the
Trigger Counters, in a Typical
Run (Run 2185)
NO. OF EVENTS
400
300
200
100
10
0
50
100
150
TA COUNTER PULSE HEIGHT
TA CUT

(b)

FIGURE 31

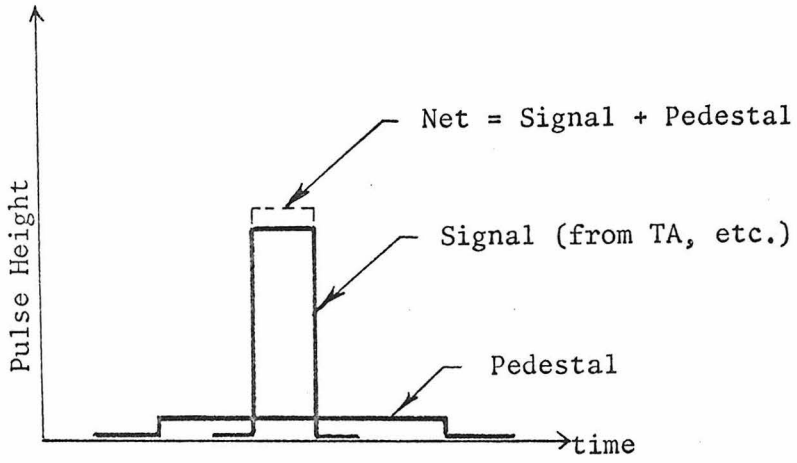

FIGURE 32:

Nonzero Pulse Height
Base Formed by Pedestal

in Fig. 31b, we can reject the pions with close to 100% efficiency in most of the data. In high statistics data, the wings of the two distributions still overlap (see Fig. 33), so choosing the position of the TA CUT is less clear.

In such cases we have chosen the TA CUT closer to the electron peak than the pion peak for the following reason. The beam interacts with more protons than neutrons so we expect the reactions:

$$e^{\pm} p \rightarrow e^{\pm} n \pi^{+}$$

and

$$\gamma p \rightarrow n \pi^{+}$$

to occur more frequently than:

$$e^{\pm} n \rightarrow e^{\pm} p \pi^{-}$$

and

$$\gamma n \rightarrow p \pi^{-}$$

In addition, pions may be photoproduced by gamma rays from annihilating positrons, whereas no such mechanism exists for electrons. Therefore, we expect the pion contamination to be greater in the positron data than in the electron data. Because of this asymmetry, it is important to eliminate all pions.

By taking the TA CUT close to the electron peak we avoid contaminating our data with pions at the expense of losing some electrons or positrons. However, since we do not observe nor expect any difference in the shape and position of the e^{+} and e^{-} distributions, we will lose the same fraction of e^{+} and e^{-} events, providing we use the same TA CUT for both. Thus, although the absolute cross section will be affected, the value obtained for R will not.

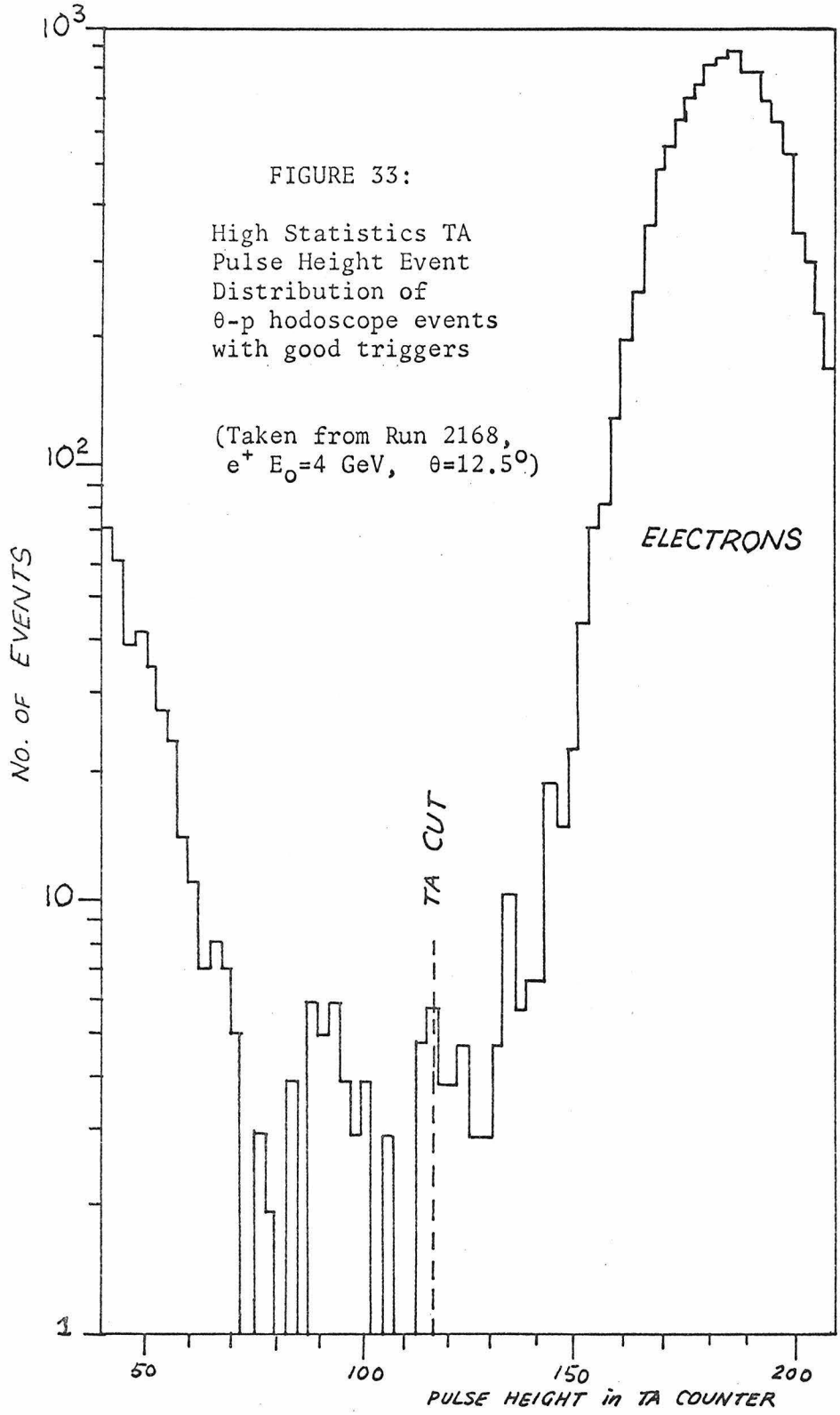

FIGURE 33:

High Statistics TA Pulse Height Event Distribution of θ-p hodoscope events with good triggers

(Taken from Run 2168, e^+ E_o=4 GeV, θ=12.5°)

Typical TA pulse height distributions for each data point are shown in Fig. 34. Note that aside from the 35^{o} data, the only data points in which there is reasonable ambiguity in the positions of the TA CUT are the E_{o}=4.0 GeV, $\theta=12.5^{o}$ and 20.0^{o} points, where we have taken the TA CUTs close to the electron peaks. It should be mentioned, however, had we taken the TA CUT as low as 80 in Fig. 34a and Fig. 34b, we would have changed N/Q by less than 0.3% and 0.5%, respectively.

For the $\theta=35^{o}$ point (see Fig. 34d) the separation between the pion and electron distributions is considerably less distinct. A measure of the pion contamination here was obtained by studying the event distribution in the "missing mass - pulse height" plane shown in Fig. 35.

The horizontal axis, labelled "missing mass" gives the equivalent mass of the undetected particles if one assumes the detected particle is an electron or a positron. The expression used to calculate the missing mass is given in Appendix B. The vertical axis gives the pulse height in the total absorption counter. The dots represent typical events.

Events in area C are predominantly elastic electron events used to make up the major portion of N/Q. The diminishing distribution to the left portion of C represents the radiative tail. The "x" represents the position of the elastic peak.

Events in area B are events with pulse heights in the electron peak but which land above the kinematical limit of the elastic peak (i.e. to the far right in Fig. 26).

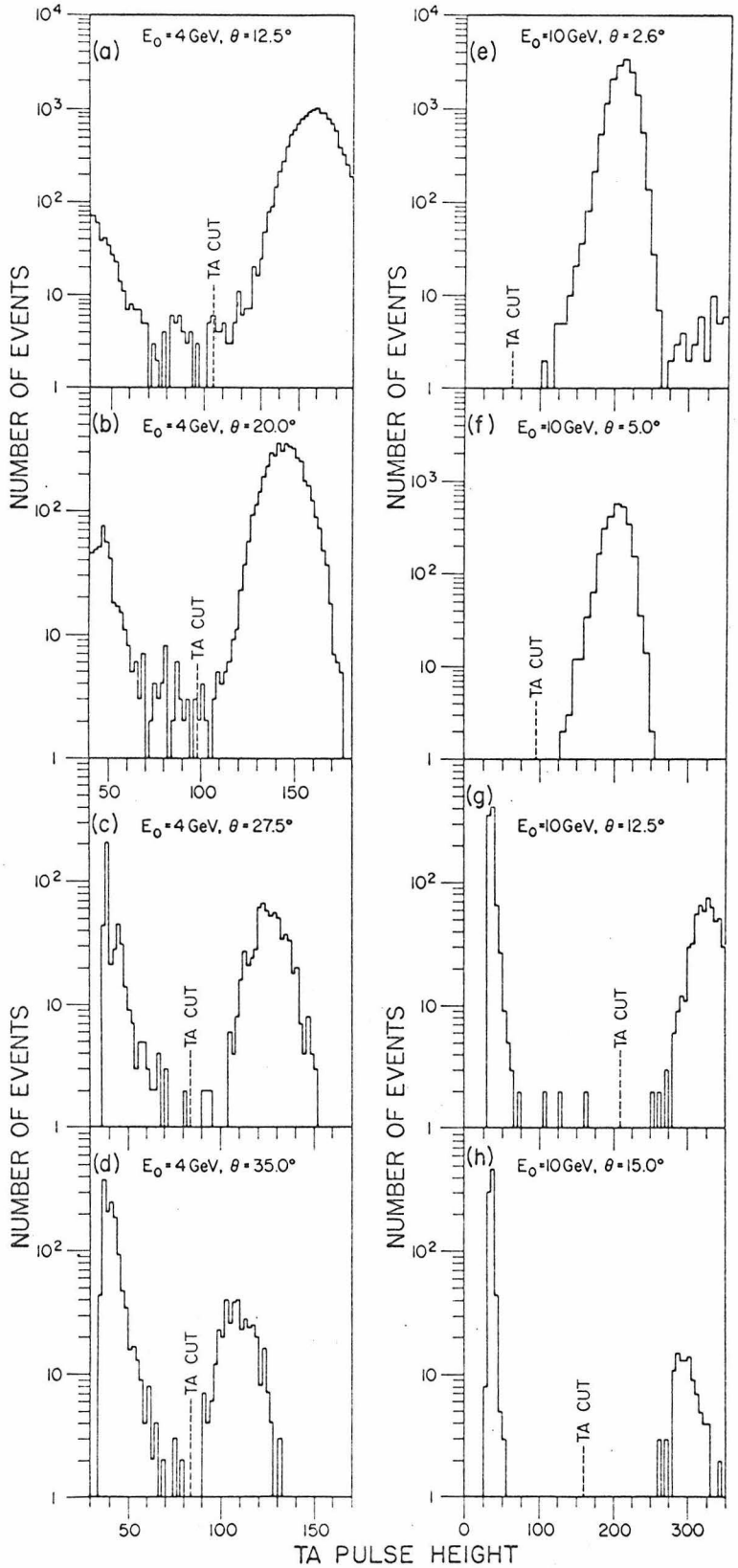
(a) E_0 = 4 GeV, θ = 12.5°
(b) E_0 = 4 GeV, θ = 20.0°
(c) E_0 = 4 GeV, θ = 27.5°
(d) E_0 = 4 GeV, θ = 35.0°
(e) E_0 = 10 GeV, θ = 2.6°
(f) E_0 = 10 GeV, θ = 5.0°
(g) E_0 = 10 GeV, θ = 12.5°
(h) E_0 = 10 GeV, θ = 15.0°
TA CUT
NUMBER OF EVENTS
TA PULSE HEIGHT

FIGURE 34.

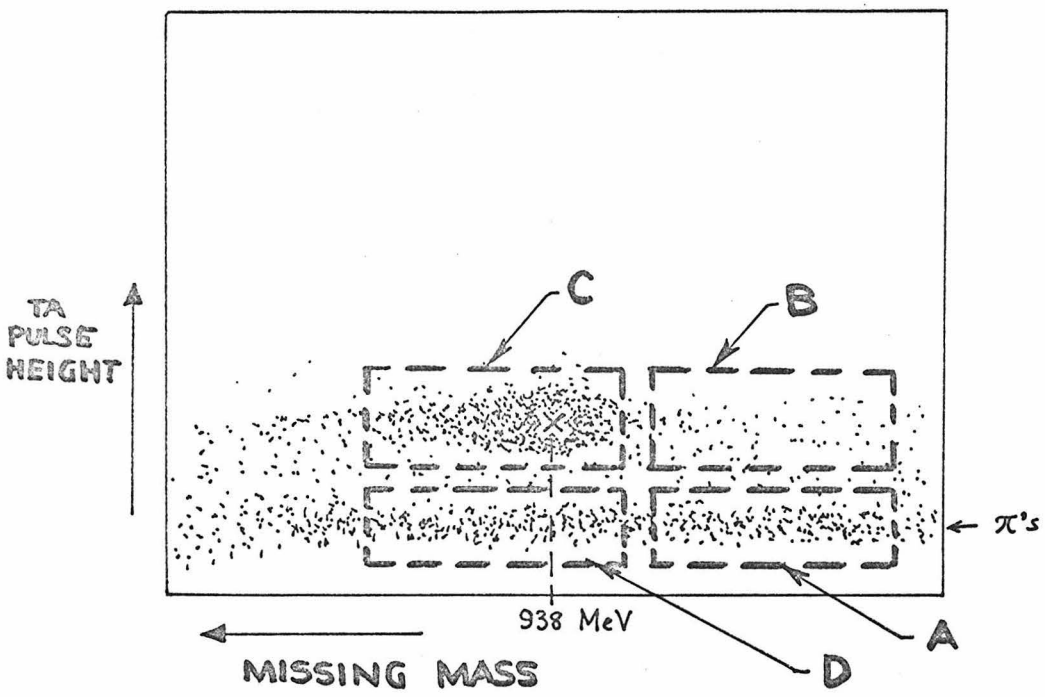

FIGURE 35:
Missing Mass - TA pulse height
Scatter Plot
(Dots represent typical
events)

The widely spread distribution of which A and D are a part, represent the pions which are spread throughout the θ-p plane and therefore represent a large range of missing mass.

If the number of events in A, B, C, and D are N_A, N_B, N_C, and N_D, respectively, then a measure of the pion contamination in C is given by:

$$N_{\pi/e} = \frac{\text{No. of } \pi\text{'s in C}}{\text{No. of e's in C}} \lesssim \frac{N_D(N_B/N_A)}{N_C}$$

The "less than" sign is because some of the events making up B may be due to electrons that have quasi-elastically scattered off the target walls. However, this will not affect the argument to follow as the quasi-elastic contribution will be the same for electrons and positrons.

Calculating this ratio for the 35^o e^+ and e^- data, we obtain:

$$N_{\pi^+/e^+} \lesssim (8.5 \pm 2.9) \times 10^{-2}$$

$$N_{\pi^-/e^-} \lesssim (2.7 \pm 1.0) \times 10^{-2}$$

Thus, were we to use only the total absorption counter, we would expect the pion contamination to contribute as much as a (6±3)% deviation in the value for R.

To reduce this asymmetry to a negligible level, one dE/dX counter was used. A typical pulse height distribution in a dE/dX counter appears as shown in Fig. 36. By requiring the dE/dX pulse height to be greater than the line labelled "dE/dX CUT," we eliminate the majority of the pions at the expense of eliminating some electrons. However,

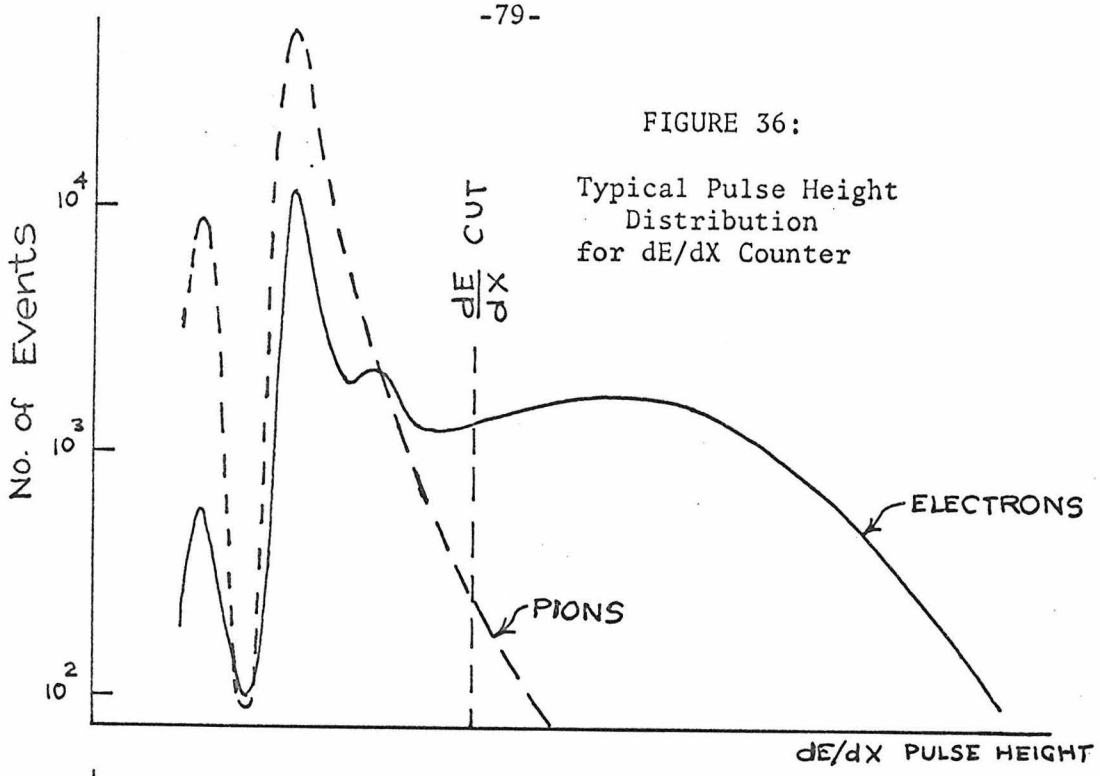

FIGURE 36:

Typical Pulse Height Distribution for dE/dX Counter

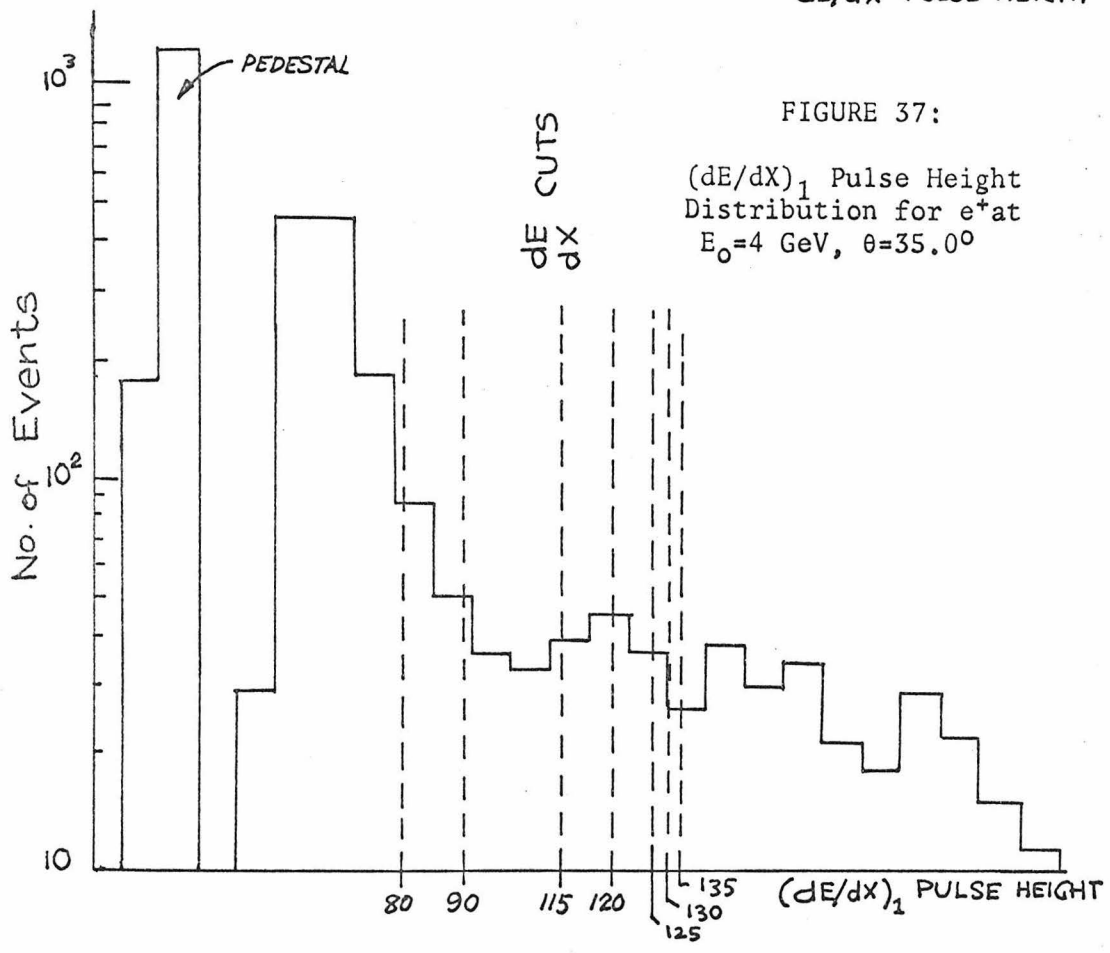

FIGURE 37:

$(dE/dX)_1$ Pulse Height Distribution for e^+ at E_0=4 GeV, θ=35.0°

by the same argument used earlier, the loss of some electrons will reduce the statistical accuracy but will not change the value for R.

The actual dE/dX pulse height distribution for the 35^{o} data is shown in Fig. 37. Various dE/dX CUTs were applied to the data at the places shown in the figure.

By looking at the decrease in events in the area about the elastic peak in Fig. 35 the dE/dX electron detection efficiency was estimated to be (89±3)% with a dE/dX CUT of 80 and (64±6)% with dE/dX CUT of 130. By looking at a low pulse height strip (across A and D in Fig. 35) the dE/dX pion detection efficiency at these two CUTs was estimated to be (30.3±1.3)% and (11.5±0.8)%, respectively.

Thus with a dE/dX CUT of 80, we would expect the π-e rejection to be increased by a factor 3. This would reduce the pion asymmetry to less than (2±1)%.

If a dE/dX CUT of 130 was used, then the π-e rejection would be increased by a factor of $\sim$6. This would reduce the pion asymmetry to less than (1±½)%. However, the statistical uncertainty increases from ±11% (for a dE/dX CUT of 80) to ±13%, so that the overall uncertainty is increased by using the larger dE/dX CUT.

A plot of R versus various dE/dX CUTs is shown in Fig. 38. Note that the application of a dE/dX CUT greater than 80 reduces R by about (8±3)%, which is consistent with the dE/dX π-e rejections just discussed and our (6±3)% estimate of the pion asymmetry. As expected, beyond a certain point, increasing the dE/dX cut does not change R. The

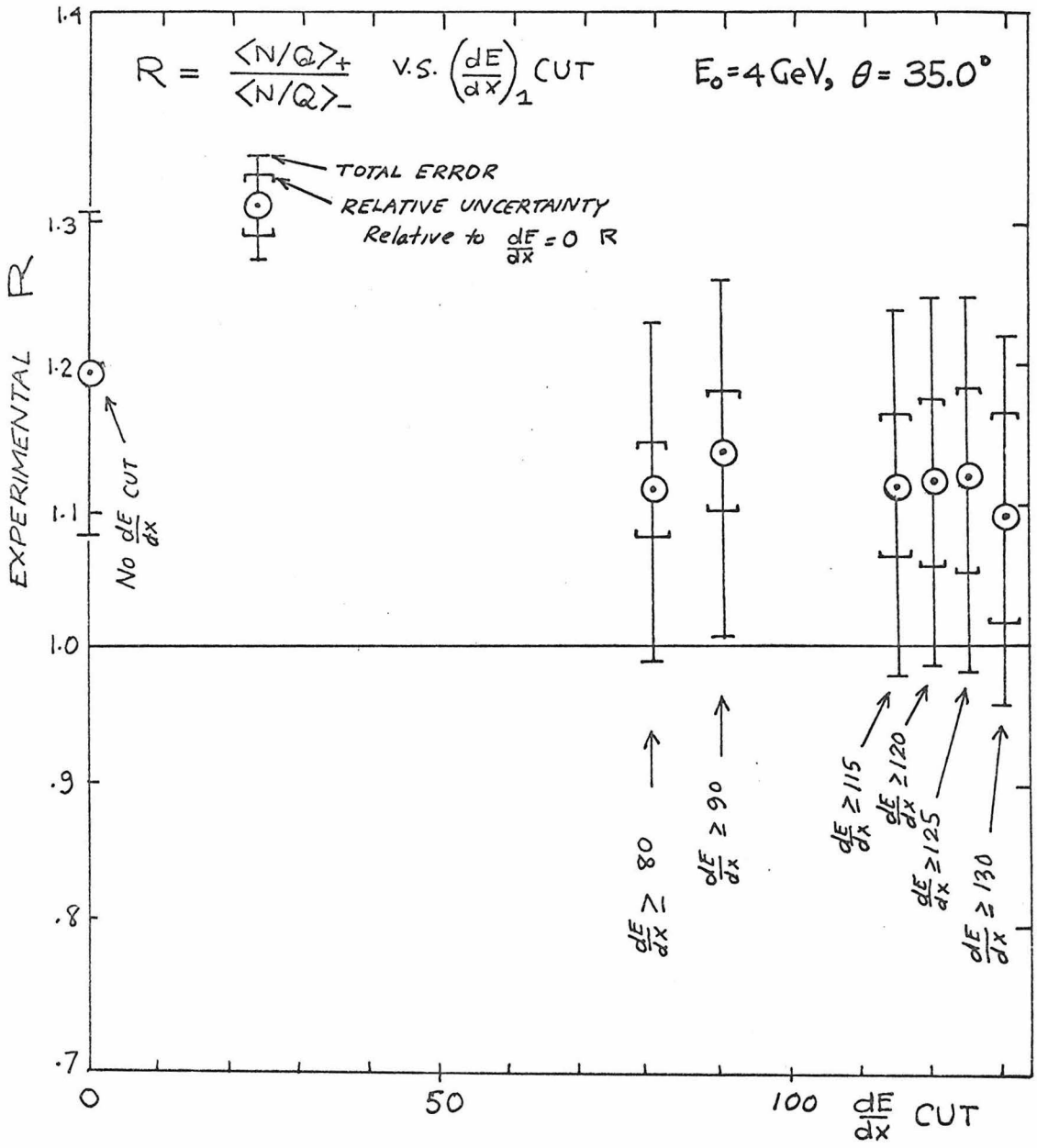

FIGURE 38:
Plot of R v.s. $(dE/dX)_1$ CUT, for E_o=4 GeV, θ=35° point

final dE/dX CUT chosen for the data analysis of the 35^{o} data was the one at $(dE/dX)_1$=80.

To further check that there was no e^+/e^- asymmetry in the dE/dX electron efficiency, we applied the same dE/dX conditions to the E_o=4 GeV, $\theta=27.5^{o}$ data that were run with the same beams as the 35^{o} data. Since the pions are effectively eliminated by the TA counter here, we would not expect the dE/dX counter to affect R.

Two dE/dX CUTs were used, one at 80 and one at 130. The dE/dX electron efficiency at each of these CUTs was (86.8±1.3)% and (63.0 ±3.3)% and the pion efficiency was likewise (32.7±2.1)% and (13.6± 1.2)%, respectively. These efficiencies are comparable to those in the 35^{o} case. A plot of R v.s. these dE/dX CUTs for the 27.5^{o} point is shown in Fig. 39. Note that within the relative statistical uncertainty, R does not change. This confirms our earlier assumption that the dE/dX electron and positron detection efficiencies were equal.

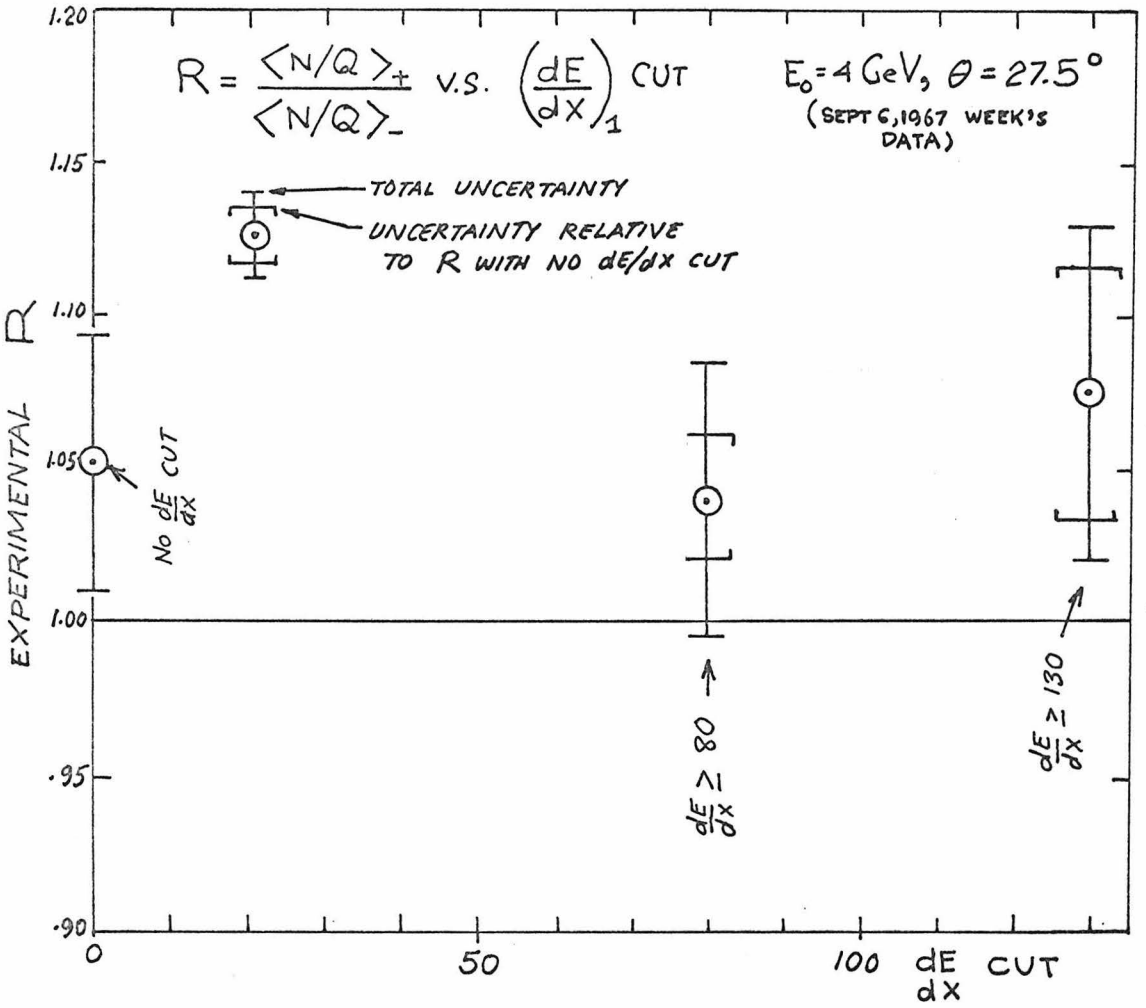

FIGURE 39:
Plot of R v.s. $(dE/dX)_1$ CUT, for E_o=4 GeV, θ=27.5° point

E. Corrections to N/Q

For each data point a number of runs were taken alternating with positrons and electrons, as mentioned earlier. In each run an N/Q was obtained and a number of multiplicative corrections, specific to the particular run, was applied.

The corrections were the following:

1) Difference in the radiative correction between e^+ and e^-, C_1.
2) Deviation of spectrometer angle from a canonical angle, C_2.
3) Deviation of incident energy from a canonical energy, C_3.
4) Ambiguous events (such as double tracks), C_4.
5) Trigger counter inefficiency, C_5.
6) Toroid drift correction, C_6.
7) Solid angle acceptance variation with variation in the position of the elastic peak, C_7.
8) Electronic dead time, C_8.
9) Computor sampling losses, C_9.
10) Background subtraction, C_{10}.
11) Steering correction due to earth's magnetic field, C_{11}.

These corrections are described in detail in the following sections:

1. Difference in Radiative Correction Between e^+ and e^-, C_1

The intrinsic radiative correction described earlier (Section B of this chapter) is different for e^+p and e^-p elastic scattering. This is because the interference between the amplitudes for a photon coming off the lepton line and for a photon coming off the proton line (see Fig. 40) occurs with opposite signs for electrons and positrons.

To illustrate how the radiative corrections were applied, let us suppose the sample area, R_s, is of the shape indicated in Fig. 41, where the left edge of R_s is a constant distance $\Delta E'$ away from the elastic peak (compare this with the sample area in Section C of this chapter, Fig. 27).

The radiative effects described earlier take what otherwise would have been events on the elastic peak and distribute them to the left of the elastic peak. Thus for a given elastic peak, the radiative correction can be characterized by the parameter $\Delta E'$, which is a measure of "how much" of the elastic events is retained. The larger $\Delta E'$, the smaller the radiative correction.

The radiative correction factor is written in either the form $(1+\delta)$ or e^{δ}, where δ is a negative function of $\Delta E'$ and kinematical quantities such as incident and scattered electron and proton momenta. If the sample volume can be characterized by a single $\Delta E'$ (as in Fig. 41), the experimental cross section is equal to the theoretical elastic cross section times $(1+\delta)$ or e^{δ}. Theoretical calculations[12] of the lowest order radiative corrections give the corrections in the form

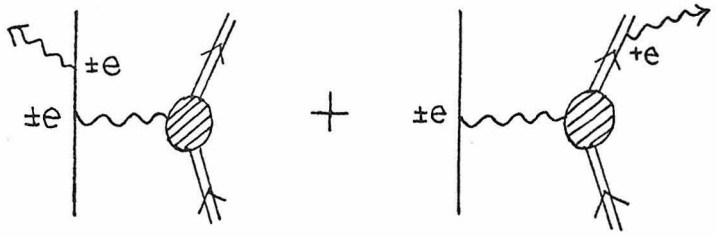

FIGURE 40:

Interference between radiation diagrams with one photon off the electron and proton line, is opposite in sign for e^+ and e^- - producing a difference in the radiative corrections for e^+ and e^-

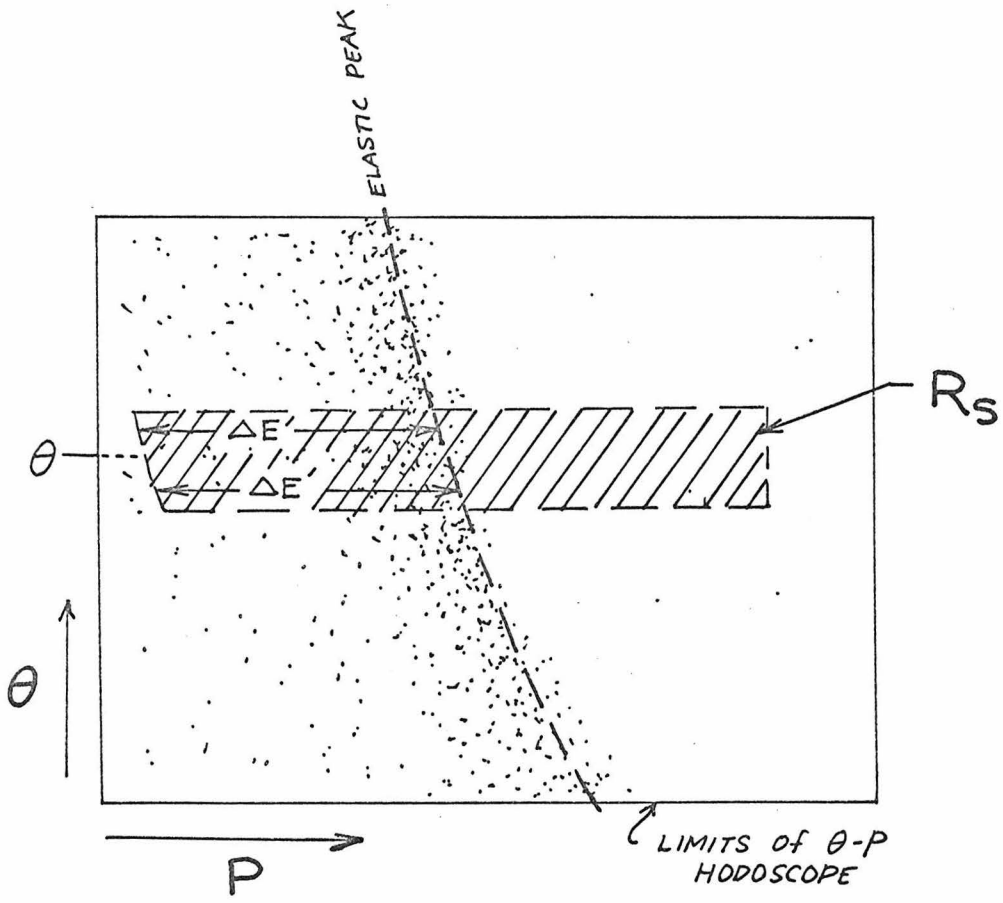

FIGURE 41: θ-p Hodoscope Plane with sample region, R_s, such that the left edge is a constant distance ΔE' from the elastic peak

$1+\delta$. However, there are arguments that indicate e^{δ} to be the correct form when all orders are included, so we have used the form e^{δ} in this experiment.

Therefore, if we use the Rosenbluth formula to predict the number of electrons (N_s) that will elastically scatter into R_s of Fig. 41, we get the following:

$$N_s^- = N_{in}^- \Delta\Omega(\theta) \left(\frac{d\sigma}{d\Omega}\right)_\theta e^{\bar{\delta}(\Delta E') + \delta_B(\Delta E')}$$

Where:
- N_{in}^- = total number of incident electrons
- $\Delta\Omega(\theta)$ = average solid angle acceptance into R_s
- $\left(\frac{d\sigma}{d\Omega}\right)_\theta$ = average Rosenbluth cross section in the angular region spanned by R_s
- $\bar{\delta}(\Delta E')$ = intrinsic radiative correction for e^-p elastic scattering
- $\delta_B(\Delta E')$ = Bremsstrahlung radiative correction

Similarly, had we used positrons instead of electrons we get the prediction:

$$N_s^+ = N_{in}^+ \Delta\Omega(\theta) \left(\frac{d\sigma}{d\Omega}\right)_\theta e^{\delta^+(\Delta E') + \delta_B(\Delta E')}$$

Now the actual θ-p hodoscope plane sample area used in the data analysis was not shaped like R_s in Fig. 41 but instead like R_s in Fig. 27, where we do not have a constant $\Delta E'$. However, to treat this case we need only consider R_s in Fig. 27 as being made up of n little areas

like R_s in Fig. 41, each with its own $\Delta E'$, as shown in Fig. 42.

For the data taken with the 8-GeV/c spectrometer, the θ-p hodoscope plane was divided into 54 such strips with each strip spanning ± 0.144 milliradians of scattering angle. And for the 20-GeV/c spectrometer data, the θ-p plane was divided into 30 strips with each strip spanning ± 0.125 milliradians.

If for the nth strip, we call the mean angle, "θ_n" and the mean $\Delta E'$, "ΔE_n" - then the predicted number of counts in R_s of Fig. 42 is:

$$N_s^{\pm} = N_{in}^{\pm} \sum_{i=1}^{n} \left(\frac{d\sigma}{d\Omega}\right)_{\theta_i} \Delta\Omega(\theta_i)\, e^{\delta^{\pm}(\Delta E_i) + \delta_B(\Delta E_i)}$$

Therefore, under the same beam conditions,we would expect the difference due to radiative correction effects in the number of positron events to electron events collected to be characterized by the ratio:

$$\frac{N_s^+}{N_s^-} = \frac{\sum_{i=1}^{n} \left(\frac{d\sigma}{d\Omega}\right)_{\theta_i} \Delta\Omega(\theta_i)\, e^{\delta^{+}(\Delta E_i) + \delta_B(\Delta E_i)}}{\sum_{i=1}^{n} \left(\frac{d\sigma}{d\Omega}\right)_{\theta_i} \Delta\Omega(\theta_i)\, e^{\delta^{-}(\Delta E_i) + \delta_B(\Delta E_i)}}$$

In fact, this is precisely the ratio we have used to multiply the N/Q we get for electrons in order to compare it with the N/Q we get for positrons.

Specifically, the difference in the radiative correction between e^+ and e^- was accounted for by multiplying all electron N/Q's (and not positron N/Q's) by:

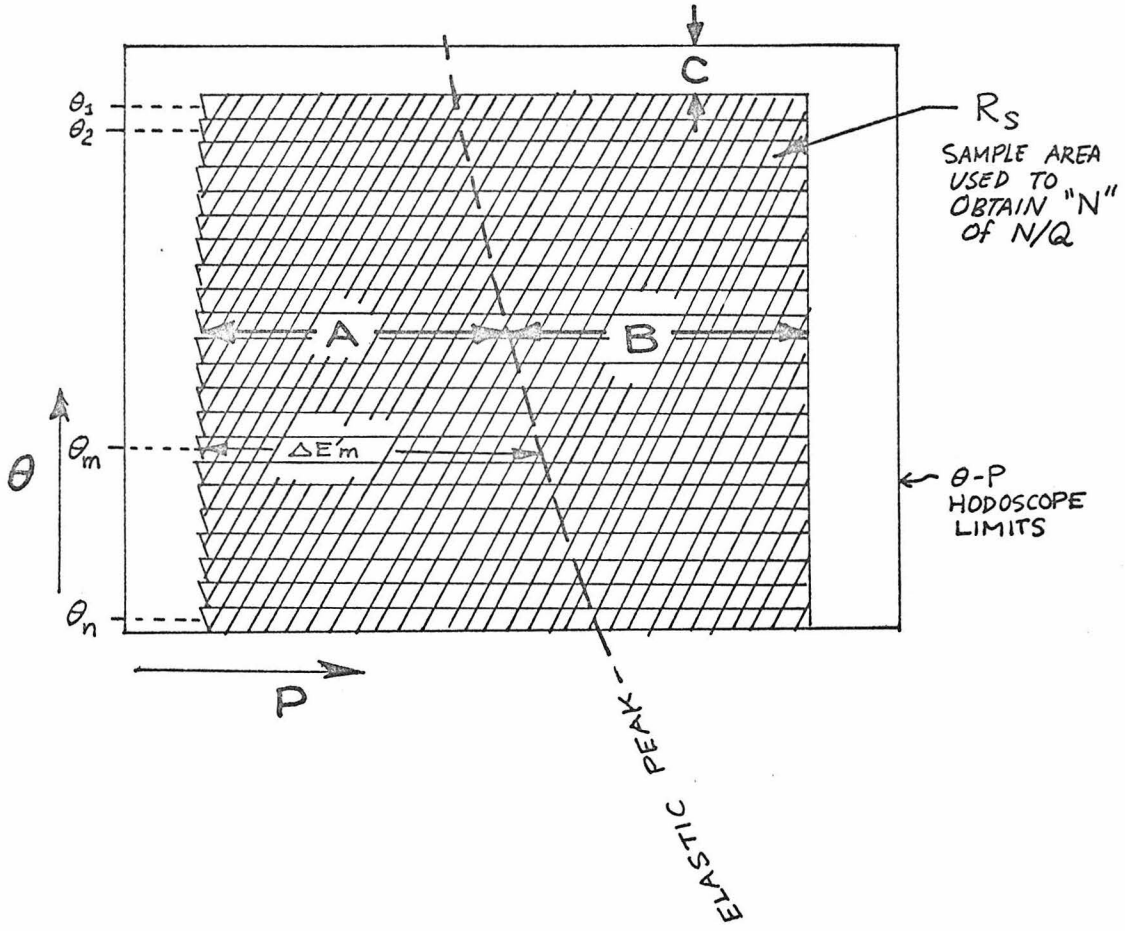

FIGURE 42: Standard sample area, R_s, in θ-p hodoscope plane approximated by n areas, each with a constant ΔE'

$$C_1 = \frac{\sum_{i=1}^{n} \left(\frac{d\sigma}{d\Omega}\right)_{\theta_i} \Delta\Omega(\theta_i)\, e^{\delta^+(\Delta E_i) + \delta_B(\Delta E_i)}}{\sum_{i=1}^{n} \left(\frac{d\sigma}{d\Omega}\right)_{\theta_i} \Delta\Omega(\theta_i)\, e^{\delta^-(\Delta E_i) + \delta_B(\Delta E_i)}}$$

Where $d\sigma/d\sigma$ is the Rosenbluth cross section given in Chapter I with the following dipole fit for the form factors:

$$G_M(q^2)/2.73 = G_E(q^2) = 1/(1+q^2/0.73)^2 \qquad q^2 \text{ in } (\text{GeV/c})^2$$

This empirical fit to the form factors fits elastic e^-p scattering data[13] to better than ±10% over the kinematic region of our experiment and will be completely adequate for estimating the angular weighting in the above sums.

And where:

$$\Delta\Omega(\theta_i) = \begin{cases} (59 - .047\nu^2)(1 - .04\delta_i^2) & \text{for 8-GeV/c system} \\ 1 & \text{for 20-GeV/c system} \end{cases}$$

The ν_i and δ_i are those corresponding to the position of the elastic peak on the ith strip

($\Delta\Omega(\theta_i)$ is really $\Delta\phi_i \Delta\theta_i$, but $\Delta\theta_i$ is the same for each i, so it cancels in C_1)

And $\delta^{\pm}(\Delta E_i)$ is given by the results of Meister and Yennie[14]:

$$\delta(\Delta E') = \delta_0(\Delta E') \pm \delta_1(\Delta E') + \delta_2(\Delta E')$$

where:

$$\delta_0(\Delta E') = \frac{\alpha}{\pi}\left\{\left[\ln\left(\frac{2P_0\cdot P'}{m^2}\right) - 1\right]\ln\left[\eta\left(\frac{\Delta E'}{E'}\right)^2\right] + \frac{13}{6}\ln\left(\frac{2P_0\cdot P'}{m^2}\right) - \frac{1}{2}\ln^2\eta - \frac{28}{9}\right\}$$

$$\delta_1(\Delta E') = -\frac{\alpha}{\pi}\left\{ \ln\eta \ln\left[\eta\left(\frac{E_o}{E_p}\right)^2\left(\frac{\Delta E'}{E'}\right)^4\right] - \beta(2E_o/M) + \beta(2E'/M)\right\}$$

$$\delta_2(\Delta E') = \frac{\alpha}{\pi}\left\{\left[\frac{E_p}{|\vec{P}_p|}\ln\left(\frac{E_p + |\vec{P}_p|}{M}\right) - 1\right] \times \ln\left[\frac{E_o^2}{ME_p}\left(\frac{\Delta E'}{E'}\right)^2\right] + \frac{3}{2}\ln\left(\frac{2E_p}{M}\right) - \frac{1}{2}\ln^2\left(\frac{E_p}{M}\right)\right\}$$

$P_o = (E_o, \vec{P}_o)$ = incident electron 4-momentum

$P' = (E', \vec{P}')$ = scattered electron 4-momentum

$P_p = (E_p, \vec{P}_p)$ = recoiling proton 4-momentum

$$\eta = E_o/E'$$

$$\beta(x) = \begin{cases} \ln^2 x & \text{if } x \le 1 \\ 0 & \text{if } x > 1 \end{cases}$$

α = 1/137

M = proton rest mass

m = electron rest mass

And the Bremsstrahlung radiative correction, δ_B, is obtained by integrating the Bethe Heitler formula (see Appendix C) to give:

$$\delta_B(\Delta E') = -\frac{4}{3}\left[\ell_A\left(\ln\left(\frac{E'}{\Delta E'}\right) - .625\right) + \ell_B\left(\ln\left(\frac{E'^2}{E_o \Delta E'}\right) - .625\right)\right]$$

where: ℓ_B = amount of material in radiation lengths the electron passes through before scattering

ℓ_A = amount of material in radiation lengths the electron passes through after scattering, but before detection in the hodoscope.

The sizes of the radiative correction factors, C_1, are shown in Table II.

E_o GeV	θ (o)	C_1 (%)	CS/TH	C_2 (%)	CS/EO	C_3 (%)	C_4 (%)	C_5 (%)	C_6 (%)	C_7 (%)	C_8 (%)	C_9 (%)	C_{10} (%)	C_{11} (%)
4	12.5	0.635	-6.91	0.2	-4.99	0.4	5	0.3	0.3	0.03	10	0.3	-1	0.3
4	20.0	1.523	-7.81	0.05	-6.21	0.4	5	0.3	0.2	0.03	1	0.0	-1	0.3
4	27.5	2.660	-7.79	0.2	-6.65	0.4	5	0.2	0.2	0.05	2	0.2	-3	0.2
4	35.0	4.081	-7.37	0.1	-6.72	0.4	6	0.0	0.1	0.03	3	0.6	-3	0.1
10	2.6	0.060	-5.28	0.2	-3.28	0.3	7	0.8	0.0	0.0	13	0.8	-1	-0.5
10	5.0	0.222	-7.11	0.0	-5.14	0.1	6	3.0	0.0	0.0	2	30	-6	-0.4
10	12.5	1.355	-9.04	0.2	-7.54	0.05	6	0.2	0.1	0.02	1	0.0	-2	0.2
10	15.0	1.954	-8.95	0.05	-7.68	0.02	6	0.3	0.1	0.1	1	0.0	-2	0.2

TABLE II.

Typical Sizes of the Correction Factors Applied to N/Q

$CS/TH=(\theta/\frac{d\sigma}{d\Omega})\,d\left(\frac{d\sigma}{d\Omega}\right)/d\theta$, $CS/EO=(E_o/\frac{d\sigma}{d\Omega})\,d\left(\frac{d\sigma}{d\Omega}\right)/dE_o$

C_1=Rad. Corr., C_2= θ Corr., C_3=E_o Corr., C_4=Ambig. Events,
C_5=Trigger Inefficiency, C_6=Toroid Drift, C_7=Solid Angle,
C_8=Electronic Dead Time, C_9=Computer Sampling Loss,
C_{10}=Background, C_{11}=Earth Field Corr.

2. Deviations in Spectrometer Angle, C_2

Because the angular position of the spectrometer varied slightly between different runs of the same data point, it was necessary to normalize all measurements of N/Q to a common angle θ_o.

The spectrometer angle was given by a gear driven encoder. The gear rode along a rack which was attached to the end station floor, and gave the spectrometer angle, θ, to ±.001 degrees.

Since $|\theta-\theta_o|/\theta_o << 1$, the $N(\theta)/Q$'s were linearly extrapolated to $N(\theta_o)/Q$ using $CS/TH=\left(\theta/\frac{d\sigma}{d\Omega}\right)\frac{d(d\sigma/d\Omega)}{d\theta}$, calculated from the Rosenbluth formula using the dipole fit. Thus:

$$C_2 = 1 + \frac{(\theta_o-\theta)}{\theta_o} CS/TH$$

The CS/TH's used and the typical size of the C_2 corrections are shown in Table II.

3. Deviations in Incident Energy, C_3

Because of drifts in the regulation of the current supplying the switchyard energy defining magnets, the incident energy varied between different runs of the same point. As was mentioned earlier (cf. Section C of Chapter II) these energy drifts were monitored by periodically measuring the field in a switchyard reference magnet with a flip coil, and using a calibration curve to give the incident energy E_o.

We took this value for the mean incident energy in the particular run and normalized the N/Q's obtained to a standard energy E_{oo}. Again, since $|E_o-E_{oo}|/E_{oo}<<1$, the $N(E_o)/Q$'s were linearly extrapolated to $N(E_{oo})/Q$ using $CS/EO=\left(E_o/\frac{d\sigma}{d\Omega}\right)\frac{d(d\sigma/d\Omega)}{dE_o}$, calculated from the Rosenbluth formula using the dipole fit. Thus:

$$C_3 = 1 + \frac{(E_{oo}-E_o)}{E_{oo}} CS/EO$$

The CS/EO's used and some typical C_3's are shown in Table II.

4. Ambiguous Events, C_4

Our discussion of N/Q has been based on the events in the θ-p hodoscope plane. However, only a select class of events appear in the θ-p hodoscope plane used to obtain N/Q. The computer selects only those events which can be assigned a p-hodoscope bin and a θ-hodoscope bin. Thus events which cause double, triple, etc. tracks in either the θ and p hodoscopes do not appear in our θ-p plane and therefore are not included in N/Q. C_4 represents the correction to N/Q for these lost events.

a. NGOOD

Let us first define the following codes to denote the kinds of events that may occur in each hodoscope:

Code 0	2 adjacent counters fire	(symbolically --00----)
Code 1	3 adjacent counters fire	(" ----000-----)
Code 2	4 adjacent counters fire	(" ---0000-----)
Code 3	1 counter fires	(" -----0------)
Code 4	no counter fires	(" ----------)
Code 5	multiple singles (≤5)	(" --0--0---0--)
Code 6*	double, triple, etc. tracks	(" --00--000---)
Code 7	profuse singles (>5)	(" -0--0-0-0-0-0)

* Anything not falling into codes 0 to 5, 7 to 9, are placed here. However, almost all code 6's are due to double tracks.

Code 8 edge counter fires only (symbolically: ---------0)

Code 9 2 or more adjacent counters (" --0-0--00----)
plus 1 or 2 single counters

In this notation, only events whose θ and p codes are a combination of 0, 1, 2, 3 and 9 are used to make up N/Q. The computer was able to assign a specific θ and p bin only to events of this kind.

The reasons for accepting events with these codes are given below (while examining the reasons, it is helpful to look at Table III which gives the typical size of these contributions):

Code 0 Events: Code 0 events are the normal type of event in the θ-hodoscope of the 8-GeV/c spectrometer (see Fig. 43). Code 0 and Code 1 events are the normal type of event in the p-hodoscopes in the 8-GeV/c and 20-GeV/c spectrometers (see Fig. 44).

In the θ-hodoscope for the 20-GeV/c spectrometer, the geometry is such that a "normal" event causes three adjacent counters to fire (see Fig. 45). However,an inefficient counter could make such an event appear as a code 0 event. Thus we also accept code 0 events in the 20-GeV/c θ-hodoscope providing they have satisfied the trigger and pulse height conditions.

Code 1 Events: As mentioned above, code 1 events are normal events in the θ-hodoscope in the 20-GeV/c spectrometer and in the p-hodoscopes in the 8-GeV/c and 20-GeV/c hodoscopes. The geometry of the counters also allows the occasional firing of three adjacent counters in the θ-hodoscope in the 8-GeV/c spectrometer as well (cf. dotted line in Fig. 43). A normal event accompanied by some

θ-code \ p-code	0	1	2	3	4	5	6	7	8	9
0	6465	2641	331	648	2	158	217	10	1	819
1	164	66	9	16	1	4	38	0	0	59
2	23	7	1	2	0	3	17	0	0	5
3	624	281	48	101	1	19	17	0	1	93
4	12	4	0	2	0	2	0	0	0	2
5	28	10	1	3	1	3	3	0	0	8
6	37	23	4	3	0	4	21	0	0	25
7	0	0	0	0	0	0	0	0	0	0
8	136	40	3	16	1	3	6	0	0	12
9	299	113	14	30	0	10	20	0	0	54

TABLE III.

Typical distribution of events in the 8-GeV/c θ-p code plane when the trigger counters are required to fire. (Typical distribution from Run 2168, E_o=4 Gev, θ=12.5°.)

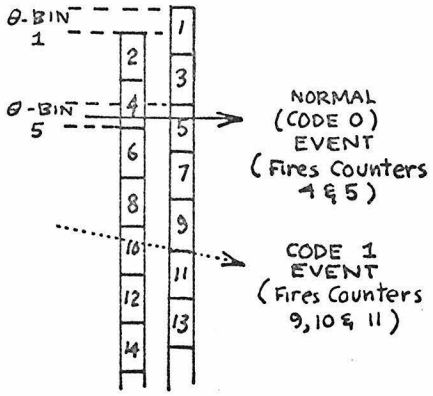

FIGURE 43:
θ-hodoscope in
8-GeV/c system

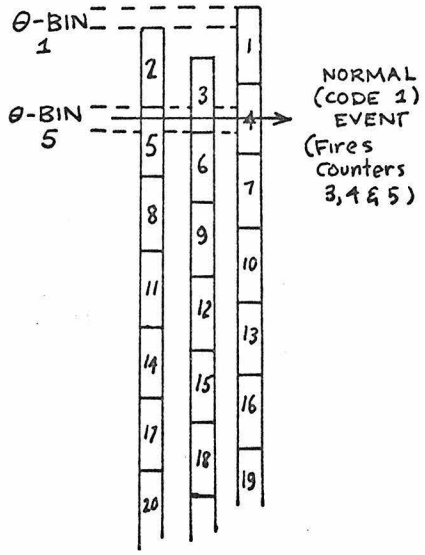

FIGURE 45:
θ-hodoscope in
20-GeV/c system

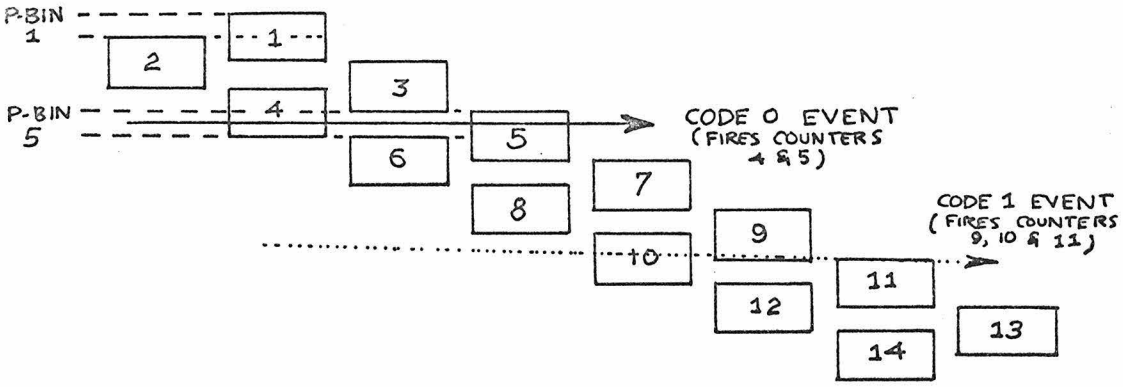

FIGURE 44:
p-hodoscope in
both 8-GeV/c and
20-GeV/c system

low energy background might also appear as a code 1 event.

Code 2 Events: These can occur for the same reasons described for code 1 events.

Code 3 Events: These are included in the belief they are really code 0 events involving an inefficient counter. Because at least two counters were known to be inoperative during the experiment, the number of such events is considerable.

However, low energy background will often cause only one counter to fire, so it is necessary to justify our inclusion of code 3 events. It turns out that if we look at the θ-p plane distribution of only code 3 events, the events are distributed, both in shape and position, in the manner they would if they were elastic - providing we require the trigger and pulse height conditions to be met. This is shown in Fig. 46, which shows the p-distribution (obtained by sliding the events in the θ-p hodoscope plane to a common angle) of code 3 events compared with the p-distribution of code 0 events. Code 3 events that do not satisfy the trigger requirements are also shown. Note that such events do not appear as elastic events.

Code 9 Events: These events are assumed to be a combination of a good event (code 0, 1 or 2) and some low energy background. A study of code 9 distributions confirmed this.

The actual bin assignments (cf. Figs.43, 44, 45) were made as follows. Where the events represent an odd number of adjacent bins,

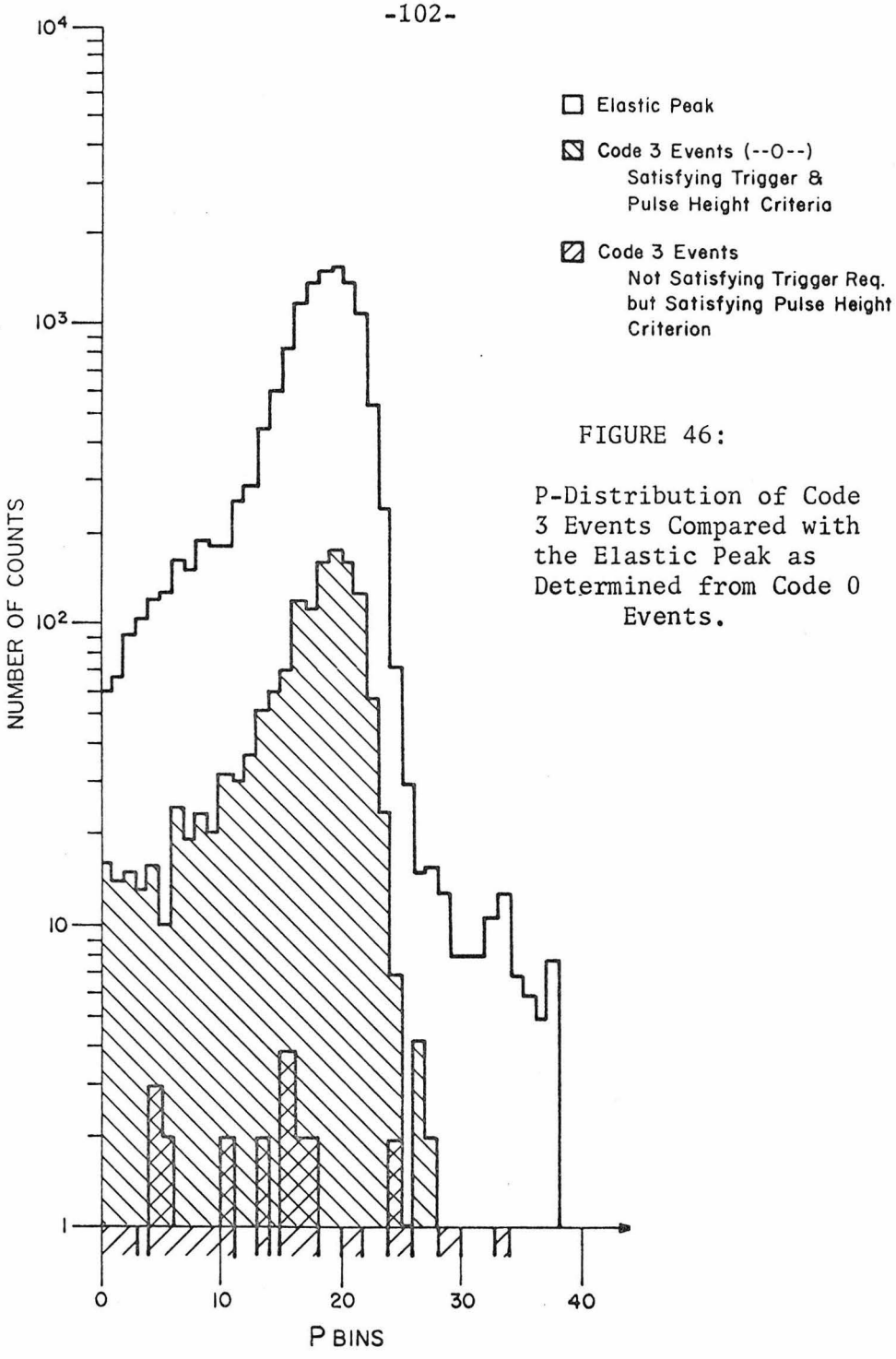

FIGURE 46:

P-Distribution of Code 3 Events Compared with the Elastic Peak as Determined from Code 0 Events.

such as in code 0 and 2 events, the central bin was assigned to the group. In code 1 and 3 events, there are two adjacent bins involved, and alternate bins were assigned (e.g., left bin, then right bin, etc.) to these groups. The exception to this form of bin assignment was the 20-GeV/c θ-hodoscope, where a normal event causes three adjacent counters to fire. There, a unique bin was assigned to code 1 and 3 events and an alternating procedure applied to code 0 and 2 events.

Let us denote the total number of events of the kind just described (code 0, 1, 2, 3 and 9 in both θ and p hodoscopes) as NGOOD. Then if we define $N(\theta_c,p_c)$ as the total number of events with θ event code = θ_c and p event code = p_c, we get:

$$\text{NGOOD} = \sum_{i=0}^{3}\sum_{j=0}^{3} N(i,j) + \sum_{i=0}^{3}\left[(N(i,9) + N(9,i))\right] + N(9,9)$$

b. NAMBIG

However, there are other events which may be elastic but which are not included in NGOOD and which do not appear in N/Q. These are events in which a multiple track (code 5 or code 6) has occurred in one or more of the hodoscopes.

That such events are indeed good events can be seen if we make the following code assignments to convert our multiple track events to a number of single track events.

```
θ ----000-----                    θ ----000-----
                                  p --00--------
                  treat as
p --00---00---                    θ ----000-----
                                  p -------00---

                                  θ --00--------
θ --00--00----                    p --------00--
                  treat as
p ---00---00--                    θ ------00----
                                  p ---00-------
```

and similarly:

```
                                  θ ----000-----
θ ----000-----                    p ---0--------
                  treat as
p ---0-----0--                    θ ----000-----
                                  p ---------0--
```

Since some of the multiple tracks will be due to background, this type of assignment produces more good events than actually occur, but this will not affect our argument. For if we examine the p-distribution for such reassigned events, we get the result shown in Fig. 47. The similarity of the peaks verifies our assumption that such events are predominantly elastic events.

Ambiguous events are all events with θ-code and p-code any combination of 5 and 6 with 0,1,2,3,5,6, and 9. Thus the total number of such events, which we will call "NAMBIG", is:

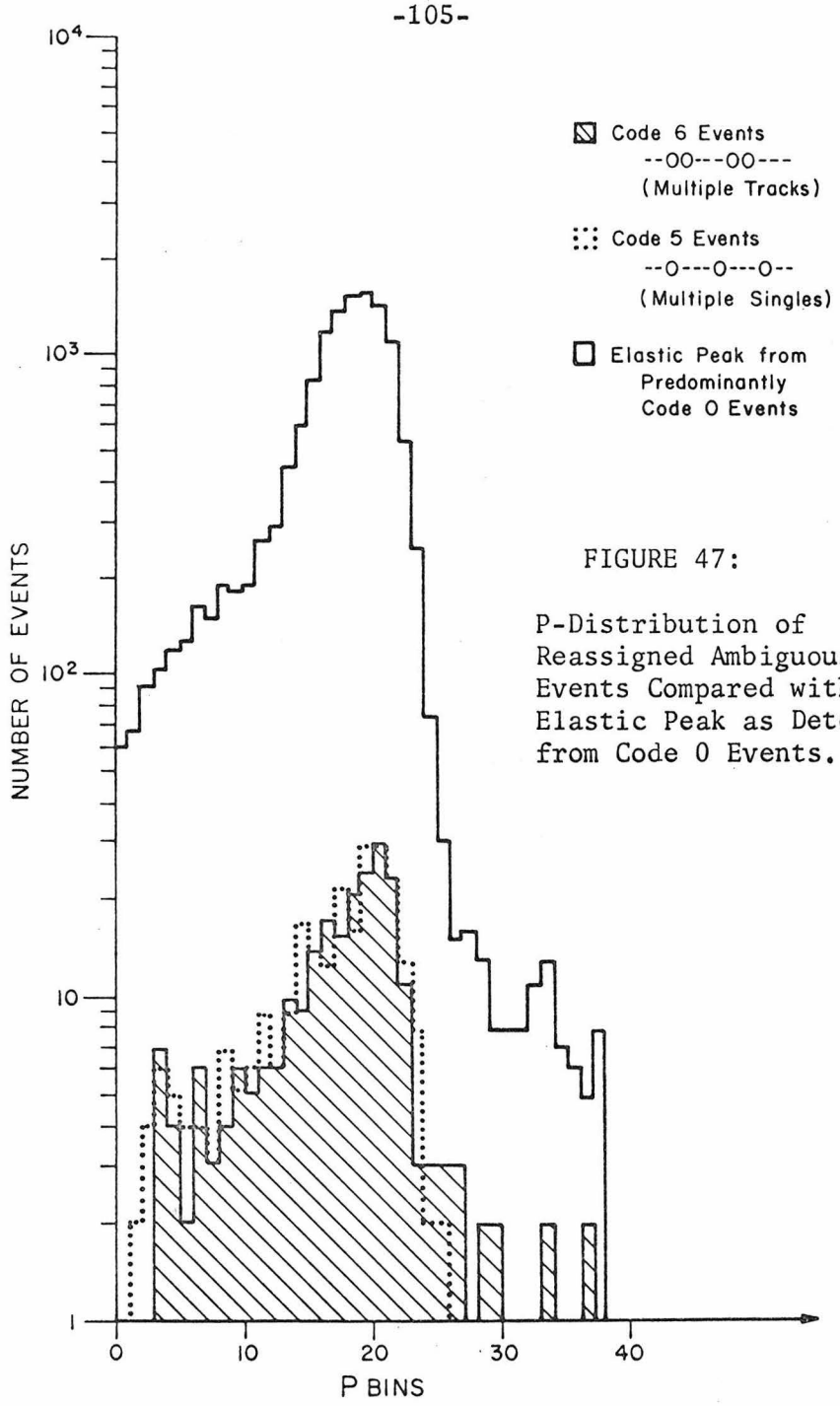

FIGURE 47:

P-Distribution of Reassigned Ambiguous Events Compared with Elastic Peak as Determined from Code 0 Events.

$$\text{NAMBIG} = \sum_{i=0}^{3}\Big[N(5,i) + N(6,i) + N(i,5) + N(i,6)\Big] + N(5,9) + N(9,5) + N(6,9) + N(9,6) + N(5,5) + N(5,6) + N(6,5) + N(6,6)$$

c. C_4

Therefore to compensate for these ambiguous events which are not included in N/Q, we multiply up N/Q by:

$$C_4 = \frac{\text{NGOOD} + \text{NAMBIG}}{\text{NGOOD}}$$

Note that this treats ambiguous events as single events (instead of two events together). This simplifies our correction for electronic dead-time (to be described in Section E8 of this chapter), which compensates for the event losses due to the occurence of more than one event per pulse. Furthermore, by applying the correction in this manner, we guard against the possibility that one of the tracks is a result of low energy background.

Some typical C_4's are shown in Table II.

5. Trigger Inefficiency, C_5

In the data analysis, only those events which fired both front and rear triggers in the 8-GeV/c hodoscope or all three trigger counters in the 20-GeV/c hodoscope were considered. However, because of the finite recovery time of the phototubes, the "good" event detection efficiency of the trigger counters was less than 100%. To correct for this inefficiency, the N/Q's were multiplied by C_5, where:

$$C_5 = \frac{CC1Y + CC1N}{CC1Y}$$

Where:

$$CC1Y = \begin{cases} \text{all } (0,0)^* \text{ events } \underline{\text{with}} \text{ a good trigger for the 8-GeV/c } \underline{\text{system}} \\ \text{all } (0,0),(0,1),(0,2),(1,0),(2,0) \text{ events } \underline{\text{with}} \text{ a good trigger for the } \underline{\text{20-GeV/c}} \text{ system} \end{cases}$$

and:

$$CC1N = \begin{cases} \text{all } (0,0) \text{ events } \underline{\text{without}} \text{ a good trigger for the } \underline{\text{8-GeV/c}} \text{ system} \\ \text{all } (0,0),(0,1),(0,2),(1,0),(2,0) \text{ events } \underline{\text{without}} \text{ a good trigger for the } \underline{\text{20-GeV/c}} \text{ system} \end{cases}$$

The definitions of CC1Y and CC1N are different for the 8 and 20-GeV/c systems because code 1 events are normal events in the 20-GeV/c θ-hodoscope.

---

* (θ_c, p_c) = (θ-code, p-code)

C_5 is based on the assumption that CC1N represents good events that were missed because of an inefficient trigger counter. A p-distribution plot of just CC1N events (obtained by sliding events in the θ-p plane to a common angle) is shown in Fig. 48a, and is consistent with such events being elastic events. Fig. 48b shows that the TA pulse height spectrum of such events also corresponds to that obtained for elastically scattered electrons. Therefore the bad events included in CC1N are few, and since C_5 is a small correction ($\sim$0.5%), the few bad events will affect N/Q negligibly.

The following question may be raised - why do we not take CC1Y = NGOOD with a good trigger, and CC1N = NGOOD without a good trigger? The reason is that, whereas code 3 events (1 counter fires) and code 5 events (multiple singles) appear to be good elastic events when a trigger is required, the same is <u>not</u> true when we do not enforce the trigger requirement. This is evident in Fig. 46. This can also be seen when one looks at the ratio:

$$\frac{N_3}{N(0,0)} = \frac{\sum_{i=0}^{3}(N(3,i)+N(i,3)) - N(3,3)}{N(0,0)}$$

For a typical run: (Run 2168, E_0=4 GeV, θ=12.5°)

$N_3/N(0,0)$ = 0.295 with a good trigger

$N_3/N(0,0)$ = 1.59 without a good trigger

The fact that the ratio is larger without a good trigger than with a

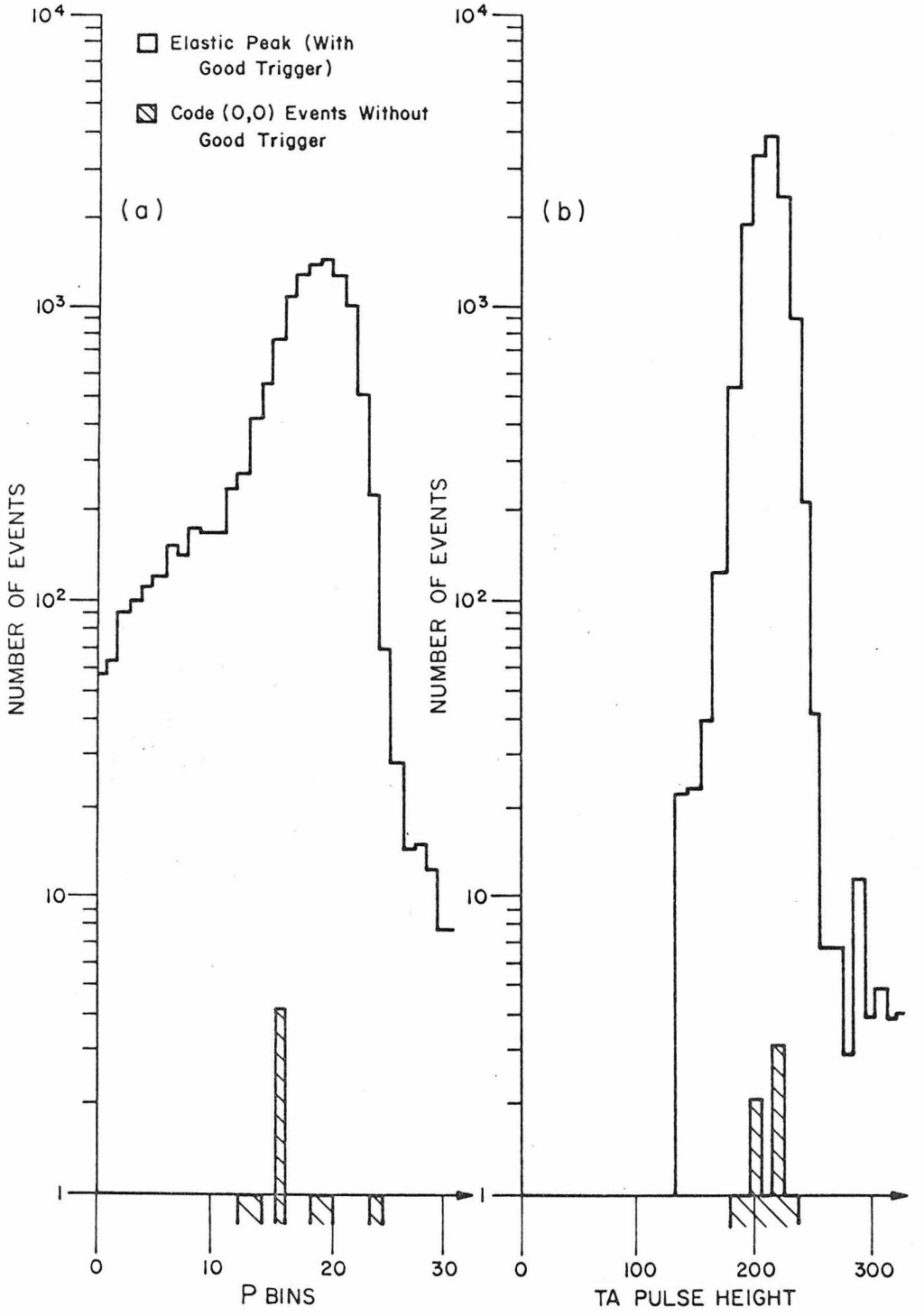

(a)
P-Distribution of (0,0) Events with No Trigger

(b)
TA Pulse Height Spectra of (0,0) Events with No Trigger

FIGURE 48.

good trigger indicates inelastic events are contributing significantly to code 3 events without a trigger. Therefore we cannot use NGOOD to correct the trigger inefficiency. In addition, the majority of NGOOD events are already contained in (0,0), so the gain in statistical accuracy by using NGOOD instead of (0,0) is slight.

Some typical C_5's are shown in Table II.

6. Toroid Drift Correction, C_6

As we mentioned earlier (cf. Section E1, Chapter II) there were drift currents in the electronics of the toroid charge integrator. Since Q of N/Q was taken from the toroid beam charge monitor for most of the data (except the 2.6° and 5.0° data, where the corrected Faraday cup was used), it was necessary to correct N/Q for these drifts.

The mean toroid drift currents (I_{drift}) measured, are shown in Table IV. The drift currents are given in the chronological sequence of beams used.

To correct for this drift, the following correction was applied to N/Q for runs other than those of the 2.6° and 5.0° data (for these, C_6 below equalled 1):

$$C_6 = \frac{Q_{tor}}{Q_{tor} - t \cdot I_{drift}}$$

Where:

I_{drift} = average drift current during the particular beam

t = total toroid integrating time for the particular run

Q_{tor} = total integrated toroid charge for the run

Some typical C_6's are shown in Table II.

Incident Energy E_o (GeV)	Particle	Toroid Drift Current I_{drift} (nanoAmps)
4	e^+	0.03±.03
4	e^-	0.05±.05
4	e^+	0.00±.03
10	e^+	0.00±.03
10	e^-	0.04±.03
10	e^+	0.03±.03
10	e^-	0.05±.03
10	e^+	-0.025±.03
4	e^+	0.03±.04
4	e^-	0.02±.02
4	e^+	0.07±.03
4	e^-	0.01±.02
4	e^+	0.05±.03
10	e^+	0.04±.02
10	e^-	-0.11±.02
10	e^+	0.04±.06
10	e^-	0.05±.02

TABLE IV.

Toroid Drift Currents
Listed in the Chronological
Beam Order

7. Solid Angle Acceptance Variation, C_7

As we mentioned earlier (Section C of this chapter), the position of the elastic peak in the θ-p hodoscope plane varied between runs of a given data point. Because the solid angle acceptance is not the same for all regions of the θ-p plane, the correction for this effect must be considered.

For the 8-GeV/c spectrometer, we use the φ-acceptance function described earlier:

$$\Delta\phi(\theta,p) = (59 - 0.47\vartheta(\theta)^2)(1 - 0.04\delta(p)^2)$$

The relative solid angle seen by an elastic peak p=p(θ) is:

$$\Delta\Omega \cong \int d\theta\,\Delta\phi = \int d\theta\,(59 - 0.47\vartheta(\theta)^2)(1 - 0.04\,\delta(p(\theta))^2)$$

Since the elastic peak movements are small we are less concerned with ΔΩ than dΔΩ/dp. It is shown in Appendix D that for the data points in this experiment, where the elastic peak is essentially a straight line in the θ-p plane, we can write:

$$\frac{d\Delta\Omega}{dp} = \left(\int d\theta\,(59 - 0.47\vartheta(\theta)^2)\right) \cdot \left[\frac{d(1 - 0.04\delta^2(p))}{dp}\right]_{p=p_e}$$

Where: p_e = momentum at the center of the elastic peak in the θ-p plane

Since the kind of correction we would apply to ΔΩ would be of the form:

$$\frac{d\Delta\Omega}{dp}\,\Delta p$$

and since the $\int d\theta\,(59 - 0.47\vartheta^2)$ factor cancels when we take ratios, we will compensate for the solid angle changes equally well if we simply

multiply N/Q by:

$$C_7 = 1/(1-0.04\delta(p_e)^2)$$

Where: p_e corresponds to the average momentum of the elastic peak in the R sample area in the θ-p plane

In the 20-GeV/c spectrometer case, the use of ϕ slits at the entrance to the spectrometer resulted in a ϕ-acceptance that varied negligibly with p. Hence:

$$\Delta\Omega = C\int d\theta \Delta\phi(\theta) = \text{Constant}$$

and $C_7 = 1$ for the 20-GeV/c system

Some typical C_7's are shown in Table II.

8. Electronic Dead Time, C_8

As we mentioned earlier (Section F1d, Chapter II), an electronic toggle was used in the experiment to limit the data rate to a maximum of one event per beam pulse. The event loss due to multiple events per beam pulse was significant, especially in the high rate data. However, the beam intensity was adjusted so that these losses were always less than 20%.

To correct for these lost events, N/Q was multiplied by the ratio of the number of pulses into the "set" input of the toggle, over the number of pulses at the output of the toggle. This ratio was taken from two fast scalers, which are labelled EVTT and NRD in Fig. 21 and Fig. 25.

Thus if we call:

EVTT = number of pulses into the toggle

NRD = number of pulses out of the toggle

then C_8 is:

$$C_8 = \frac{\text{EVTT}}{\text{NRD}}$$

There still remains the question of deadtime in the EVTT scaler. If we assume the events are distributed timewise in a Poisson distribution, then the fractional error in EVTT due to deadtime losses is shown in Appendix E to be:

$$\varepsilon = \frac{EVTT_{actual} - EVTT}{EVTT} = \frac{EVTT}{2N_p T_\ell / \tau}$$

Where: N_p = Total number of beam pulses

T_ℓ = Beam pulse width in nsec

τ = Dead time of the scaler in nsec

For a typical high rate run, say Run 2168, which is an e^+ run with E_o=4 GeV, θ=12.5°:

$$EVTT = 17785$$
$$N_p = 133725$$
$$T_\ell = 1600 \text{ nsec}$$

this gives $\varepsilon = 0.00416 \times 10^{-2} \tau$

Since the scalers used were 100 GHz scalers, the deadtime was of the order of 10 nsec. Thus the error due to the deadtime in the EVTT scaler is ∿0.05%, which is negligible.

We can use the same type of deadtime calculation to estimate C_8. It is shown in Appendix E that, providing each beam pulse is equivalent in intensity:

$$C_8 \cong CC_8 = 1 + \frac{NRD}{2N_p}$$

However, in the experiment the intensity per beam pulse varied appreciably so that CC_8 provides at most a rough check of C_8. Typical CC_8's are compared with C_8's in Appendix E.

Some typical C_8's are shown in Table II.

9. Computer Sampling Losses, C_9

Because of magnetic tape errors incurred during data logging, not all events logged by the computer (NRD) could be analyzed. Since N/Q includes only events that can be analyzed, it was necessary to compensate for those lost by multiplying N/Q by:

$$C_9 = \frac{NRD}{N_{spl}}$$

Where:

NRD = events logged by the computer

N_{spl} = events analyzed

Some typical C_9's are shown in Table II. This correction is large only for the 5^o data, where the data tapes had many errors because of a faulty recorder.

10. Background Subtraction, C_{10} -

The background subtraction was performed in the following manner. A region R_{fb} (see Fig. 49) in the kinematically forbidden region of the θ-p plane was used as a background sample. The counts in R_{fb}, $N(R_{fb})$, were then expanded by solid angle factors to match the solid angle of region R_s, the region in which N/Q was determined. Since empty target studies indicate the background population in the lower left hand corner (see Fig. 49) is greater than the number of counts in the upper right corner (even though the solid angle acceptance is the same), the expanded counts are multiplied by a compensating factor 1.3, so that the estimated background counts in the N/Q sample region R_s are:

$$N_{BG}(R_s) = \frac{1.3\, N(R_{fb}) \iint_{R_s} dp\, d\theta\, \Delta\phi(\theta,p)}{\iint_{R_{fb}} dp\, d\theta\, \Delta\phi(\theta,p)}$$

If we use the acceptance function (discussed earlier in Section F1a, Chapter II):

Then:
$$N_{BG}(R_s) = \frac{1.3\,(A+B)\left[1 - \frac{(A+B)^2}{3\times10^4}\right]\left(\frac{54-C}{54}\right)}{\omega\left[1 - 4\times10^{-4}\left(400 - 20\omega + \omega^2/3\right)\right]}$$

A, B, C, ω are defined in Fig. 49

By using a typical background sample area R_{fb} in an empty target run, this expression reproduced the total number of events in the θ-p plane reasonably well.

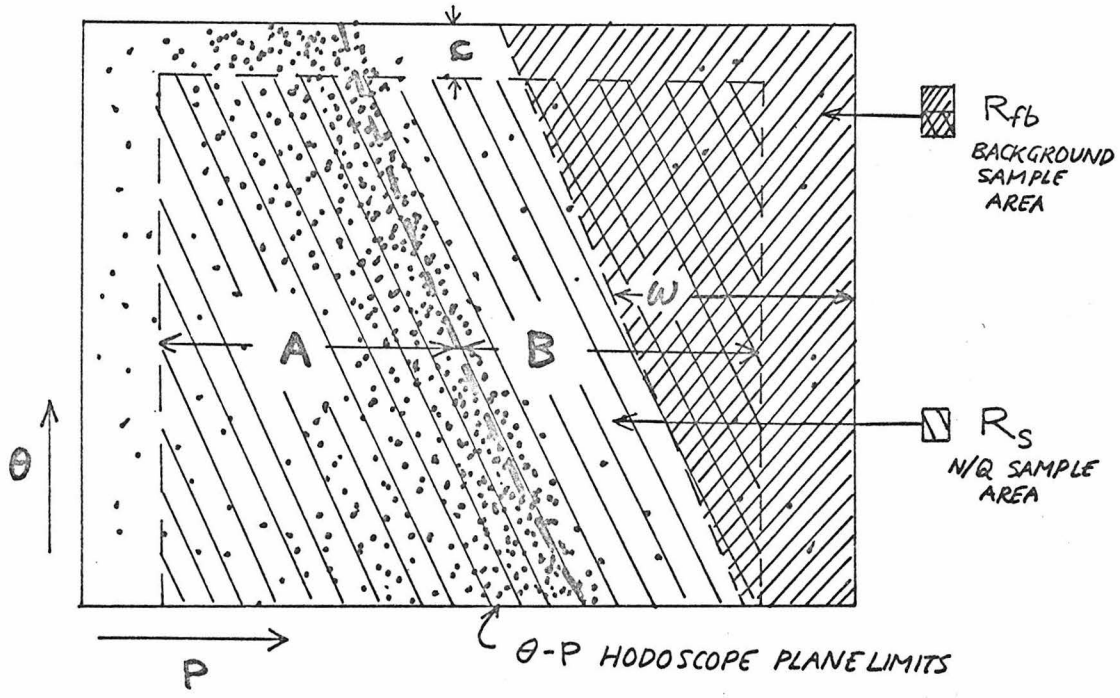

FIGURE 49: Diagram showing Background Sample area, R_{fb}, in relation to R_s, in the θ-p hodoscope plane.

Therefore, C_{10} was the following:

$$C_{10} = \frac{N(R_s) - N_{BG}(R_s)}{N(R_s)}$$

Where:
$N(R_s)$ = number of events in the region R_s, used to make up N of N/Q

The background subtraction affected the N/Q's slightly (∿2% for most of the data) and had a negligible effect on the values of R. Typical C_{10}'s are shown in Table II.

11. Steering Correction Due to Earth's Magnetic Field, C_{11}

We mentioned earlier (Section C, Chapter II) that the incident beam line was slightly curved because of the earth's magnetic field. Since the curvature will be in the opposite direction for electrons and positrons, there will be a relative shift in the e^- and e^+ scattering angles.

The shift in angle was calculated using the following argument. Looking at Fig. 50, if the beam was incident on TC20 as shown by the dotted path, the angular deflection would be:

$$\Delta\theta' = \int_{\ell} q \frac{\vec{B}\cdot\vec{n}}{P}\, d\ell$$

B = field along path
n = normal to the plane
q = $\pm e$
p = incident electron momentum

However, the beam was actually centered on TC20 and RS2, so that the actual beam path was more like the solid one in Fig. 50, which is obtained from the dotted path by a rotation about TC20 by the amount:

$$\vartheta \simeq \frac{y}{\int_{\ell} d\ell} = \frac{r[1-\cos(\Delta\theta')]}{\int_{\ell} d\ell} = \frac{1-\cos(\Delta\theta')}{\Delta\theta'} \simeq \frac{\Delta\theta'}{2}$$

Therefore the actual error in the scattering angle, $\Delta\theta$, is:

$$\Delta\theta = \Delta\theta' - \Delta\vartheta \simeq \Delta\theta' - \Delta\theta'/2 = \Delta\theta'/2$$

and thus the relative shift in angle from e^+ to e^- is:

$$\Delta\theta_{\pm} = 2\Delta\theta = \frac{q}{P}\int_{\ell} \vec{B}\cdot\vec{n}\, d\ell$$

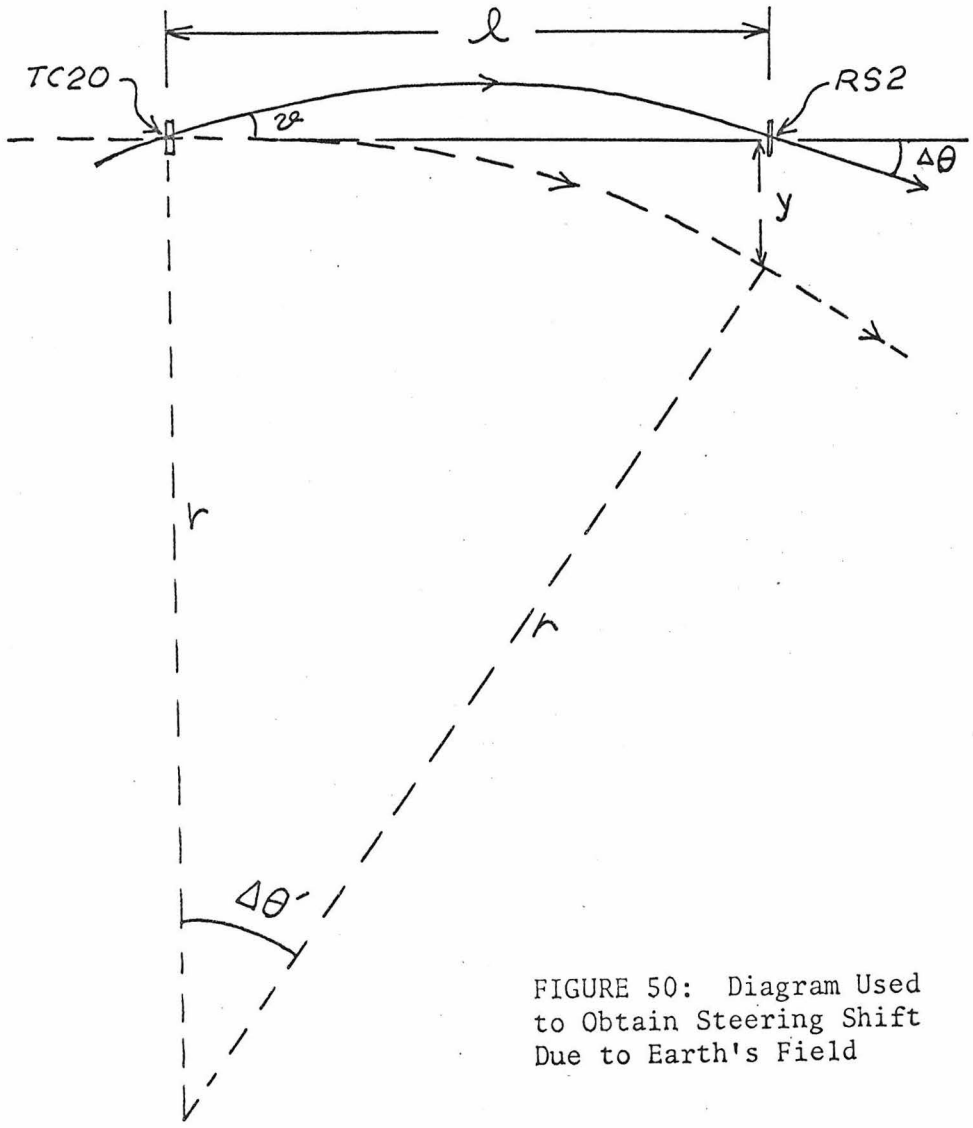

FIGURE 50: Diagram Used to Obtain Steering Shift Due to Earth's Field

The integral was calculated from field measurements taken along the beam line (see Fig. 51) and found to be equal to 1.64×10^{-3} Webers/meter.

Therefore, for E_o=4 GeV, the relative e^+ to e^- angular shift was:

$$\Delta\theta_{\pm} = 0.123 \text{ mrad}$$

and for E_o=10 GeV, the relative e^+ to e^- angular shift was:

$$\Delta\theta_{\pm} = 0.0492 \text{ mrad}$$

To compensate for these shifts, the electron N/Q's were increased by the amounts shown in Table V. The correction is in the opposite direction for the θ=2.6° and 5.0° data because the 20-GeV/c spectrometer was on the opposite side of the beam line to the 8-GeV/c spectrometer.

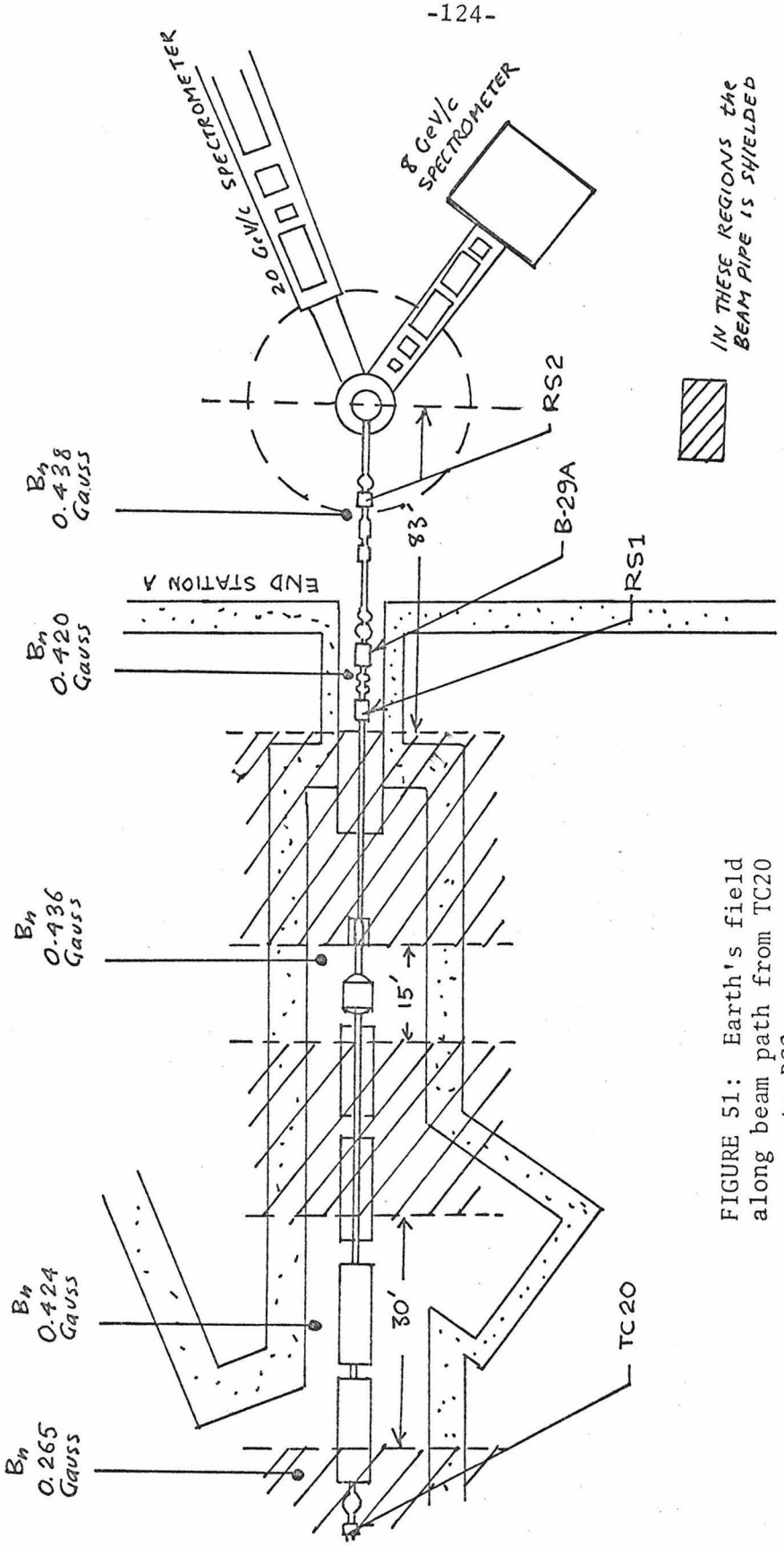

FIGURE 51: Earth's field along beam path from TC20 to RS2

INCIDENT ENERGY E_0 (GeV)	Scattering Angle θ (degrees)	Correction to R for Earth's field steering shift (%)
4	12.5	+0.389
4	20.0	+0.285
4	27.5	+0.200
4	35.0	+0.148
10	2.6	-0.570
10	5.0	-0.400
10	12.5	+0.203
10	15.0	+0.167

TABLE V.

Corrections to R for steering shift due to Earth's magnetic field.

F. Obtaining R From the N/Q's

The corrected N/Q's of a given data point were averaged in the following manner:

$$\langle N/Q \rangle^{\pm} = \frac{\sum_i N_i^{\pm} (N/Q)_i^{\pm}}{\sum_i N_i^{\pm}}$$

Where:

+ denotes positrons
- denotes electrons
$(N/Q)_i$ = N/Q for the ith run
N_i = N of N/Q for the ith run

R is obtained from the ratio of $\langle N/Q \rangle^+$ and $\langle N/Q \rangle^-$, i.e.,

$$R = \frac{\langle N/Q \rangle^+}{\langle N/Q \rangle^-}$$

The method described above was chosen for the averaging, rather than the more conventional method of averaging using:

$$\langle N/Q \rangle = \frac{\sum_i (N/Q)_i / \varepsilon_i^2}{\sum_i 1/\varepsilon_i^2}$$

Where ε_i is the fractional error in $(N/Q)_i$

because it was felt that large systematic errors like the monitor uncertainty do not reflect the relative accuracy of the various N/Q's making up $\langle N/Q \rangle$. For this reason, the runs were weighted with the inverse of the fractional statistical error squared, $(1/\sqrt{N_i})^{-2}$.

G. Errors

The uncertainty attached to N/Q was a combination of the following:

1. Statistical Fluctuation in N of N/Q, ϵ_1

This varied from ±0.5% to ±10%.

2. Statistical Fluctuation Arising from the Background Sample, ϵ_2

This varied from ±0.1% to ±2.5%.

3. Statistical Fluctuation Arising from Other Corrections, ϵ_3

The statistical uncertainty in the corrections for ambiguous events, C_4; trigger inefficiency, C_5; electronic deadtime, C_8; and computer losses, C_9, were of the order ±0.2%.

4. Uncertainty in the Elastic Peak Position, ϵ_4

The uncertainty in determining the exact location of the elastic peak resulted in an uncertainty in the radiative correction and solid angle. This uncertainty was of the order of ±0.1%.

5. Uncertainty in Beam Steering, ϵ_5

Using the zinc sulfide screen arrangement mentioned earlier (Section C, Chapter II), the beam steering was maintained to ± 1 mm. on the zinc sulfide screens.

If we consider the effect of a ±1 mm uncertainty in the horizontal position of the beam, we find 1st order beam optics predict zero shift at the hodoscopes and 2nd order optics predict a negligible

shift.

The positional uncertainty of ±1 mm corresponds to an angular uncertainty of ±0.02 mrad. This angular uncertainty produces an uncertainty in N of N/Q (because of the variation of cross section with angle) by the amounts shown in column 3 of Table VI. This is consistent with steering tests in which the beam was deliberately misteered (in angle) by ±0.1 mrad, the results of which are shown in Figure 52.

Recall that we applied a correction for the steering shift resulting from the earth's magnetic field (Section E11, Chapter III). Because of the uncertainty in measuring $\int \vec{B} \cdot \hat{n}\, dl$ along the actual beam path, we have assigned an additional steering error to R equal to one half the C_{11} correction.

We have also assigned a further uncertainty to R because of the possible asymmetric steering effect of remnant fields (up to 10 Gauss) in the horizontal steering magnet B-29A along the beam path between TC20 and RS2 (see Fig. 51). This magnet was not energized during this experiment and the magnet was degaussed before our runs; however, later measurements showed that remnant fields $\sim$5 Gauss can exist even after degaussing.

The combination of these two uncertainties is shown in column 4 of Table VI. The total N/Q steering error, which is a combination of column 3 and $1/\sqrt{2}$ times column 4, is shown in column 5.

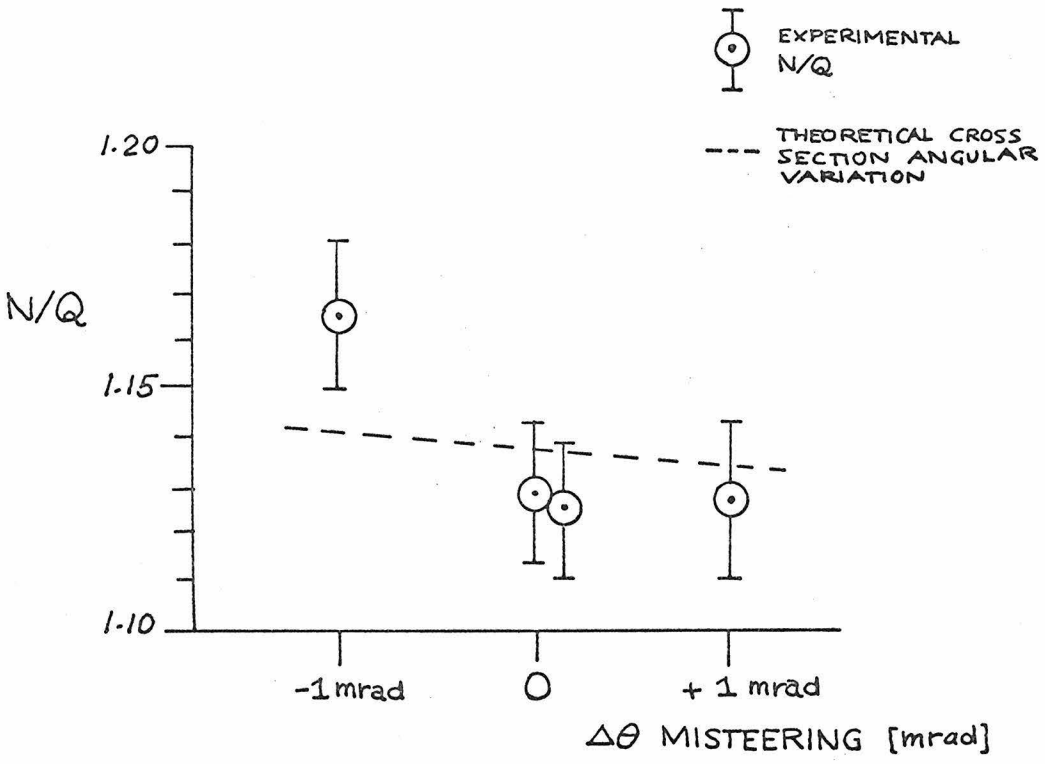

FIGURE 52: Comparison of the actual change in N/Q with the expected variation as a function of steering angle.

INCIDENT ENERGY E_o (GeV)	SCATTERING ANGLE θ (degrees)	% CHANGE in $d\sigma/d\Omega$ due to $\Delta\theta=\pm 0.02$ mrad (%)	UNCERTAINTY in R due to Field Uncertainty Affecting the Steering (%)	TOTAL UNCERTAINTY in N/Q due to Steering (%)
4	12.5	0.0695	0.347	0.255
4	20.0	0.0491	0.254	0.186
4	27.5	0.0356	0.179	0.131
4	35.0	0.0265	0.133	0.098
10	2.6	0.255	0.510	0.442
10	5.0	0.179	0.358	0.310
10	12.5	0.091	0.182	0.158
10	15.0	0.075	0.150	0.130

TABLE VI.

Breakdown of Steering Uncertainties

6. Uncertainty in the Beam Charge Monitor, ϵ_6

This was due to the discrepancy between $(Q_{FC}/Q_{Tor})_+$ and $(Q_{FC}/Q_{Tor})_-$ mentioned earlier (Section E4, Chapter II). A monitor uncertainty equal to the disagreement between these two ratios for each data point was applied to R. The size of this uncertainty is shown in Table VII.

7. Uncertainty in the Incident Beam Energy, ϵ_7

Within a given data point, the relative position of the elastic peak in a run can be calculated using the incident energy given by the switchyard flip coil (cf. Section C, Chapter II), the angle θ given by spectrometer encoder, and the relative momentum selecting field given by the NMR probes in the spectrometer magnets.

The relative peak positions calculated in this manner are shown with the actual peak positions in Fig. 53 for the data obtained on the 8-GeV/c spectrometer ($\theta \geq 12.5^{\circ}$ data). The relation used for calculating the relative positions is shown in Appendix F. Since we were concerned only with determining R, the absolute normalization of the calculated peak positions was chosen arbitrarily to obtain the best fit for a given data point.

The discrepancy between the calculated peak positions and the actual peak positions may be due to an error in any or all of the following: flip coil energy, encoder θ, or spectrometer NMR. However, because there does not appear to be any obvious reasons why the

WEEK of Data	INCIDENT ENERGY E_o (GeV)	SCATTERING ANGLE θ (degrees)	Beam Charge Monitor UNCERTAINTY (as applied to R) (%)
8/15	4	12.5	±2.02
9/6	4	12.5	±1.03
8/15	4	20.0	±2.00
9/6	4	20.0	±1.04
8/15	4	27.5	±0.73
9/6	4	27.5	±1.08
	4	35.0	±1.50
	10	2.6	±1.50
	10	5.0	±1.50
	10	12.5	±0.45
	10	15.0	±0.51

TABLE VII.

Beam Charge Monitor Uncertainty
for the Data in each
Week of Running

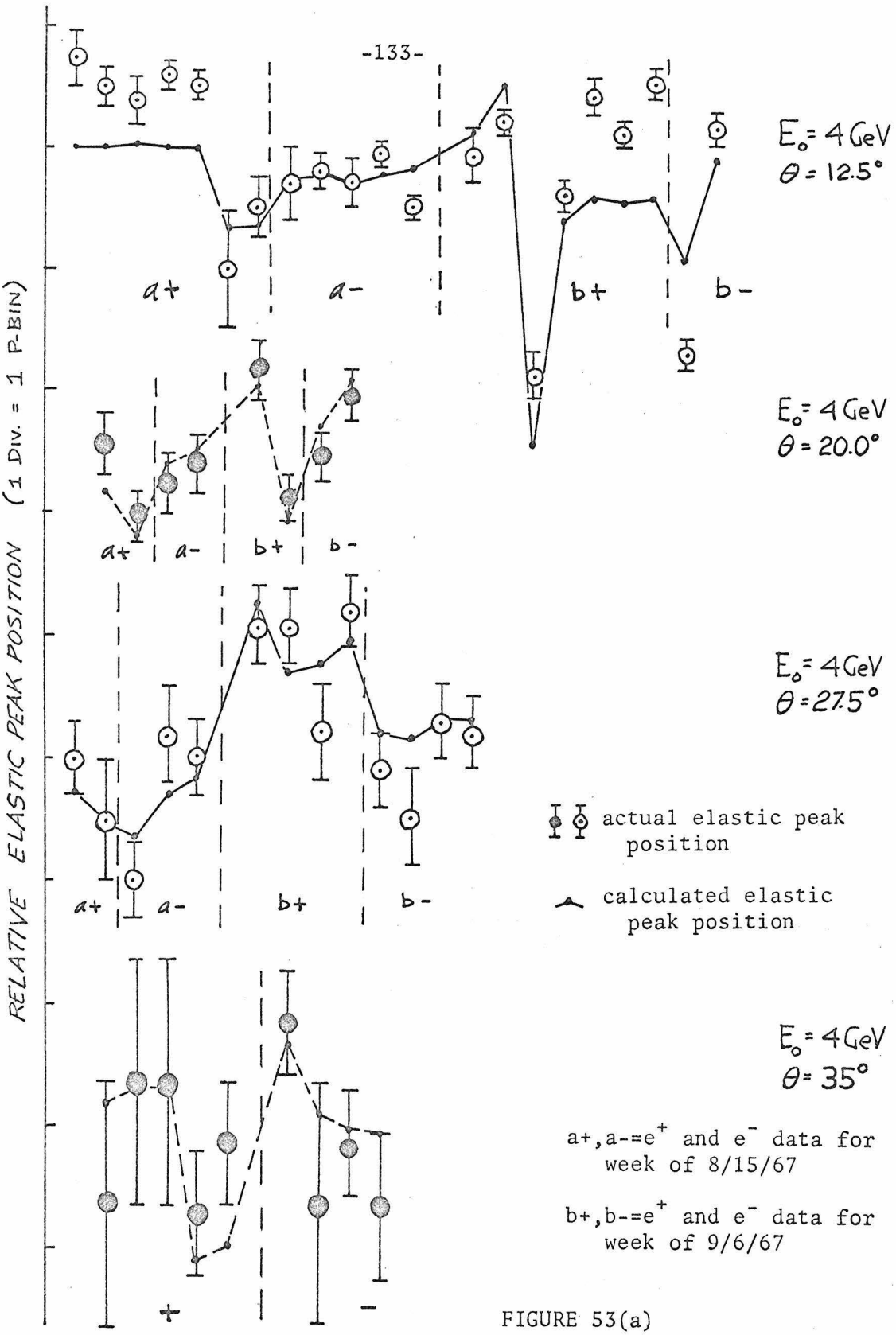
RELATIVE ELASTIC PEAK POSITION (1 DIV. = 1 P-BIN)
a+
a-
b+
b-
E₀ = 4 GeV
θ = 12.5°
E₀ = 4 GeV
θ = 20.0°
E₀ = 4 GeV
θ = 27.5°
E₀ = 4 GeV
θ = 35°
+
−
actual elastic peak position
calculated elastic peak position
a+, a-=e⁺ and e⁻ data for week of 8/15/67
b+, b-=e⁺ and e⁻ data for week of 9/6/67

FIGURE 53(a)

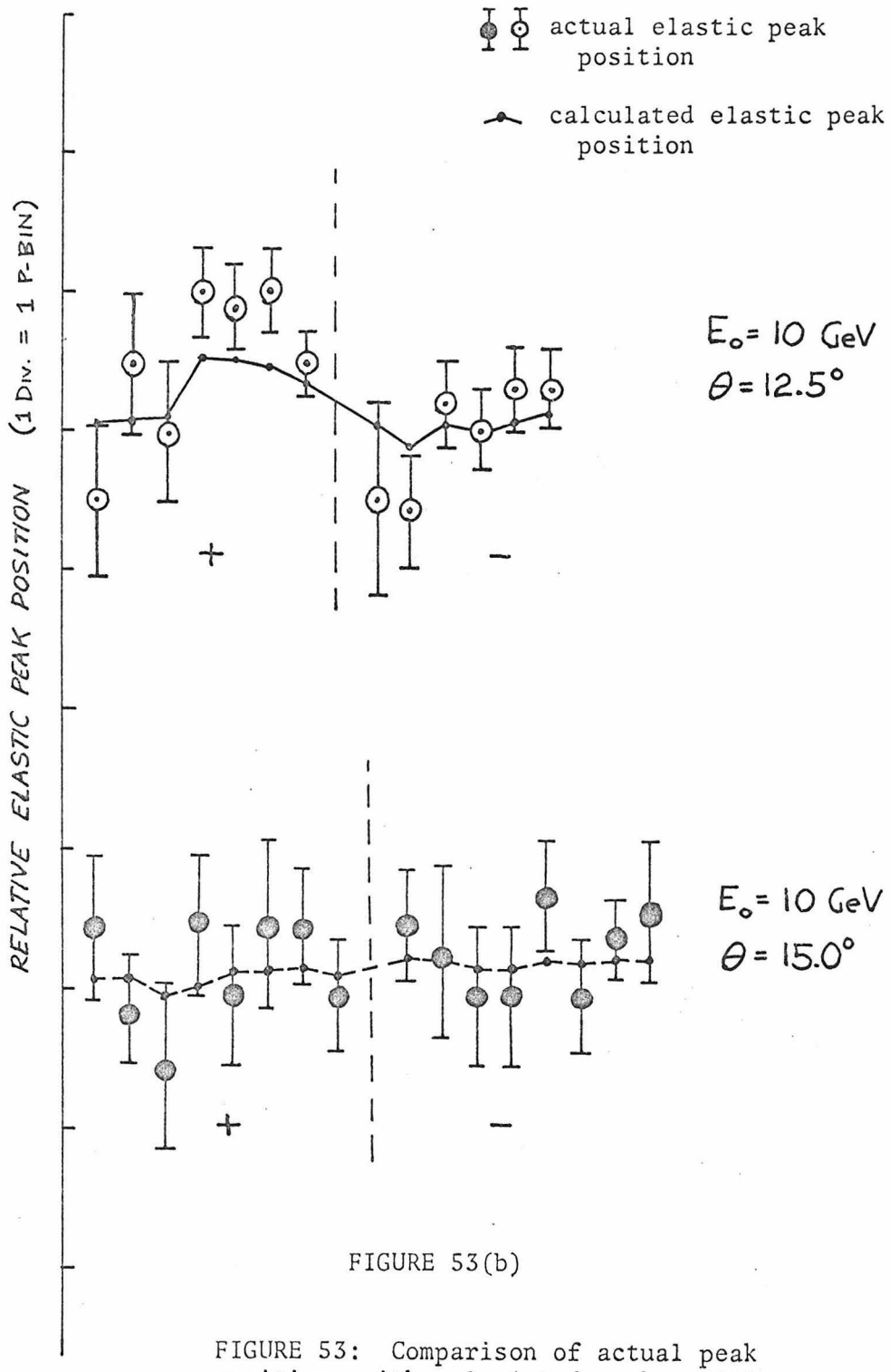

FIGURE 53(b)

FIGURE 53: Comparison of actual peak positions with calculated peak positions

encoder or spectrometer NMR was in error, we have assumed the error lies in the flip coil E_o. As a result, we have assigned an energy uncertainty to each run, equal to the energy shift required to explain the discrepancy in Fig. 53. Using the CS/EO's defined earlier (Section E3, this chapter), this energy uncertainty was transformed into an uncertainty in N/Q.

Since no NMR probes were used in the 20-GeV/c system, we could not directly estimate the E_o uncertainty for the $\theta \leq 5.0^o$ data. As a result, we have averaged the E_o=10 GeV uncertainties during the 8-GeV/c system runs and assumed that to be an estimate of the E_o uncertainty in the data taken with the 20-GeV/c system (all 20-GeV/c system data were taken with E_o=10 GeV).

The typical size of the uncertainties in the N/Q's due to the above energy uncertainty is shown in Table VIII.

8. Pion Contamination, ϵ_8

Asymmetric pion contamination was reduced to a negligible level in all but the 35^o data where it was reduced to less than (2±1)% (cf. Section D of this chapter). To account for this uncertainty, we have assigned a ±2% uncertainty to R for the 35^o data point.

Incident Energy E_o (GeV)	Scattering Angle θ (Degrees)	N/Q Uncertainty Due to E_o Uncertainty
4	12.5	±0.3%
4	20.0	±0.2%
4	27.5	±0.3%
4	35.0	±0.6%
10	2.6	±0.1%
10	5.0	±0.1%
10	12.5	±0.4%
10	15.0	±0.3%

TABLE VIII.

Typical Size of the N/Q Uncertainties Due to Uncertainty in Incident Energy, E_o

H. Combination of Errors

1. Uncertainty in N/Q

For a given run, the fractional uncertainty is simply the square root of the sum of the squares of the individual fractional uncertainties $\epsilon_1, \epsilon_2, \epsilon_3, \epsilon_4, \epsilon_5, \epsilon_6, \epsilon_7$, and ϵ_8 just mentioned. This is because the uncertainties we have been discussing refer to multiplicative factors applied to N/Q.

2. Uncertainty in R

As we mentioned earlier, the average $(N/Q)^+$ and $(N/Q)^-$ are obtained by averaging the (N/Q)'s for the runs of a given data point in the following manner:

$$\langle N/Q \rangle^{\pm} = \frac{\sum_i (N/Q)_i^{\pm} N_i^{\pm}}{\sum_i N_i^{\pm}}$$

i = sum over all ±e runs making up the data point

N_i = number of events used to make up N of N/Q

Since <N/Q> is made up of a linear combination of (N/Q)'s, and since the net error in linearly combined quantities can be shown to be:

$$\sigma(A+B+C+\ldots) = \{\sigma(A)^2+\sigma(B)^2+\sigma(C)^2+\ldots + 2(\langle(A-\overline{A})(B-\overline{B})\rangle+\langle(A-\overline{A})(C-\overline{C})\rangle+\ldots)\}^{\frac{1}{2}}$$

Where:

$\sigma(A)$ = uncertainty in A
$\sigma(B)$ = uncertainty in B
etc.
$\overline{A}$ = average value of A
$\overline{B}$ = average value of B
etc.

(If A, B, C, ... are independent, this reduces to:

$$\sigma(A+B+C+\ldots) = \{\sigma(A)^2+\sigma(B)^2+\sigma(C)^2+\ldots\}^{\frac{1}{2}}$$

we can compute the uncertainty in $\langle N/Q \rangle$ in a straightforward manner.

Since the uncertainties $\epsilon_1, \epsilon_2, \epsilon_3, \epsilon_4, \epsilon_5'$ (where ϵ_5' is the ±0.02 mrad steering uncertainty - we will call the steering uncertainty due to the earth's field and remnant fields ϵ_5''), and ϵ_7 discussed previously are independent from one run to the next, we can use the second relation above to combine them. Hence, the error due to $\epsilon_1, \epsilon_2, \epsilon_3, \epsilon_4, \epsilon_5'$, and ϵ_7 is:

$$\sigma(\langle N/Q \rangle)_{\substack{\text{Due to} \\ \epsilon_1 \epsilon_2 \epsilon_3 \epsilon_4 \\ \epsilon_5' \epsilon_7}} = \sqrt{\frac{\sum_{\substack{i \\ \text{RUNS}}} \left[\epsilon_1(i)^2 \; \epsilon_2(i)^2 \; \epsilon_3(i)^2 \; \epsilon_4(i)^2 \; \epsilon_5'(i)^2 \; \epsilon_7(i)^2 \right] N_i^2 \left(N/Q\right)_i^2}{\left(\sum_{\substack{i \\ \text{RUNS}}} N_i \right)^2}}$$

The fractional error due to $\epsilon_1, \epsilon_2, \epsilon_3, \epsilon_4, \epsilon_5'$, and ϵ_7 is simply given by:

$$\epsilon(\langle N/Q \rangle)_{\substack{\text{Due to} \\ \epsilon_1 \epsilon_2 \epsilon_3 \epsilon_4 \\ \epsilon_5' \epsilon_7}} = \frac{\sigma(\langle N/Q \rangle)_{\substack{\text{Due to} \\ \epsilon_1 \epsilon_2 \epsilon_3 \epsilon_4 \epsilon_5' \epsilon_7}}}{\langle N/Q \rangle}$$

The uncertainty in N/Q due to the steering error resulting from the uncertainty in the earth's field along the beam path and the possible remnant field in the B-29A magnet (cf. Section G5, Chapter III), is the same for all runs of a given data point. Therefore:

$$\epsilon(\langle N/Q \rangle)_{\substack{\text{Due to} \\ \epsilon_5''}} = \frac{1}{\sqrt{2}} \left(\begin{array}{l} \text{Uncertainty in R from Column 4} \\ \text{of Table VI} \end{array} \right)$$

The monitor uncertainty was also the same for all the runs of a given data point, so we need only apply it to the final $\langle N/Q \rangle$:

$$\epsilon\left(\langle N/Q\rangle\right)_{\substack{\text{Due to}\\ \epsilon_6}} = \frac{1}{\sqrt{2}}\left(\begin{array}{c}\text{Beam monitor uncertainty in R,}\\ \text{from Table VII}\end{array}\right)$$

The same was also true for the pion contamination. There:

$$\epsilon\left(\langle N/Q\rangle\right)_{\substack{\text{Due to}\\ \epsilon_8}} = \frac{1}{\sqrt{2}}\begin{cases} 2 \times 10^{-2} & \text{for the } 35^{\circ} \text{ data} \\ 0 & \text{otherwise}\end{cases}$$

Hence, the total fractional error in $\langle N/Q\rangle$ is given by:

$$\epsilon\left(\langle N/Q\rangle^{\pm}\right) = \sqrt{\epsilon\left(\langle N/Q\rangle^{\pm}\right)^2_{\substack{\text{Due to}\\ \epsilon_1\,\epsilon_2\,\epsilon_3\,\epsilon_4\\ \epsilon_5',\,\epsilon_7}} + \epsilon\left(\langle N/Q\rangle^{\pm}\right)^2_{\substack{\text{Due to}\\ \epsilon_5''}} + \epsilon\left(\langle N/Q\rangle^{\pm}\right)^2_{\substack{\text{Due to}\\ \epsilon_6}} + \epsilon\left(\langle N/Q\rangle^{\pm}\right)^2_{\substack{\text{Due to}\\ \epsilon_8}}}$$

Since R is the ratio $\langle N/Q\rangle^{+}/\langle N/Q\rangle^{-}$, the fractional error in R is then:

$$\epsilon(R) = \sqrt{\epsilon\left(\langle N/Q\rangle^{+}\right)^2 + \epsilon\left(\langle N/Q\rangle^{-}\right)^2}$$

IV. MISCELLANEOUS EFFECTS

A. Inelastic $e^{\pm}p$ Contamination

There is the possibility that some of the electron events making up N/Q, especially those that were assumed to be a part of the elastic radiative tail, are electrons that have scattered inelastically.

eg. $e\ p \rightarrow e\ p\ \pi^o$

$e\ p \rightarrow e\ n\ \pi^+$

$e\ p \rightarrow e\ p\ \pi^+\ \pi^-$

Because of the mass of the pion (139 MeV) or pions, the threshold for such reactions occurs below the elastic peak, as is shown in Fig. 26.

For the E_o = 4 GeV data, the inelastic threshold is completely off the θ-p hodoscope plane so that such effects are not relevant there.

For the 10 GeV data however, the inelastic threshold is approximately 16 p-bins below the elastic peak, so inelastic contamination may be a problem there.

However, if we use the semi-empirical relations of Hand and Wilson[15] to estimate the inelastic cross section for resonant pion production in the vicinity of the N*(1238), then it can be shown that the ratio of inelastic to elastic cross sections is:

$$\frac{d\sigma_{In}}{d\sigma_{El}} = \frac{C\left(\frac{E_o}{\tau}\right)\left(\frac{\tau}{1+\tau} + 2\tau \tan^2\frac{\theta}{2}\right)\left|G_{MV}\right|^2}{\left(\frac{\tau}{1+\tau} + 2\tau\tan^2\frac{\theta}{2}\right)\left|G_{Mp}\right|^2 + \frac{1}{1+\tau}\left|G_{Ep}\right|^2}$$

$$\lesssim C \frac{E_o}{\tau} \left| \frac{G_{MV}}{G_{MP}} \right|^2 \sim C \frac{E_o}{\tau} = C' \frac{E_o}{q^2}$$

Where: C = constant
$\tau = -q^2/4M^2$
G_{EP}, G_{MP} = Electric and Magnetic form factors for the proton
G_{MV} = Magnetic Isovector form factor
($G_{MV} = (G_{MP} - G_{Mn})/2$, where G_{Mn} = neutron magnetic form factor)

Thus the ratio of inelastic to elastic cross section goes as $\sim E_o/q^2$.

This leads us to expect the greatest inelastic contamination to occur in the E_o=10 GeV, θ=2.6° data point, where E_o/q^2=49, and is the largest of all the data points.

To obtain an estimate of the inelastic contribution to the elastic data at that point, an attempt was made to subtract the radiative tail from the data - thus leaving only the inelastic contribution. The theoretically calculated radiative tail is shown with the experimental tail in Fig. 54. The method used to generate the theoretical radiative tail is described in Appendix G. From Fig. 54 it is clear that the inelastic contribution is less than 10%.

From the E_o/q^2 behavior, the inelastic contribution in the E_o=10 GeV, θ=5.0° data should be even less. However, to guard against an asymmetry in inelastic ep scattering biasing our elastic results, we have also measured R with the spectrometer hodoscope plane centered about the (3,3) resonance at θ=2.6° and 5.0°, at an incident energy of 10 GeV. This was achieved by lowering the field of the bending magnets in the spectrometer so that the θ-p plane detected electrons

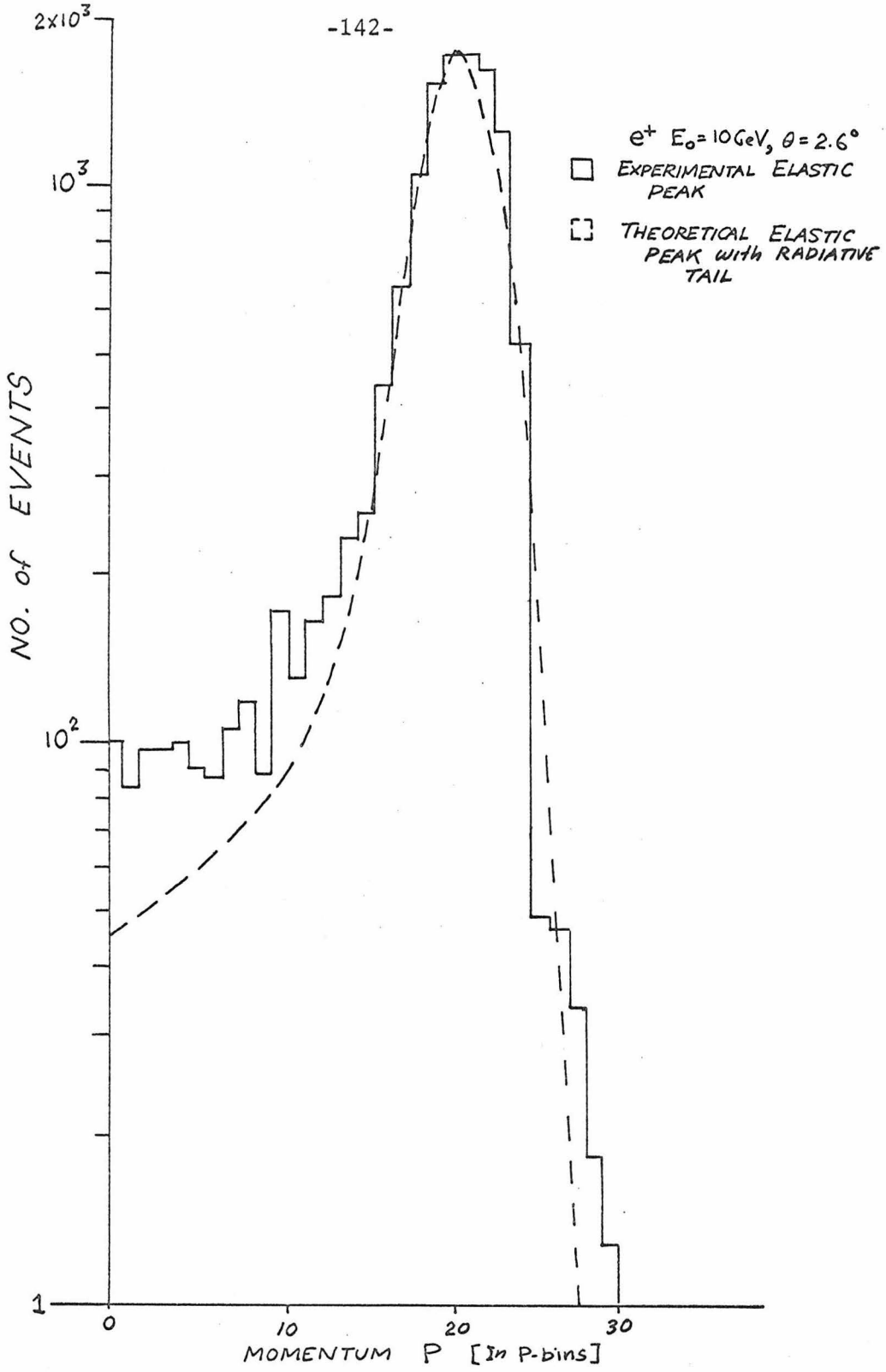

FIGURE 54: Comparison of Theoretical Radiative Tail With Experimental Tail

or positrons in which the mass of the undetected particles (missing mass) were contained in the range ~1110 MeV to ~1370 MeV. In both the 2.6^{o} and 5.0^{o} data, R was consistent with 1.

The remaining E_o=10 GeV data, at $\theta=12.5^{o}$ and 15.0^{o}, had $E_o/q^2 \leq$ 2.54, which is more than 19 times smaller than the E_o/q^2 for the 2.6^{o} point. Since the inelastic contribution at 2.6^{o} was less than 10%, the inelastic contribution at 12.5^{o} and 15.0^{o} should have been less than 0.5%, which is negligible in comparison with the statistical accuracy.

B. Annihilation Losses of Positrons

Another matter that must be considered is the asymmetric loss of positrons from positron annihilation. Incoming positrons may annihilate in the windows and in the hydrogen target before scatter, thus reducing the actual incident beam charge to a value lower than that measured by the toroid. Scattered positrons may annihilate in the hydrogen target, windows, counters, etc. and cause the number of detected scatterings to be below the number of actual scatterings. Both processes would tend to make the e^+ experimental cross section lower than actual.

We have estimated the loss of positrons by calculating the fractional loss in a positron beam going through an equivalent amount of material. Since the positrons are of high energy, we have treated the positron-atomic electron interaction using the following annihilation cross section[16], which is based on the interaction of free electrons and positrons:

$$\sigma = \frac{r_o^2 \pi}{\beta^2 \gamma(\gamma+1)} \left[\left(\gamma + 4 + \frac{1}{\gamma}\right) \ln\left(\gamma + \sqrt{\gamma^2-1}\right) - \beta(\gamma+3) \right]$$

Where: γ = incident energy of positron in rest mass units

$\beta \cong 1$, for our energies

r_o = classical electron radius 2.82×10^{-13} cm

This relation is based on the diagram shown in Fig. 55.

Now in a given material, the number of annihilations per unit time will be:

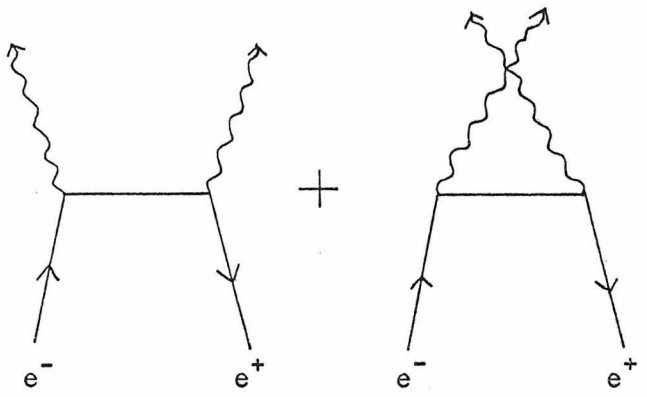

FIGURE 55:

Lowest order annihilation diagram for free e^+ and e^-

$$N_{Ann} = N_{inc} N_\rho \sigma$$

Where:
N_{inc} = incoming positron flux
N_ρ = number of electrons/unit vol.
σ = annihilation cross section given previously

or for a number of different mediums, we have:

$$N_{Ann} = \left(\sum_i \int_o^{\ell_i} N_{inc}(x_i) N_\rho(i) dx_i \right) \sigma$$

Where i is summed over the mediums
$N_\rho(i)$ = is the electron density (per unit vol.) in medium i
ℓ_i = traversal length in medium i

Since N_{Ann} will be small, N_{inc} = constant in all the mediums, therefore:

$$\frac{N_{Ann}}{N_{inc}} \cong \left(\sum N_\rho(i) \ell_i \right) \sigma$$

Thus an estimate of the annihilation losses is given by:

$$f_{Ann} = \begin{matrix}\text{Fractional} \\ \text{Annihilation} \\ \text{Loss}\end{matrix} \cong \left(\sum_{\substack{i \\ \text{Before} \\ \text{Scatter}}} N_\rho(i) \ell_i \right) \sigma(E_o) + \left(\sum_{\substack{j \\ \text{After} \\ \text{Scatter}}} N_\rho(j) \ell_j \right) \sigma(E')$$

Where i = sum over mediums before scatter
j = sum over mediums after scatter
E_o = incident positron energy
E' = scattered positron energy

For the conditions under which the 12.5^o data was taken:

$$\sum_i N_\rho(i) \ell_i \cong 6.03 \times 10^{23} \text{ cm}^{-2}$$

$$\sum_j N_\rho(j) \ell_j \cong 20.87 \times 10^{23} \text{ cm}^{-2}*$$

we obtain the values for f_{Ann} given in Table IX.

---

* The largest contribution to this comes from the hodoscope, which contributed 14.0×10^{23} cm^{-2} of $\sum_j N_\rho(j) \ell_j$

INCIDENT ENERGY E (GeV)	SCATTERING ANGLE θ (degrees)	Fractional Annihilation Loss of Positrons f_{Ann}
4	12.5	7.95×10^{-4}
4	20.0	8.73×10^{-4}
4	27.5	9.83×10^{-4}
4	35.0	1.12×10^{-3}
10	12.5	3.86×10^{-4}
10	15.0	4.10×10^{-4}

TABLE IX

Estimated Fractional Annihilation Loss of Positrons

Since $\sum_i N_\rho(i)\ell_i$ and $\sum_j N_\rho(j)\ell_j$ were even smaller for the E_o=10 GeV, θ=2.6^o and 5.0^o data, we conclude that annihilation losses affect R by $\lesssim$0.1%, a negligible amount.

It should be mentioned that energetic photons resulting from the annihilations may introduce an asymmetric background, particularly by photoproducing pions. However, as we described earlier, pion contamination was reduced to a negligible level by use of a shower counter and a dE/dX counter.

V. RESULTS

Measurements of R for elastic scattering were made for eight different data points: E_o= 4 GeV, θ=12.5°, 20.0°, 27.5°, 35.0° and E_o= 10 GeV, θ=2.6°, 5.0°, 12.5°, 15.0°. The angle-energy region of our elastic measurements of R are shown with previous measurements[2] of R in Fig. 56.

Two measurements of R for "inelastic" scattering (there was ∿20% contribution from the radiative tail of the elastic peak in the data) in the region of the N*(1238) were made at E_o=10 GeV, θ=2.6° and 5.0°.

A. Consistency Check

The data was collected in a sequence of runs which alternated between positrons and electrons. The chronological sequence of data runs, with their identifying run numbers, are shown in Table X. For each of these runs, a corrected N/Q was obtained. The N/Q's for each of these runs are shown in Figures 57, 58, 59,..., 66. In each of these figures, all the positron runs and all the electron runs are grouped together, except for the data taken several weeks apart.

Note that there appears to be a shift between the E_o=4 GeV data taken during the week of August 15th, 1967 and that taken during the week of September 6, 1967. The reason for this shift is not known.

The average N/Q for this data, as well as the mean χ^2 and standard deviation, defined by:

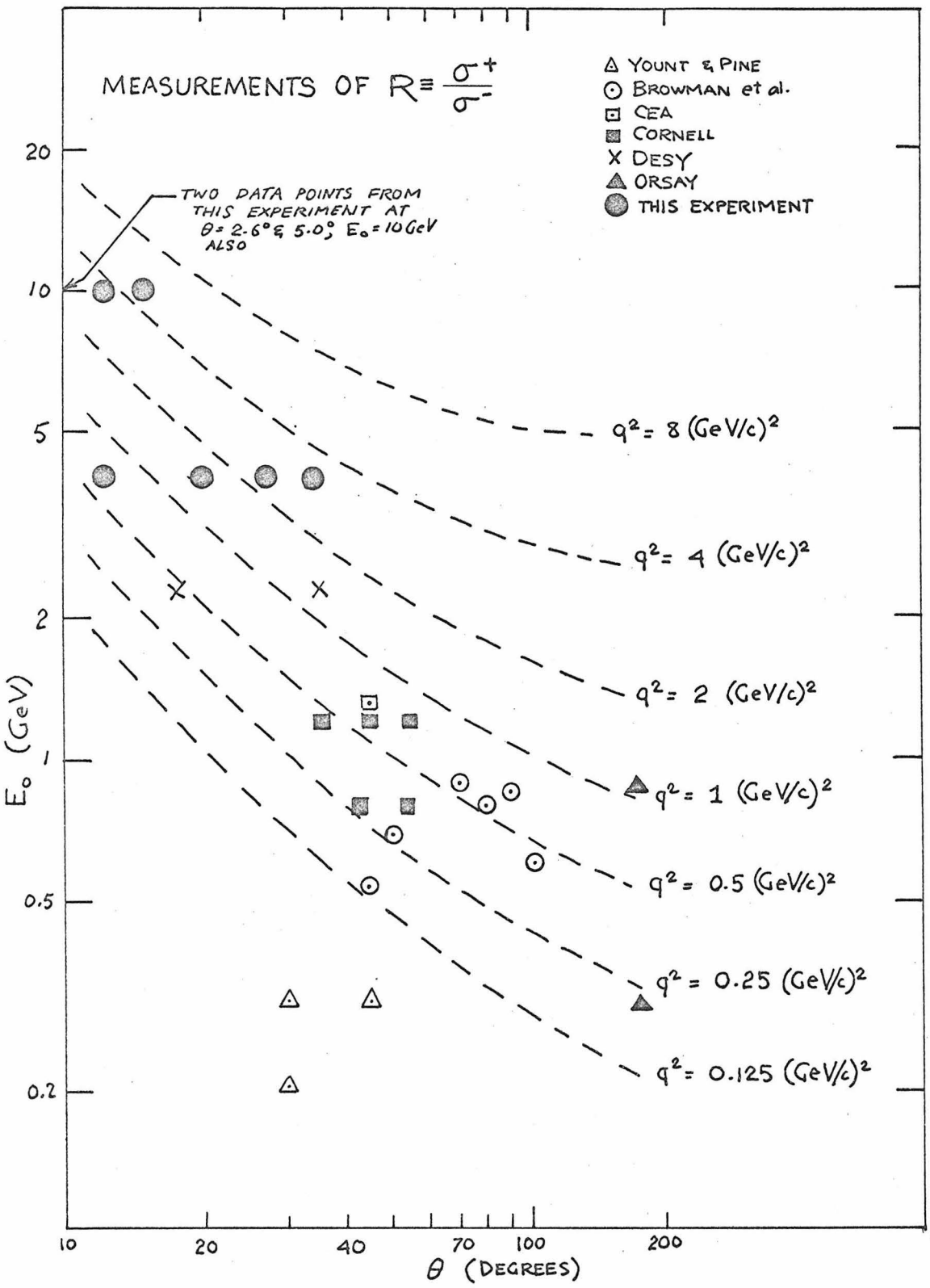
MEASUREMENTS OF $R \equiv \frac{\sigma^+}{\sigma^-}$
YOUNT & PINE
BROWMAN et al.
CEA
CORNELL
DESY
ORSAY
THIS EXPERIMENT
TWO DATA POINTS FROM THIS EXPERIMENT AT θ = 2.6° & 5.0°, E₀ = 10 GeV ALSO
$q^2 = 8$ (GeV/c)²
$q^2 = 4$ (GeV/c)²
$q^2 = 2$ (GeV/c)²
$q^2 = 1$ (GeV/c)²
$q^2 = 0.5$ (GeV/c)²
$q^2 = 0.25$ (GeV/c)²
$q^2 = 0.125$ (GeV/c)²
E₀ (GeV)
20
10
5
2
1
0.5
0.2
10
20
40
70
100
200
θ (DEGREES)

FIGURE 56.

WEEK OF 8/15/67
E_0 = 4 GeV

θ = 12.5°	20.0°	27.5°
2102		
2103		
2106		
	2107	
		2108
2110		
2111		
-2113		
-2114		
-2115		
	-2116	
	-2117	
		-2118
		-2119
		-2120
-2121		
-2122		
2125		
2126		
	2127	
		2128

E_0 = 10 GeV

θ = 12.5°	θ = 15.0°
2130	
2131	
2132	
-2135	
⋮	
-2138	
	-2139
	⋮
	-2143
	2144
	⋮
	2147
2148	
2149	
-2151	
-2152	
	-2154
	-2155
	-2156
	2158
	⋮
	2161
2162	
2163	

WEEK OF 9/6/67
E_0 = 4 GeV

θ = 12.5°	20.0°	27.5°	35.0°
2168			
			2170
			2171
			-2172
-2173			
	-2176		
		-2177	
		-2178	
2179			
	2182		
		2185	
			2186
			2187
			-2188
			-2189
			-2190
-2191			
	-2192		
		-2193	
		-2194	
2195			
2197			
	2198		
2199			
2200			
		2201	
		2202	
		2203	
			2204
			2205
	2210		

WEEK OF 9/28/67
E_0 = 10 GeV

* Denotes dummy target run

ELASTIC θ = 2.6°	N*(1238) θ = 2.6°
	2213
	*2214
*2215	
2216	
-2217	
-*2218	
	-*2219
	-2220
	-2223
-2224	
2226	

ELASTIC θ = 5.0°	N*(1238) θ = 5.0°
2228	
*2229	
	2230
	*2231
-2232	
-*2233	
	-2234
	-*2235

TABLE X.

Chronological sequence of data runs. The "-" runs represent the e^-p data, the others, the e^+ data.

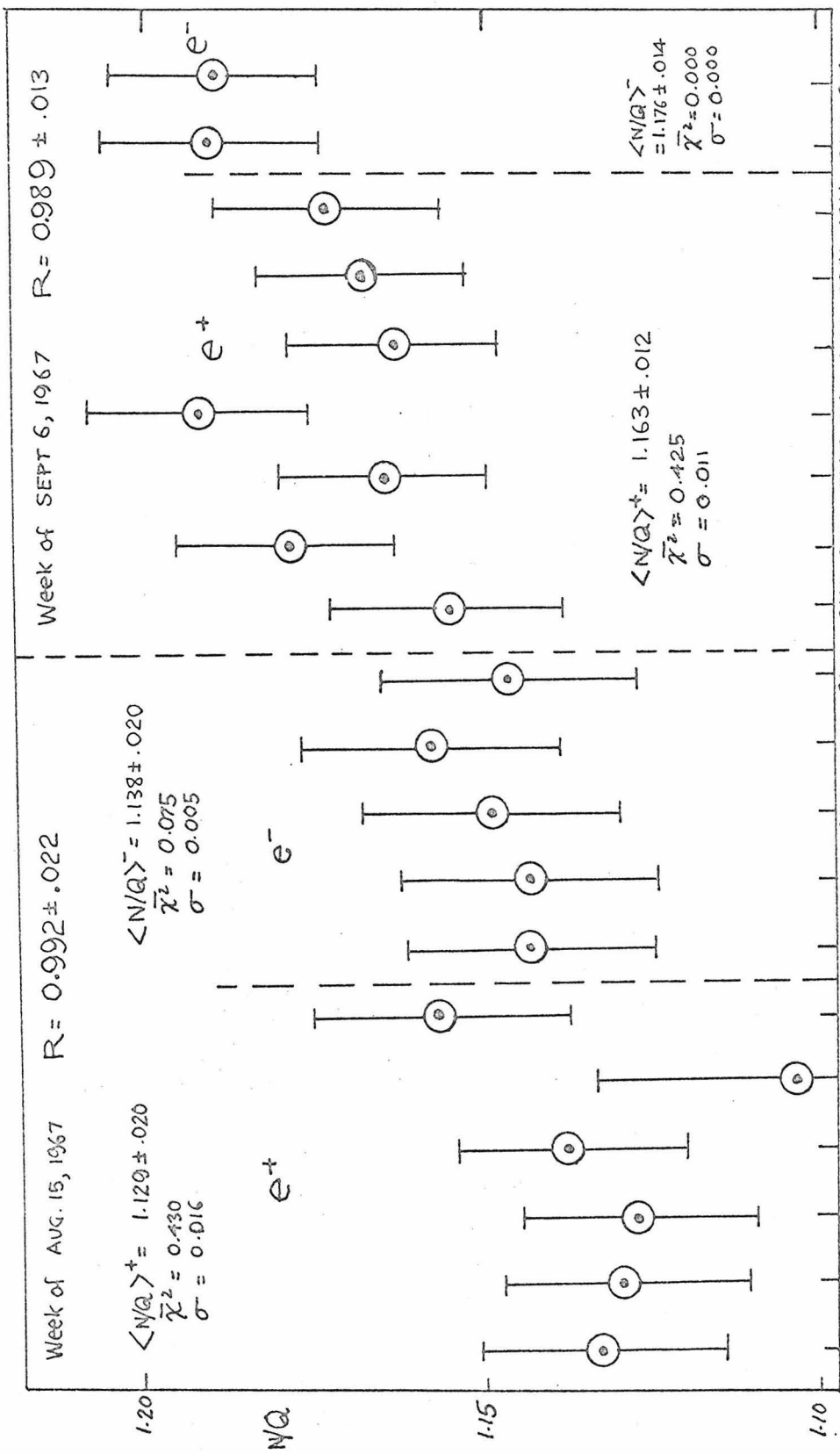

FIGURE 57: N/Q's for E_o=4 GeV, θ=12.5° data

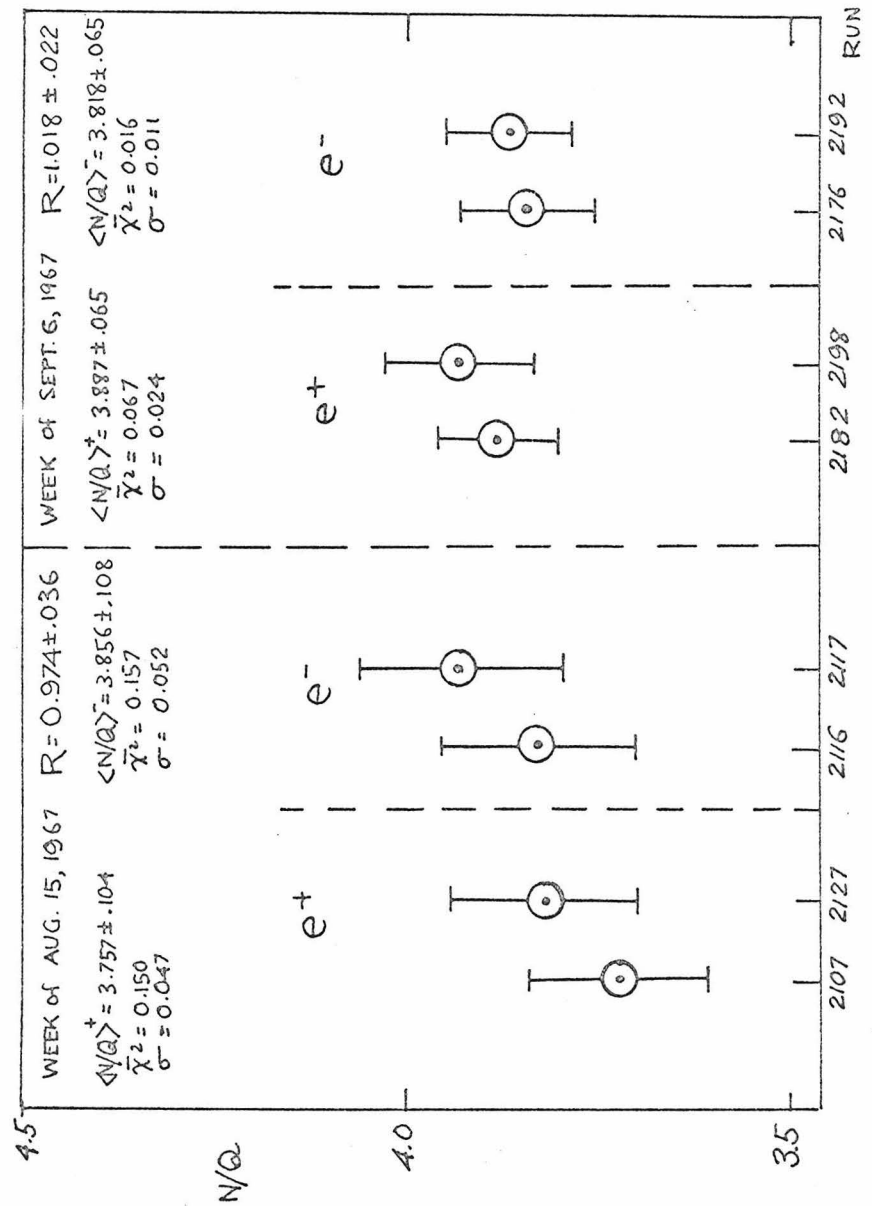

FIGURE 58:
N/Q's for E_o=4 GeV, θ=20.0° data

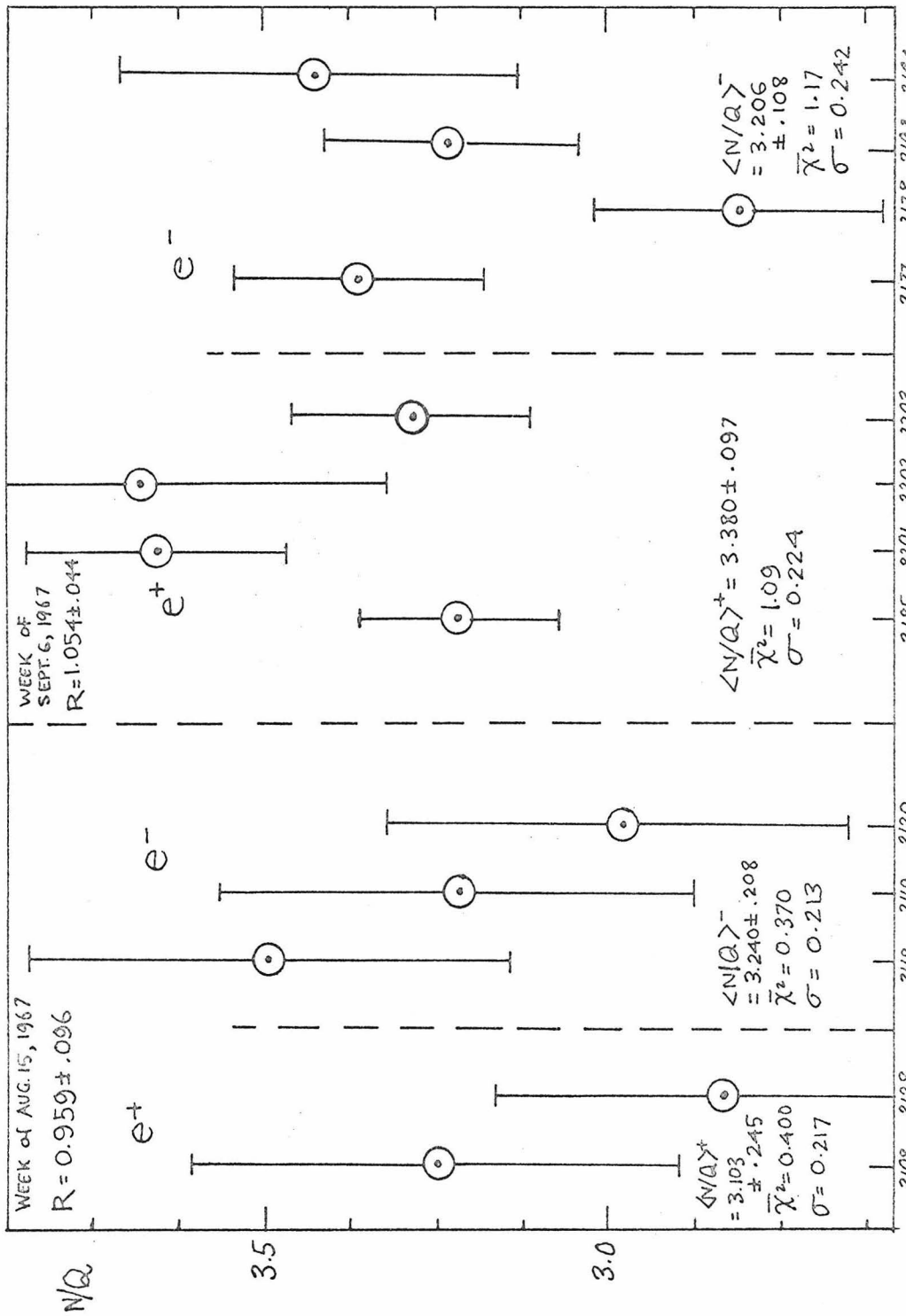

FIGURE 59: N/Q's for E_o=4 GeV, θ=27.5^o data

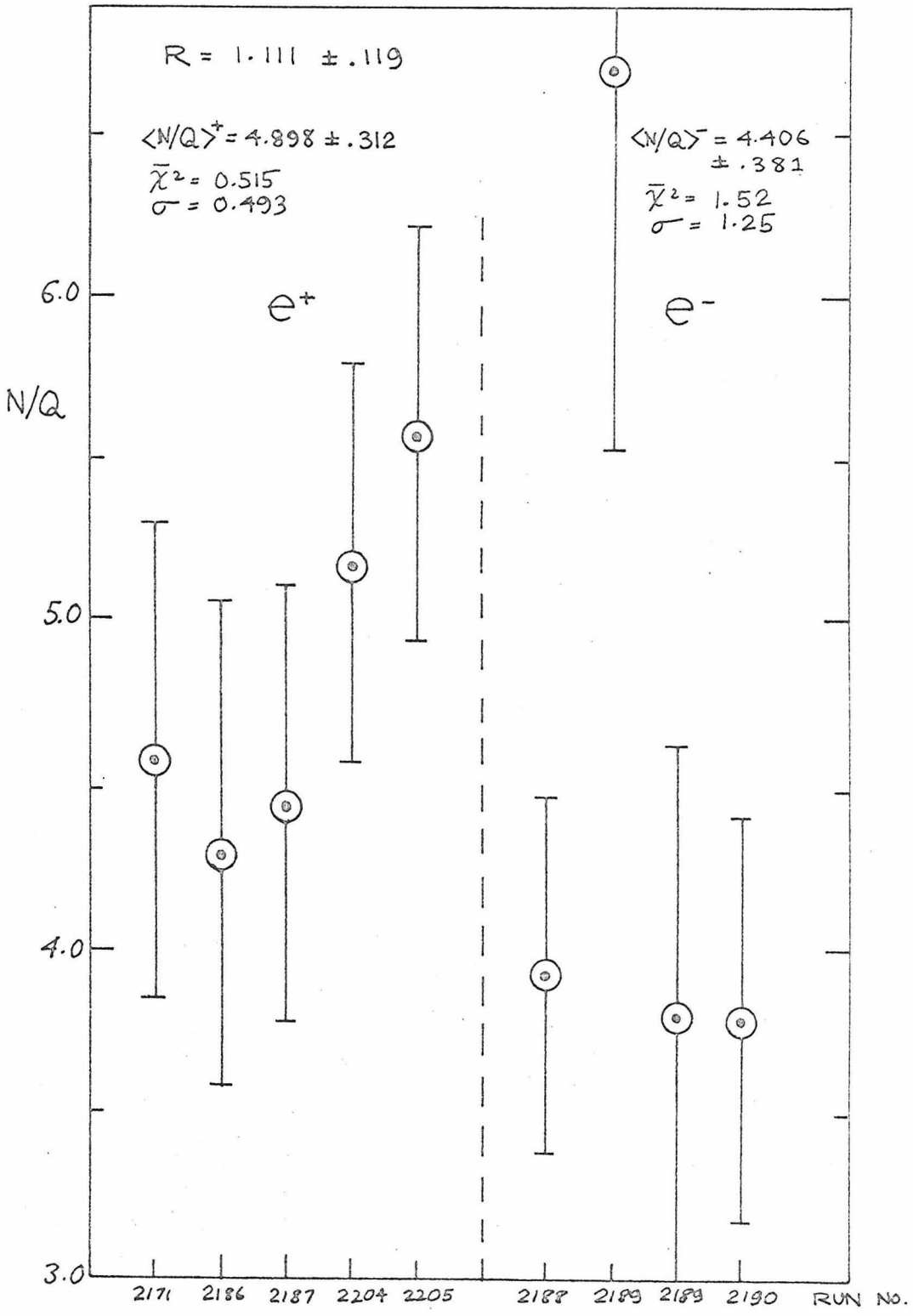

FIGURE 60: N/Q's for E_o=4 GeV, θ=35.0° data

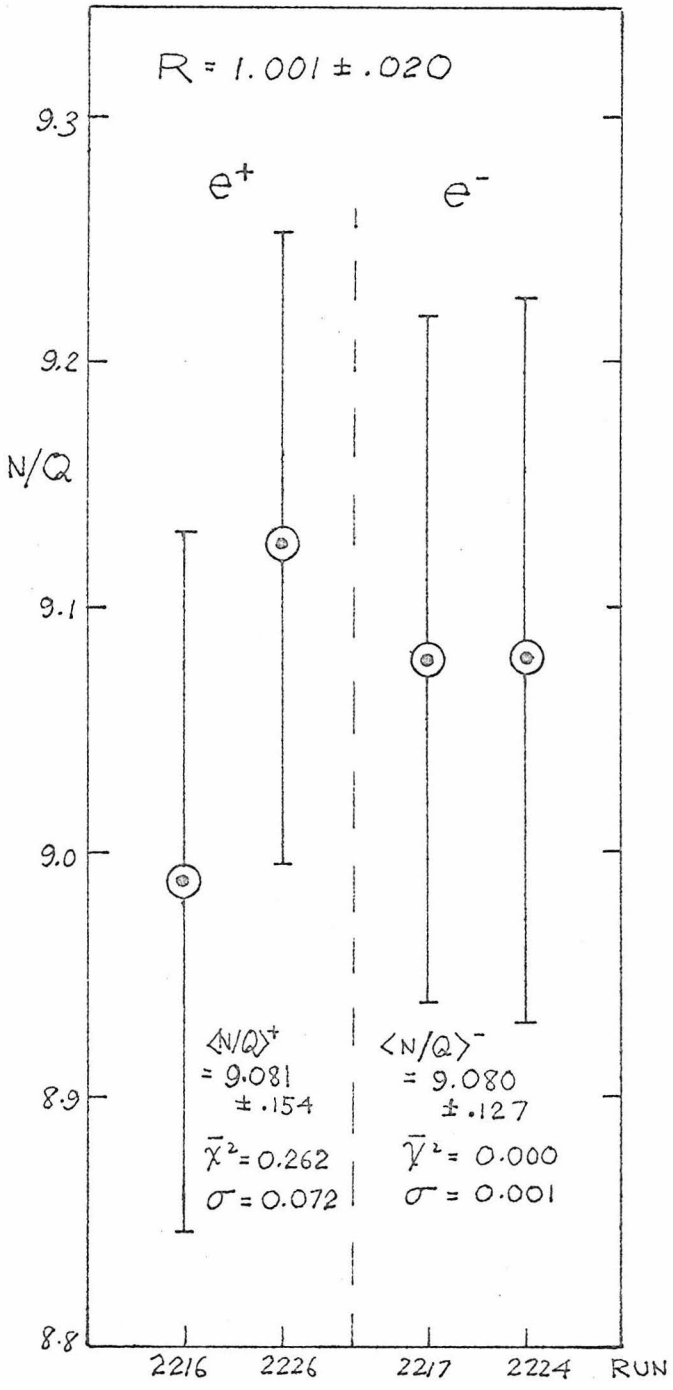

FIGURE 61: N/Q's for E_o=10 GeV, θ=2.6° data

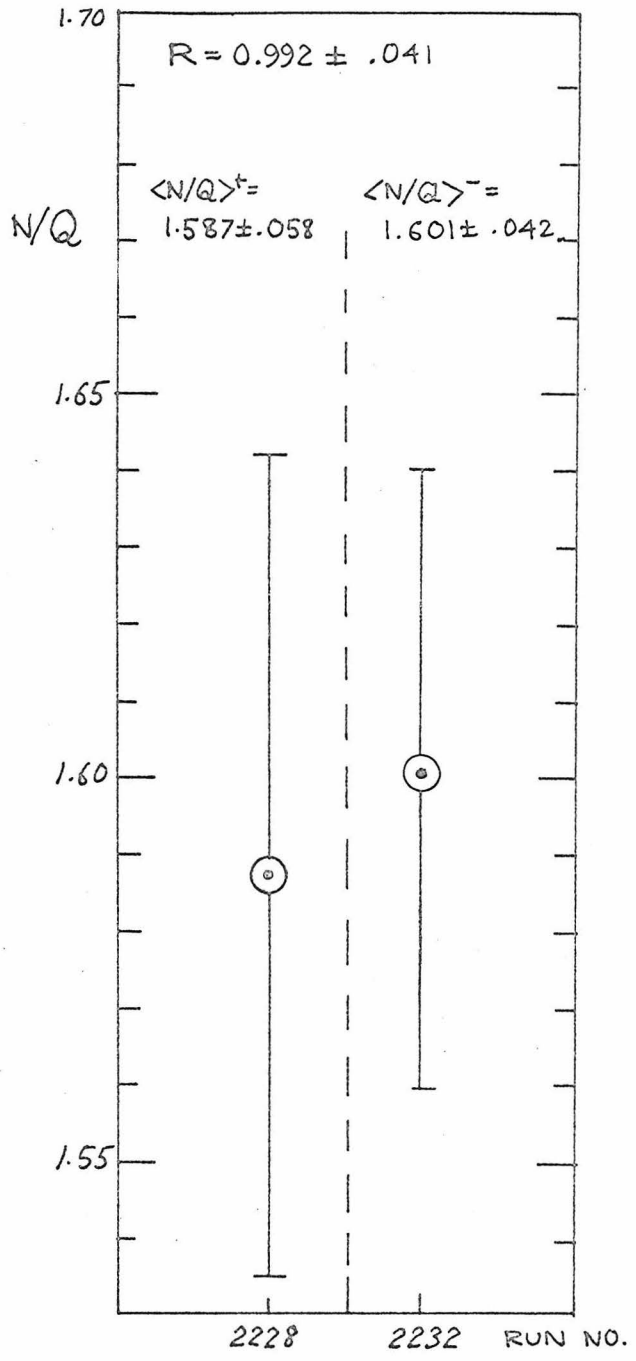

FIGURE 62: N/Q's for E_o=10 GeV, θ=5.0° data

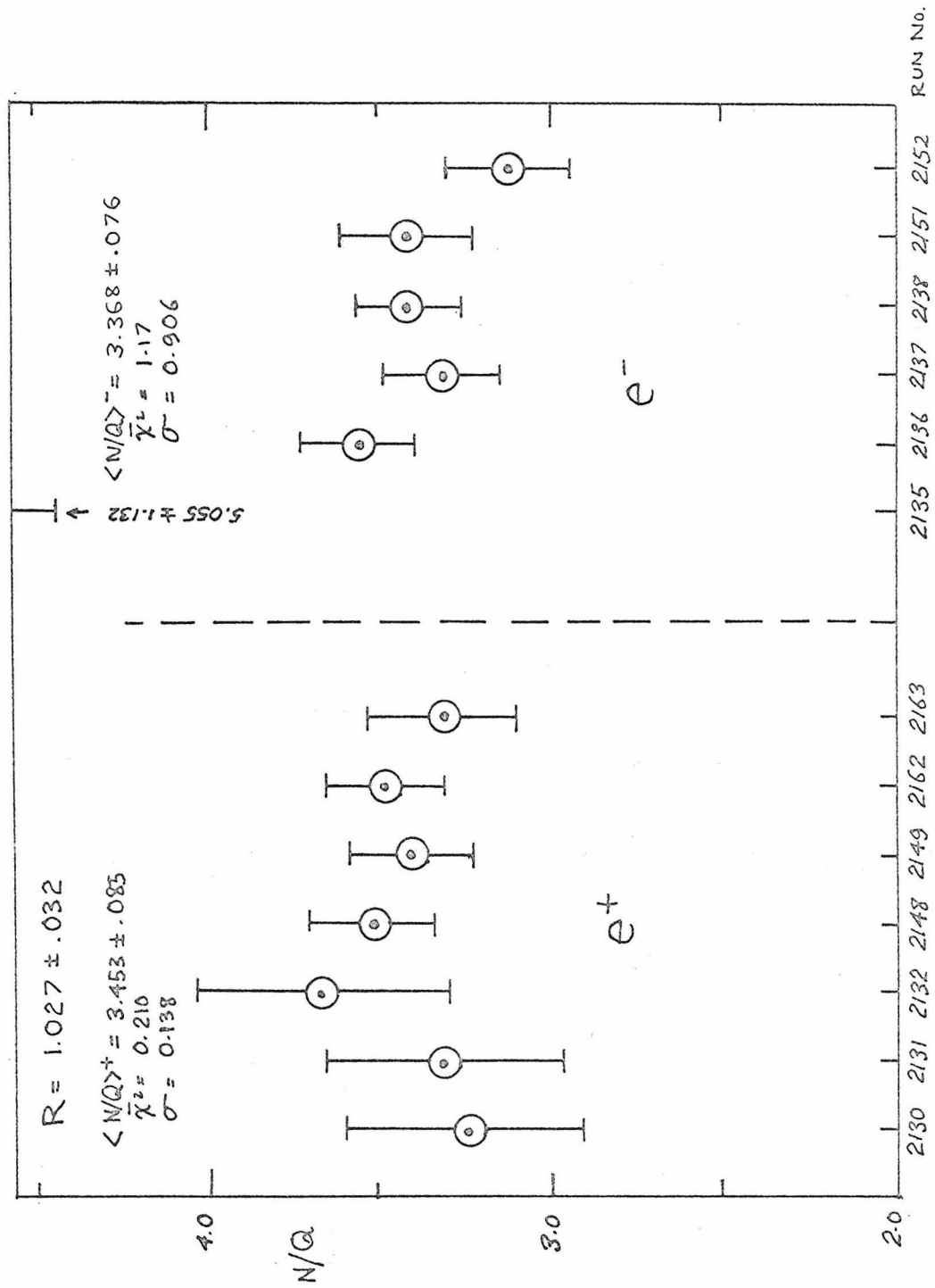

FIGURE 63: N/Q's for E_o=10 GeV, θ=12.5° data

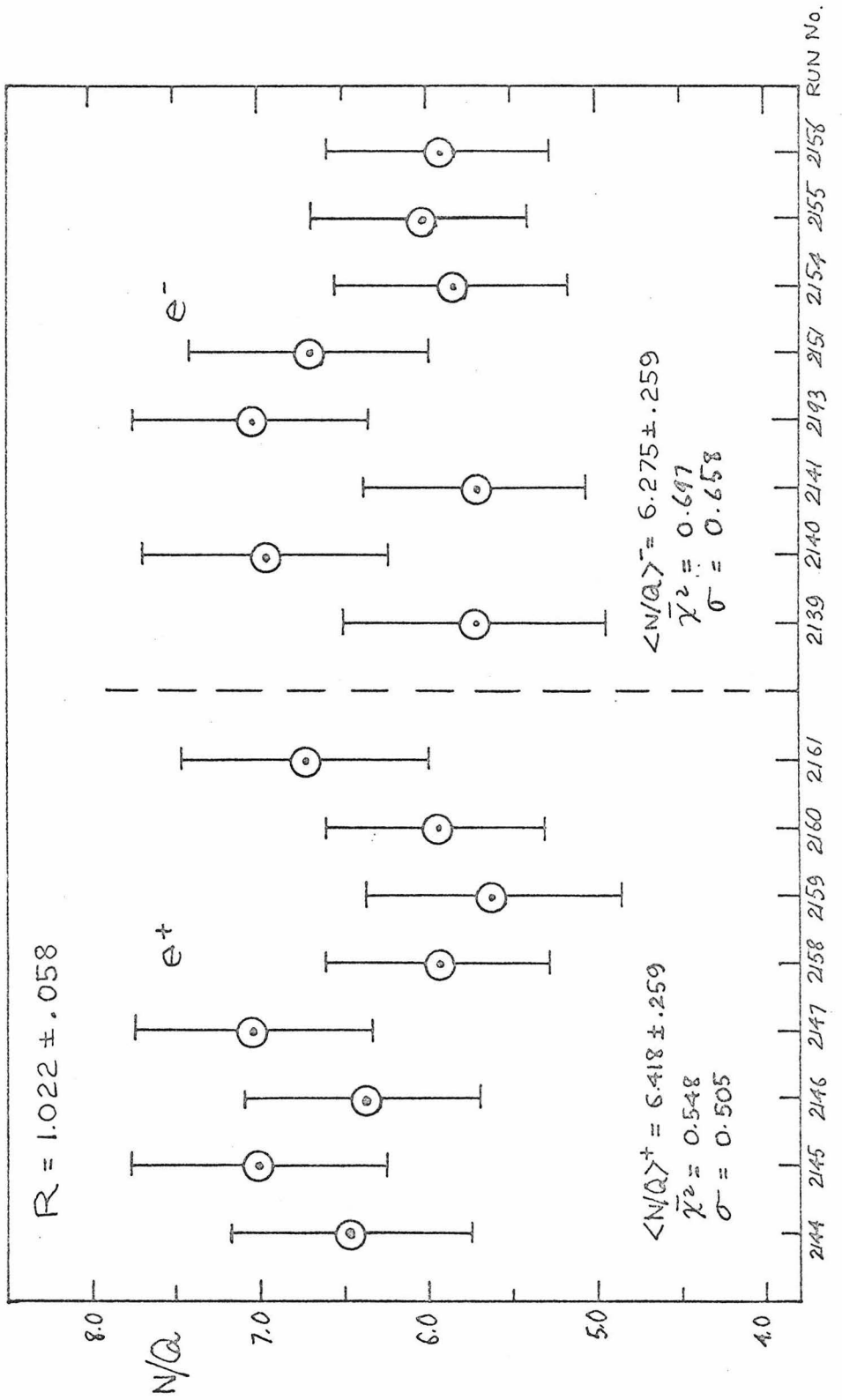

FIGURE 64: N/Q's for E_o=10 GeV, θ=15.0° data

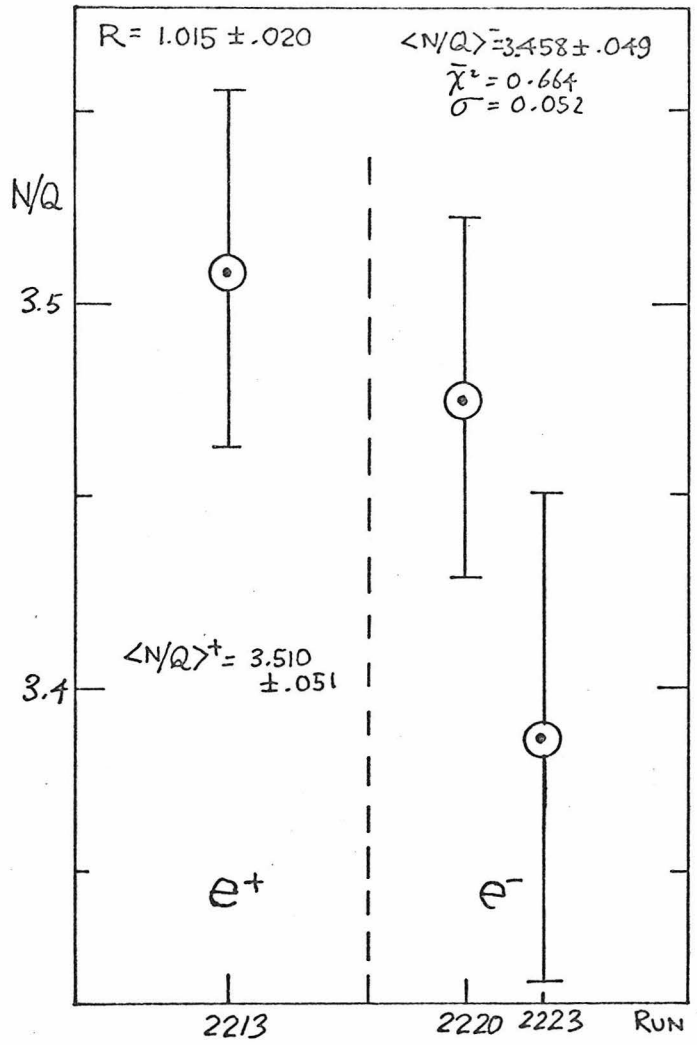

FIGURE 65: N/Q's for N*(1238) at E_o=10 GeV, θ=2.6°

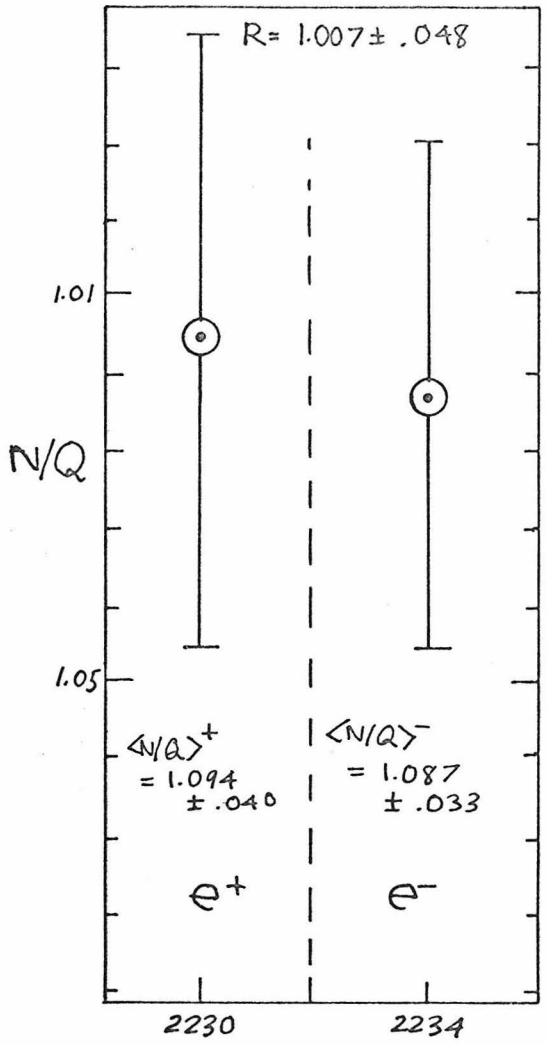

FIGURE 66: N/Q's for N*(1238) at E_o=10 GeV, θ=5.0°

$$\text{Mean } \chi^2 \equiv \bar{\chi}^2 = \frac{\sum_{i=1}^{n} \{((N/Q)_i - \langle N/Q \rangle)/\sigma_i\}^2}{n}$$

$$\text{Standard Deviation} \equiv \sigma = \sqrt{\frac{\sum_{i=1}^{n} ((N/Q)_i - \langle N/Q \rangle)^2}{n}}$$

i sum over all + or - runs

is shown in Table XI, as well as in Figs. 57 to 66. The value of $R = \langle N/Q \rangle^+ / \langle N/Q \rangle^-$ with its uncertainty is also given in Table XI and Figs. 57 to 66.

A breakdown of the fractional errors contributing to the uncertainty in R (errors $\epsilon_1, \epsilon_2, \epsilon_3, \epsilon_4, \epsilon_5, \epsilon_6, \epsilon_7$, and ϵ_8 of Section G, Chapter III) along with R and its total uncertainty is shown in Table XII.

For the points for which data was taken during both weeks of running, a final value of R was obtained by combining values of R obtained for each week.

To be consistent with the averaging method used to obtain the $\langle N/Q \rangle$'s, the R's were combined by weighting each R with the inverse of the square of the fractional statistical error, i.e.

$$\langle R \rangle = \frac{\frac{\langle R_{8/15} \rangle}{\epsilon_{8/15}^2} + \frac{\langle R_{9/6} \rangle}{\epsilon_{9/6}^2}}{\frac{1}{\epsilon_{8/15}^2} + \frac{1}{\epsilon_{9/6}^2}}$$

Where $\langle R_{8/15} \rangle$, $\langle R_{9/6} \rangle$ are the values of R obtained during the weeks of Aug. 15, 1967 and Sept. 6, 1967, respectively

and $\epsilon_{8/15}$, $\epsilon_{9/6}$ are the fractional statistical uncertainties for the R's above

WEEK of Data	E_o (GeV)	θ (o)	$\langle N/Q \rangle^+$	$\bar{\chi}^{2+}$	σ for e^+	$\langle N/Q \rangle^-$	$\bar{\chi}^{2-}$	σ for e^-	R
8/15	4.00	12.5	1.129±.020	.430	.016	1.138±.020	.075	.005	0.992±.022
9/6	4.00	12.5	1.163±.012	.424	.011	1.176±.014	.000	.000	0.989±.013
8/15	4.00	20.0	3.757±.104	.150	.047	3.856±.108	.157	.052	0.974±.036
9/6	4.00	20.0	3.887±.065	.067	.024	3.818±.065	.016	.011	1.018±.022
8/15	4.00	27.5	3.103±.245	.400	.217	3.240±.208	.370	.213	0.959±.096
9/6	4.00	27.5	3.380±.097	1.09	.224	3.206±.108	1.17	.242	1.054±.044
	4.00	35.0	4.898±.312	.515	.493	4.406±.381	1.52	1.25	1.111±.119
	10.0	2.6	9.081±.154	.262	.072	9.080±.127	.000	.001	1.001±.020
	10.0	5.0	1.587±.058	.000	.000	1.601±.042	.000	.000	0.992±.041
	10.0	12.5	3.453±.085	.210	.138	3.368±.076	1.17	.906	1.027±.032
	10.0	15.0	6.418±.259	.548	.505	6.275±.259	.697	.658	1.022±.058
INELASTIC DATA $N^*(1238)$	10.0	2.6	3.510±.051	.000	.000	3.458±.049	.664	.052	1.015±.020
	10.0	5.0	1.094±.040	.000	.000	1.087±.033	.000	.000	1.007±.048

TABLE XI: Table giving average N/Q's with mean χ^2 and the standard deviation.

Week of Data	E_0 [GeV]	θ [degrees]	N STATISTICS ϵ_1	BACKGND STATISTICS ϵ_2	ϵ_3			ELASTIC PEAK POSITION ϵ_4	BEAM STEERING ϵ_5	BEAM CHARGE MONITOR ϵ_6	INC. ENERGY ϵ_7	PION CONTAM. ϵ_8	$R = \frac{\sigma^+}{\sigma^-}$
					C_5 STATISTICS	C_4 STATISTICS	C_8 STATISTICS						
8/15	4	12.5	.672	.158	.046	.145	.153	.159	.347	2.02	.136	.000	0.992±.022
9/6	4	12.5	.484	.110	.032	.106	.140	.218	.347	1.03	.332	.000	0.989±.013
8/15	4	20.0	2.99	.501	.196	.622	.227	.189	.254	2.00	.230	.000	0.974±.036
9/6	4	20.0	1.74	.345	.089	.373	.128	.179	.254	1.04	.205	.000	1.018±.022
8/15	4	27.5	9.26	2.86	.811	2.04	.722	.635	.179	.730	.298	.000	0.959±.096
9/6	4	27.5	3.92	1.01	.215	.852	.382	.182	.179	1.08	.229	.000	1.054±.044
	4	35.0	9.58	3.21	.000	2.18	.612	.643	.133	1.50	.599	2.00	1.111±.119
	10	2.6	.982	.162	.098	.247	.308	.133	.541	1.50	.088	.000	1.001±.020
	10	5.0	2.96	1.65	.571	.712	1.38	.288	.438	1.50	.140	.000	0.992±.041
	10	12.5	2.99	.516	.211	.628	.115	.416	.182	.450	.239	.000	1.027±.032
	10	15.0	5.35	1.04	.321	1.19	.106	.324	.150	.510	.175	.000	1.022±.058
INELASTIC DATA N*(1238)	10	2.6	.927	.671	.218	.262	.345	.000	.528	1.50	.000	.000	1.015±.020
	10	5.0	2.92	3.12	.584	.722	.816	.000	.544	1.50	.000	.000	1.007±.048

TABLE XII: Breakdown of Errors and their % contribution to the uncertainty in R

B. Values of R

The final values of R obtained for each data point are shown in Table XIII and a comparison with previous measurements is given in Fig. 67.

In Table XIII, R is the corrected experimental ratio with its uncertainty. The uncertainty in R is the square root of the sum of the squares of the statistical uncertainty and the estimated uncertainty due to systematic errors, both of which are given in the table. As we indicated earlier, the systematic error is dominated by the beam monitor uncertainty.

The column labelled "Rad. Corr." is the net correction to R from radiative effects. The column labelled "ReB/A" in the table gives the 95% confidence limits for the quantity ReB/A defined in Chapter I.

The inelastic measurements in the table, labelled "N*(1238)," give R for all scattered events which correspond to a range of missing mass from $\sim$1110 MeV to $\sim$1370 MeV, for the final state particles other than the scattered electron. By subtracting the elastic radiative tail in this region, we estimate about 70% of the cross section leads to N*(1238) production. The remainder of the scattering in this region can be attributed to non-resonant pion production and to the radiative tail for elastic scattering. No radiative corrections were made to these cross sections.

As can be seen in the table, both our elastic and inelastic measurements are consistent with R=1.

TABLE XIII: ELASTIC SCATTERING DATA

Scattering Angle θ (degrees)	Incident Energy E_o (GeV)	q^2 $(GeV/c)^2$	$R = \frac{\sigma^+}{\sigma^-}$	Statistical Error	Systematic Error	Rad. Corr.	Limits on ReB/A	
							lower	Upper
12.5	4.00	0.689	0.990±.016	±.004	±.015	-.006	-.010	.005
20.0	4.00	1.535	1.006±.022	±.016	±.015	-.015	-.010	.013
27.5	4.00	2.440	1.039±.042	±.040	±.011	-.028	-.011	.031
35.0	4.00	3.268	1.111±.119	±.115	±.030	-.045	-.032	.087
2.6	10.00	0.204	1.001±.020	±.012	±.016	-.001	-.010	.010
5.0	10.00	0.731	0.992±.041	±.039	±.014	-.002	-.023	.019
12.5	10.00	3.785	1.027±.032	±.030	±.012	-.014	-.009	.023
15.0	10.00	4.999	1.022±.058	±.056	±.015	-.020	-.024	.035
INELASTIC DATA: REGION of N*(1238)								
2.6	10.00	0.197	1.015±.020	±.012	±.016	0.000	-.007	.014
5.0	10.00	0.705	1.007±.048	±.045	±.017	0.000	-.022	.026

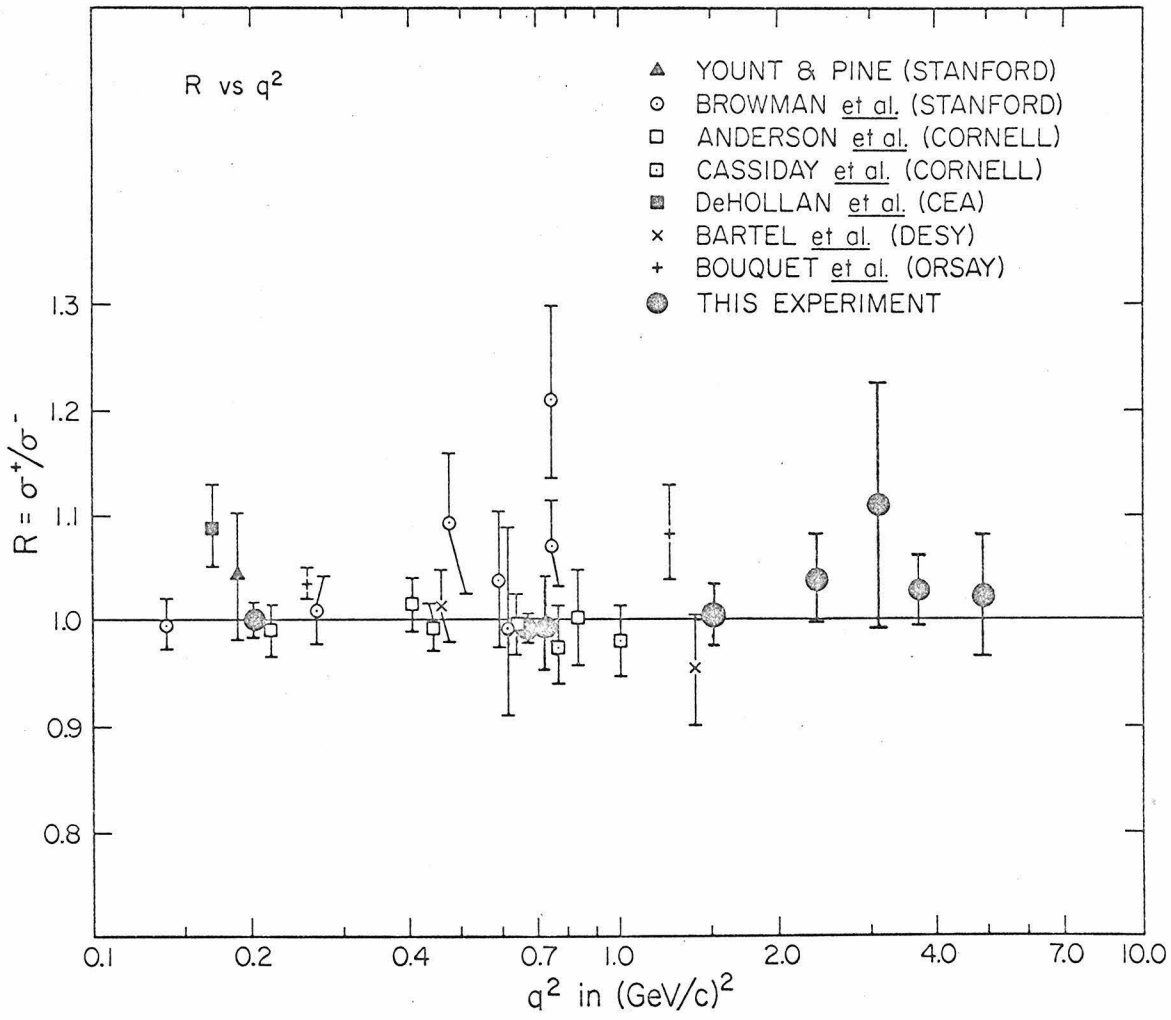

FIGURE 67:

The ratios R (from Ref. 2) of e^+p to e^-p elastic scattering cross sections are shown plotted against four-momentum transfer squared, q^2. The new results from this experiment are shown as solid points.

VI. INTERPRETATION of RESULTS

Within the one standard deviation errors, all the measurements taken in this experiment, both elastic and inelastic, are consistent with R=1. We found no evidence that two-photon terms contribute significantly to elastic or inelastic scattering over the kinematical region of our experiment. Our results are therefore consistent with the single-photon exchange model, on which the Rosenbluth formula is based.

The implications of our result, as far as various two-photon enhancement mechanisms are concerned, will now be considered. Because of the lack of theoretical studies relating to the two-photon contributions to inelastic scattering, we have restricted our considerations to elastic scattering only.

A. Possible N*(1238) Enhancement

Early estimates of a possible resonance enhancement of the form shown in Fig. 68 were made by Drell, Ruderman and Fubini[17]. They were motivated by the large nuclear Compton scattering cross section observed for photon frequencies near the (3/2,3/2) pion-nucleon resonance.

However, although the nucleon polarizability (dynamic two-photon contribution) was large, they found it had opposite signs above and below the resonance. Since in electron scattering the virtual photon is integrated over frequency and wave number, the net polarizability

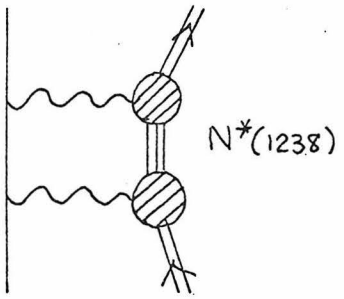

FIGURE 68: N*(1238) Enhancement of Two-Photon Amplitude

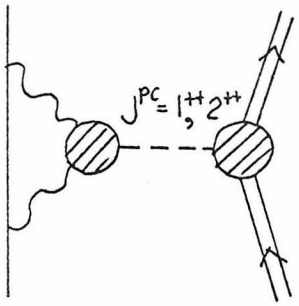

FIGURE 69: Meson Enhancement in the annihilation channel for two-photon amplitude

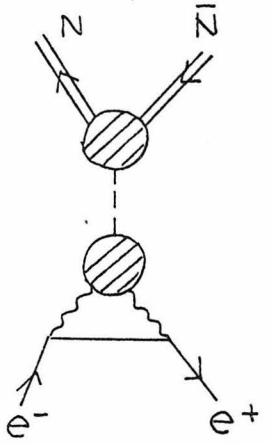

FIGURE 70: t-channel representation of Fig. 69

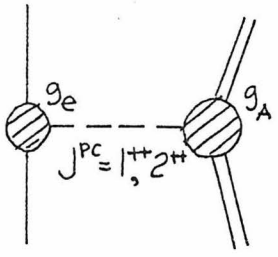

FIGURE 71: Direct Exchange Diagram to represent meson enhancement in the annihilation channel of the two-photon amplitude

correction to ep scattering turns out to be small. Drell, Ruderman and Fubini found the two-photon contribution to be less than 2% for all angles and energies up to 1 GeV. Werthamer and Ruderman extended this calculation and found the two-photon contribution to be small for nonforward scattering angles (for $\theta >> m_\pi/E_o$, or $\theta >> 2^o$ for E_o=4 GeV and $\theta >> 0.8^o$ at E_o=10 GeV) at all energies.

Because the uncertainty in our determinations of R were $\gtrsim \pm 1.6\%$, our results are consistent with the estimates above.

B. Possible $J^{PC}=1^{++}$, 2^{++} Enhancements

Resonant enhancements in the annihilation channel (see Fig. 69) have been considered by Gourdin, Martin, Flamm, Kummer, Drell and Sullivan[18].

By an helicity argument, one can show that in the high energy limit where the electron mass is negligible, the intermediate state particle in Fig. 69 cannot have zero spin. This can be seen intuitively if one remembers that the spin of a zero mass particle (e.g., a photon) is lined up parallel or antiparallel to its direction of motion. Conservation of angular momentum requires some angular momentum to be transferred across to the nucleon whenever the zero mass electrons scatter (i.e., change direction).

Since the smallest spin that can be transferred across is one, the spin of the intermediate state meson must be one of J=1,2,3,... Furthermore, since the charge conjugation (C) parity of a two photon state is positive, the C parity of the intermediate state must also

be positive.

The space inversion parity (P) can be found by transforming our scattering process in the s-channel to the t-channel (see Fig. 70). In this case, the incident and scattered nucleon appear as a nucleon-antinucleon pair. We can therefore use the well known C parity relation (which is a direct result of the generalized Pauli principle):

$$C = (-1)^{L+S}$$

Where:
C = C-parity
L = Total orbital angular momentum of the nucleon-antinucleon system
S = Total spin angular momentum of the nucleon-antinucleon system

If we consider the J=1 case, the possible L, S combinations are:

L	S
1	0
0	1
1	1
2	1

From the relation above, it is clear that only the L=1, S=1 state satisfies C>0. Since the spatial parity for L=1 is -1, the spin parity for two nucleons with S=1 is +1, and the intrinsic parity for a particle is opposite to that of its antiparticle, the total P-parity is P=-1(1)(-1)=+1>0.

If the spin of the intermediate particle is J=2, the possible L, S combinations are:

L	S
1	1
2	0
2	1
3	1

Only the L=1, S=1 and L=2, S=0 states satisfy C>0. Since the spatial parity for L=2 is +1 and the spin parity for S=0 is -1, again the total parity is positive.

Hence, if we limit our considerations to states with spin ≤ 2, the intermediate states must have quantum numbers $J^{PC} = 1^{++}$ or 2^{++}.

1. $J^{PC} = 1^{++}$ Resonance Enhancement

The effects of a $J^{PC} = 1^{++}$ intermediate state have been calculated by the authors mentioned earlier[18].

Gourdin and Martin applied a partial wave analysis to the t-channel diagram (Fig. 70) and obtained the following expression for the ep elastic scattering cross section in the laboratory:

$$\left(\frac{d\sigma}{d\Omega}\right)^{\pm}_{Lab} = \left(\frac{d\sigma}{d\Omega}\right)_{Mott} \cdot \left\{ A(q^2) + B(q^2)\tan^2\frac{\theta}{2} \pm C(q^2)\tan^2\frac{\theta}{2}\sqrt{1 + \frac{1}{1+\tau}\cot^2\frac{\theta}{2}} \right\}$$

Where: $q^2 = (p_o - p')^2$ = 4-momentum transfer squared

$\tau = (-q^2/4M^2) > 0$ for spacelike q^2

θ = electron scattering angle

M = proton rest mass

$(d\sigma/d\Omega)_{Mott}$ = Mott cross section, defined on p.1

\+ refers to $e^+p \to e^+P$

\- refers to $e^-p \to e^-p$

Flamm and Kummer, as well as Drell and Sullivan, have treated the $J^{PC} = 1^{++}$ case in a direct exchange model (see Fig. 71) using perturbation theory, and obtain the modified ep scattering cross section to be:

$$\left(\frac{d\sigma}{d\Omega}\right)^{\pm}_{Lab} = \left(\frac{d\sigma}{d\Omega}\right)_{Rosenbluth} \pm \left(\frac{d\sigma}{d\Omega}\right)_{Mott} \cdot \left(\frac{e^2 g_e g_A}{1 - m_r^2/q^2}\right) \frac{-q^2}{M^2} \sqrt{\frac{1+\tau}{\tau}}\, G_M(q^2) \tan^2\frac{\theta}{2} \sqrt{1 + \frac{\cot^2\theta/2}{1+\tau}}$$

Where: g_e = meson-electron coupling constant
g_A = meson-nucleon coupling constant
m_r = mass of the intermediate meson

$e^2 = \alpha = 1/137$

G_M, $(d\sigma/d\Omega)_{Rosenbluth}$, $(d\sigma/d\Omega)_{Mott}$ as defined on p.1

We have used the above relation with the Dipole fit to the form factors (cf. p.91) to fit our data and to obtain the 95% confidence limits to $g_e g_A$.

The 95% confidence limits obtained from our measurements and from earlier measurements of R, are given in Table XIV. The limits are given for three different resonance masses: 1070, 1285 and 1500 MeV. The first two masses correspond to the observed $J^{PC} = 1^{++}$ particles $A_1(1070)$ and D(1285).

Note that the limits set by this experiment are consistent with limits set by earlier experiments with the exception of the DeHollan and Browman experiments.

From these limits we have estimated the coupling constant $g_e g_A$ to be ~ 0.3, and have calculated R with the above expression in order to compare it with our measurements. The results are shown in Fig. 72

EXPERIMENT to MEASURE R	m_r=1.070 GeV		m_r=1.285 GeV		m_r=1.500 GeV	
	Lower Limit	Upper Limit	Lower Limit	Upper Limit	Lower Limit	Upper Limit
This Experiment	-.303	.495	-.334	.536	-.371	.584
Bouquet et al.	.235	1.91	.316	2.31	.412	2.79
Bartel et al.	-3.79	1.43	-4.55	1.72	-5.46	2.06
Anderson et al.	-7.76	3.66	-10.3	4.84	-13.2	6.24
DeHollan et al.	.525	8.27	.669	10.5	.839	13.2
Browman et al.	.872	3.96	1.10	5.01	1.38	6.26
Yount & Pine	-169	155	-240	222	-324	301

TABLE XIV.

95% Confidence Limits on $g_e g_A$ for a $J^{PC}=1^{++}$ Two-Photon Enhancement

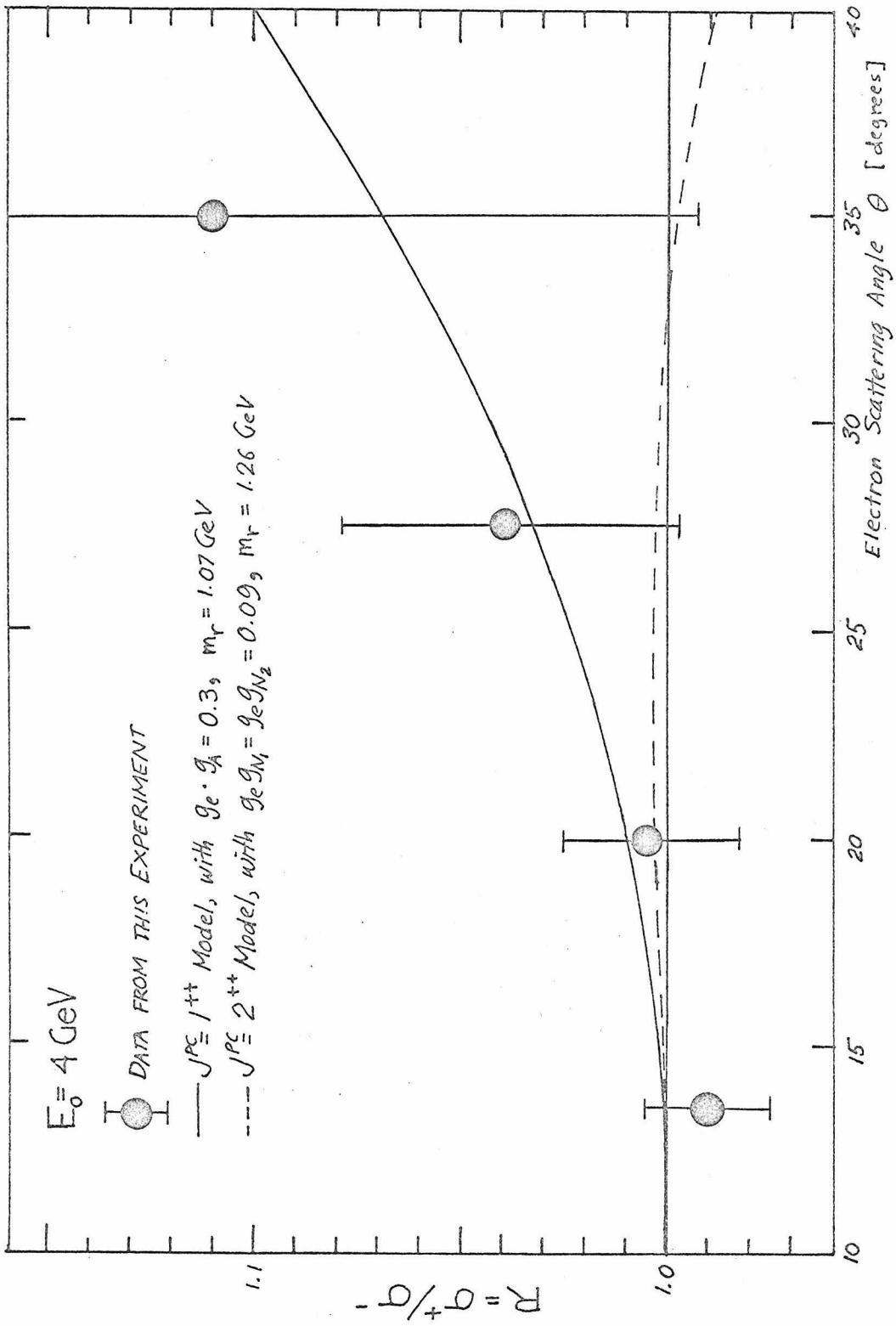

FIGURE 72: Comparison of Theoretical R's with Experimental R's

and Fig. 73. In all cases our measurements are consistent with the theoretical R's.

We mentioned earlier that a measurement of R is more sensitive to a deviation in the Rosenbluth formula than measuring the change in $a(q^2)+b(q^2)\tan^2(\theta/2)$ behavior. This is shown in the constant q^2 plots of $(d\sigma/d\Omega)^{\pm}_{Lab}/(d\sigma/d\Omega)_{Mott}$ v.s. $\tan^2(\theta/2)$: Figs. 74, 75 and 76. The plots correspond to the q^2 of our smallest angle, largest angle, and largest q^2 data points. Note that $(d\sigma/d\Omega)^{\pm}_{Lab}/(d\sigma/d\Omega)_{Mott}$ is very linear in the region of our measurements although the separation between the e^+p and e^-p curves is considerable. This very small change in curve shape is also apparent in Fig. 77, where $(d\sigma/d\Omega)^{\pm}_{Lab}/(d\sigma/d\Omega)$ v.s. θ at a constant E_o=10 GeV is plotted. Since the single photon curve sits between the e^+ and e^- curves in Fig. 77, it is clear that the shape changes very little.

2. $J^{PC}= 2^{++}$ Resonance Enhancement

Flamm and Kummer have also considered the case of a $J^{PC}= 2^{++}$ resonance in the annihilation channel. They assumed the following local coupling to the nucleon and electron, respectively:

$$\mathcal{H}_N = g_{N_1}\frac{1}{2}\left\{(\partial_\mu\bar{\psi}_N)(\partial_\nu\psi_N) + (\partial_\nu\bar{\psi}_N)(\partial_\mu\psi_\nu)\right\}B^{\mu\nu} + g_{N_2}\frac{i}{8}\left\{[\bar{\psi}_N\gamma_\mu,(\partial_\nu\psi_N)] - [(\partial_\nu\bar{\psi}_N),\gamma_\mu\psi_N] + (\mu\leftrightarrow\nu)\right\}B^{\mu\nu}$$

$$\mathcal{H}_e = e^4 g_e \frac{i}{8}\left\{[\bar{\psi}_e\gamma_\mu,(\partial_\nu\psi_e)] - [(\partial_\nu\bar{\psi}_e),\gamma_\mu\psi_e] + (\mu\leftrightarrow\nu)\right\}B^{\mu\nu}$$

Where: $\psi_N\ \psi_e$ = nucleon and electron field
$B^{\mu\nu}$ = propagator for $J^{PC}= 2^{++}$ particle
g_e = phenomelogical coupling constant of the electron to the 2^{++} particle

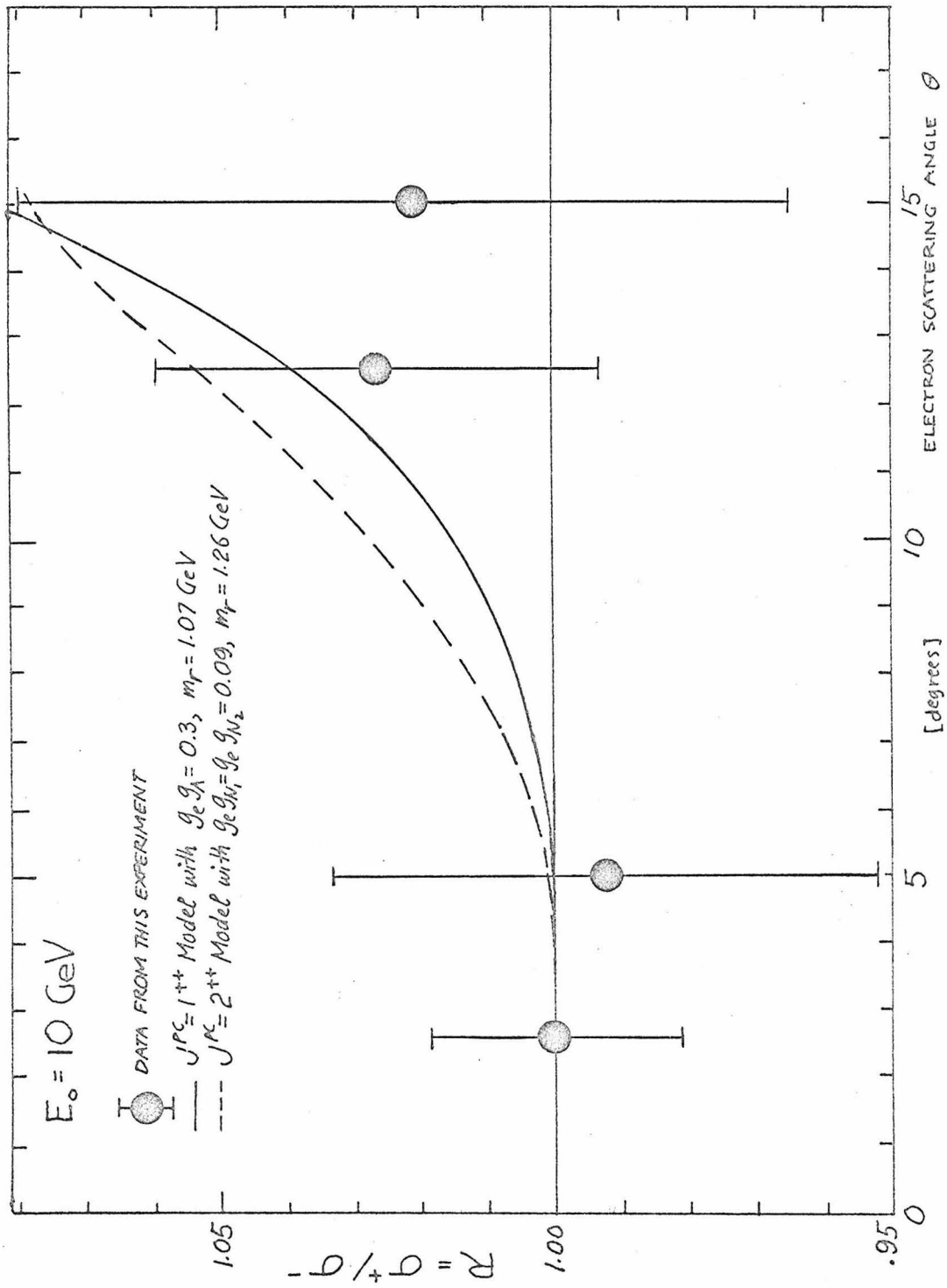

FIGURE 73: Comparison of Theoretical R's with Experimental R's

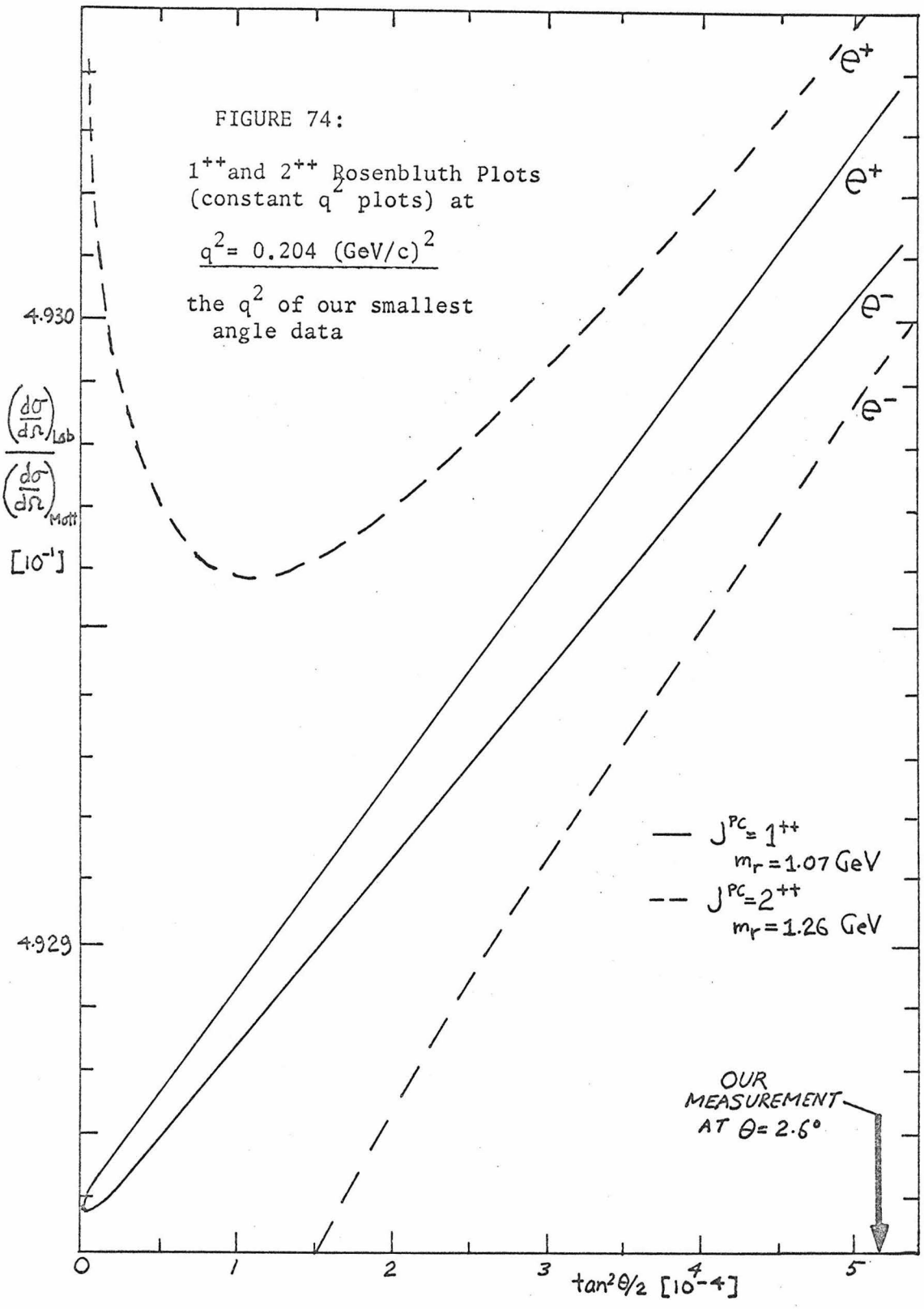

FIGURE 74:

1^{++} and 2^{++} Rosenbluth Plots (constant q^2 plots) at

$q^2 = 0.204$ $(GeV/c)^2$

the q^2 of our smallest angle data

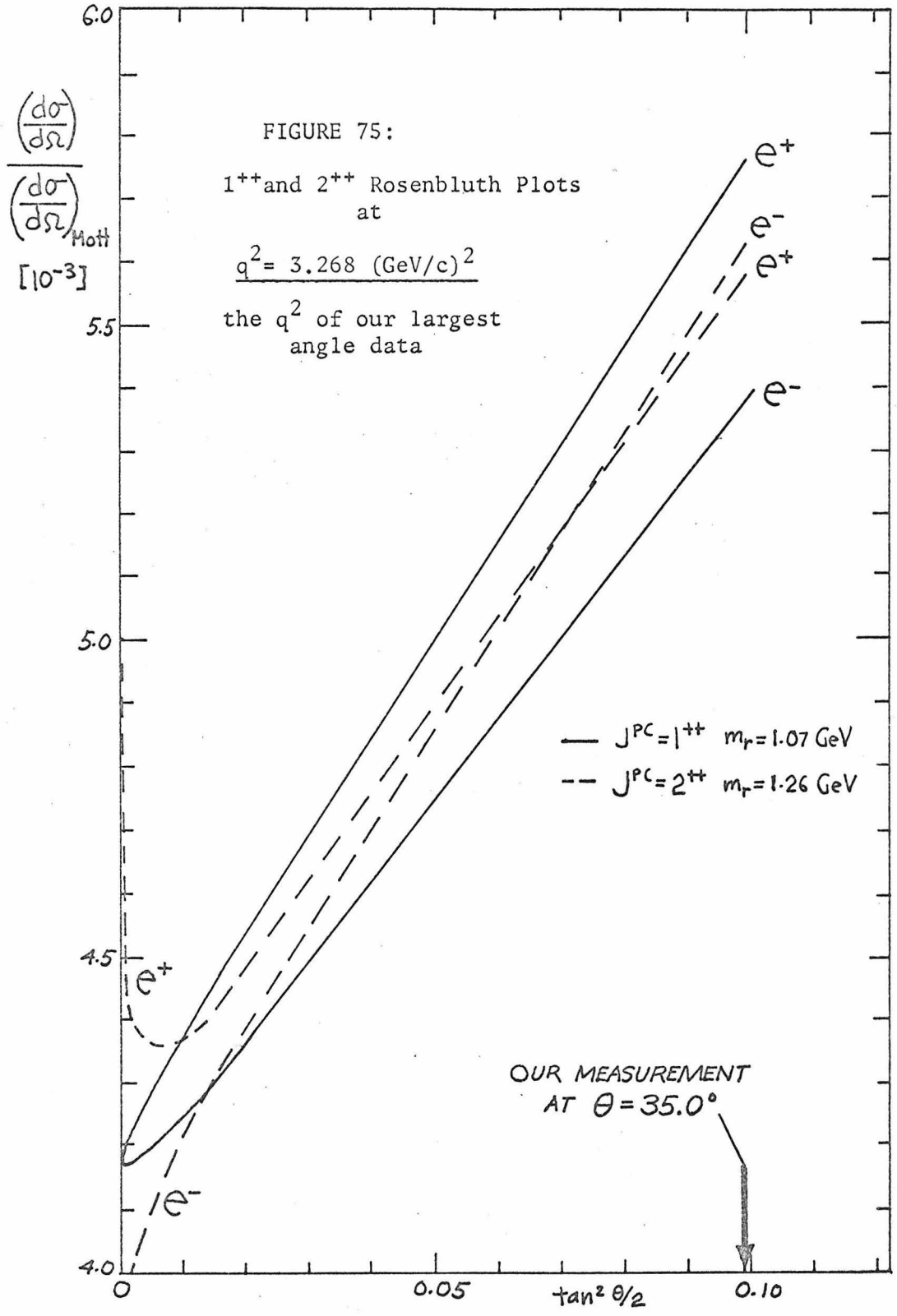
6.0
5.5
5.0
4.5
4.0
$\left(\frac{d\sigma}{d\Omega}\right) / \left(\frac{d\sigma}{d\Omega}\right)_{Mott}$
$[10^{-3}]$
FIGURE 75:
1^{++} and 2^{++} Rosenbluth Plots
at
$q^2 = 3.268\ (GeV/c)^2$
the q^2 of our largest angle data
e^+
e^-
e^+
e^-
$J^{PC}=1^{++}$ $m_r = 1.07$ GeV
$J^{PC}=2^{++}$ $m_r = 1.26$ GeV
e^+
e^-
OUR MEASUREMENT
AT $\theta = 35.0°$
0
0.05
$\tan^2 \theta/2$
0.10

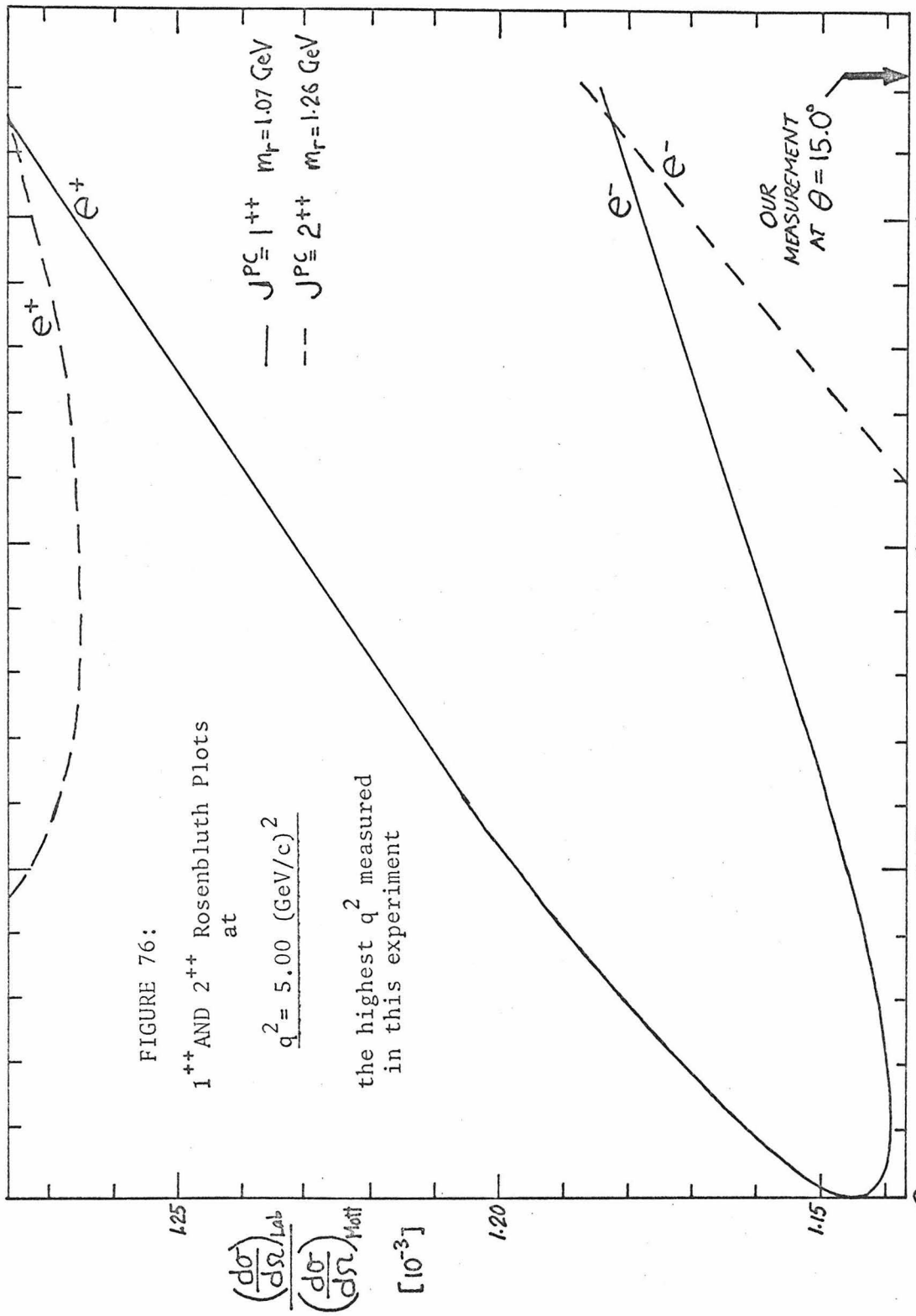

FIGURE 76:

1^{++} AND 2^{++} Rosenbluth Plots at

$q^2 = 5.00$ (GeV/c)^2

the highest q^2 measured in this experiment

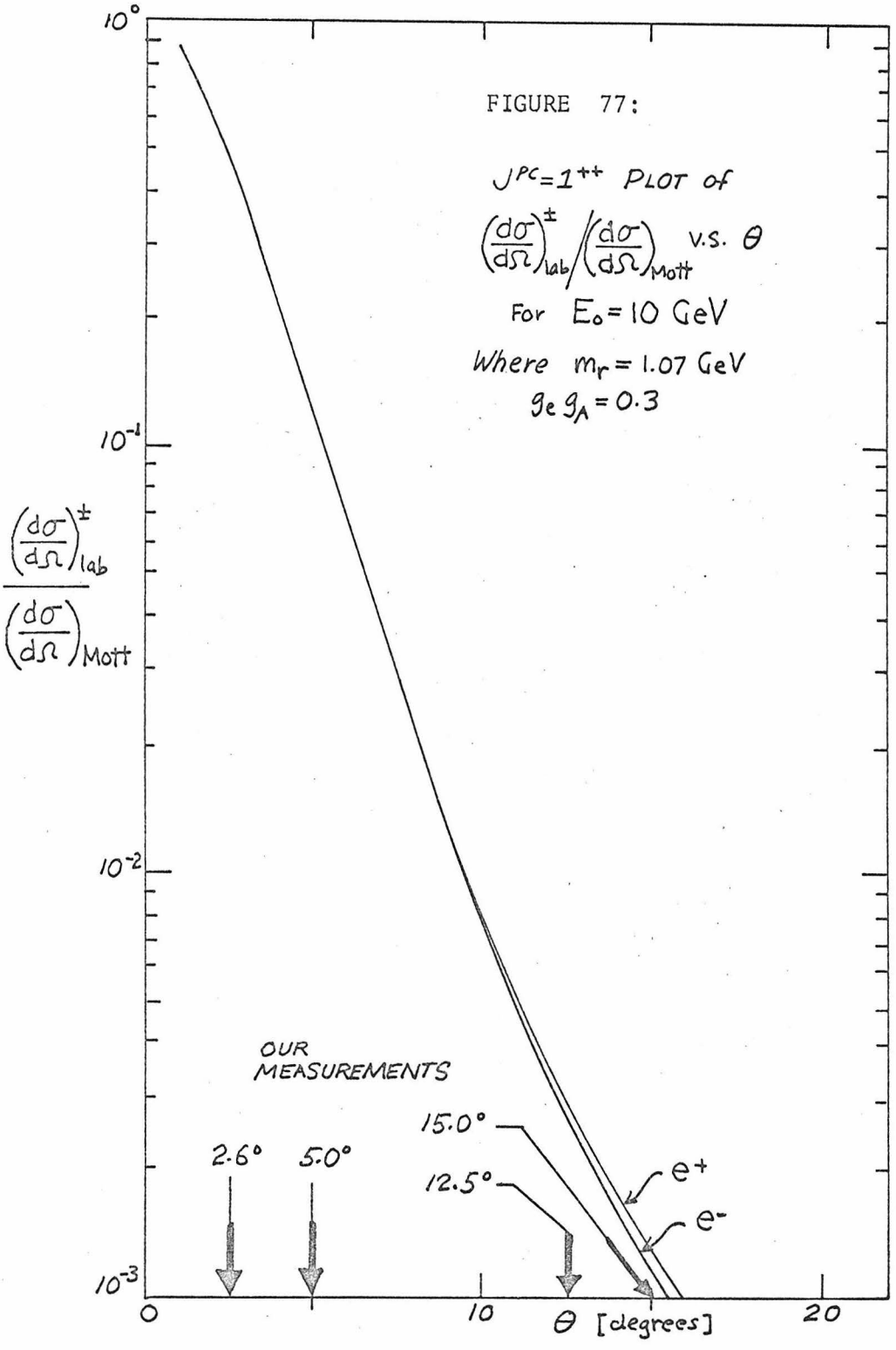
FIGURE 77:
$J^{PC}=1^{++}$ PLOT of
$\left(\frac{d\sigma}{d\Omega}\right)^{\pm}_{lab} \Big/ \left(\frac{d\sigma}{d\Omega}\right)_{Mott}$ v.s. θ
For $E_o = 10$ GeV
Where $m_r = 1.07$ GeV
$g_e g_A = 0.3$
$\frac{\left(\frac{d\sigma}{d\Omega}\right)^{\pm}_{lab}}{\left(\frac{d\sigma}{d\Omega}\right)_{Mott}}$
10^{0}
10^{-1}
10^{-2}
10^{-3}
OUR MEASUREMENTS
2.6°
5.0°
15.0°
12.5°
e^+
e^-
0
10
20
θ [degrees]

g_{N1}, g_{N2} = phenomelogical coupling constants of the nucleon to the 2^{++} particle

Two coupling constants are used to scale the strength of the two separate coupling terms for the meson-nucleon interaction. The two couplings are analogous to coupling to the charge and magnetic form factors in the one-photon case.

With the above interaction density, they obtained the following modified elastic ep scattering cross section in the lab:

$$\left(\frac{d\sigma}{d\Omega}\right)^{\pm}_{lab} = \left(\frac{d\sigma}{d\Omega}\right)_{Rosenbluth} \pm \left(\frac{d\sigma}{d\Omega}\right)_{Mott} \cdot \frac{e^2 g_e q^2}{4(1-m_r^2/q^2)} \sqrt{\frac{1+\tau}{\tau}} \sqrt{1+\frac{\cot^2\theta/2}{1+\tau}}$$

$$\times \left\{ 4M G_E g_{N_1} - g_{N_2}\left(G_M + F_1 + \frac{q^2}{M^2} G_M \tan^2\theta/2\right)\right\}$$

Where F_2, F_1 are the Dirac and Pauli form factors, which are related to G_E and G_M by:

$$F_1 = (G_M + G_E/\tau)/(1+1/\tau)$$

$$F_2 = (G_M - G_E)/(2M+2\tau)$$

Again we have used our data and previous measurements of R to obtain the 95% confidence limits to the coupling constants. However, because of the multiple coupling constants, the limits obtained are much less unique. We have treated the cases $g_{N1}=g_{N2}$, $g_{N2}=0$, and $g_{N1}=0$ with resonance masses 1260, 1305 and 1514 MeV, which correspond to the observed $J^{PC}= 2^{++}$ particles f(1260), A_2(1305) and f(1514). The results are shown in Table XV.

Note that our limits are not consistent with the limits obtained from Bouquet's, DeHollan's, and Browman's experiments. For Browman's experiment, the limits obtained with some of their data were inconsis-

EXPERIMENT to Measure R	m_r=1.260 GeV		m_r=1.305 GeV		m_r=1.514 GeV	
	Lower Limit	Upper Limit	Lower Limit	Upper Limit	Lower Limit	Upper Limit
ASSUMING $g_{N_1} = g_{N_2}$ Limits on $g_e g_{N_1} = g_e g_{N_2}$						
This Experiment	-.082	.119	-.084	.126	-.093	.165
Bouquet et al.	-7.28	-3.84	-7.58	-4.07	-9.10	.755
Bartel et al.	-.637	.873	-.673	.907	-.857	1.08
Anderson et al.	-1.41	.665	-1.49	.703	-1.90	.898
DeHollan et al.	.275	4.33	.289	4.55	.360	5.66
Browman et al.	4.95	2.95	5.20	3.15	6.44	4.15
Yount & Pine	-3.32	1.30	-3.55	1.39	-4.77	1.87
ASSUMING $g_{N_2} = 0$, Limits on $g_e g_{N_1}$						
This Experiment	-.030	.013	-.031	.013	-.034	.015
Bouquet et al.	$-5X10^8$	$-7X10^7$	$-5X10^8$	$-7X10^7$	$-6X10^8$	$-9X10^7$
Bartel et al.	-1.91	1.46	-.576	1.47	-.687	1.82
Anderson et al.	-1.54	3.27	-1.63	3.46	-2.08	1.21
DeHollan et al.	-5.82	-.370	-6.11	-.388	-7.61	-.483
Browman et al.	-13.0	-3.55	-13.8	-3.73	-17.9	-4.62
Yount & Pine	-50.6	131	-54.2	138	-72.7	186
ASSUMING $g_{N_2} = 0$, Limits on $g_e g_{N_2}$						
This Experiment	-.011	.026	-.015	.027	-.013	.030
Bouquet et al.	-7.28	-3.84	-7.58	-4.07	-9.10	-5.26
Bartel et al.	-.437	.339	-.462	.352	-.588	.420
Anderson et al.	-.985	.465	-1.04	.491	-1.33	.627
DeHollan et al.	.158	2.48	.166	2.61	.206	3.25
Browman et al.	2.07	2.58	2.17	2.76	2.69	3.64
Yount & Pine	-3.23	1.27	-3.47	1.36	-4.65	1.82

TABLE XV.

95% Confidence Limits on the Coupling Constants for a $J^{PC}=2^{++}$ Two-Photon Enhancement

tent with that obtained with the rest of their data. This is why their lower limits are greater than their upper limits in the table.

From our $g_{N_1}=g_{N_2}$ limits, we have estimated $g_e g_{N_1}=g_e g_{N_2}$ to be $\sim$0.09 and have compared the theoretical R calculated with the relation above with our measurements. The theoretical R was calculated using the Dipole fit to the nucleon form factors and by assuming a resonance mass of 1160 MeV. Our results, which are shown in Figs. 72 and 73, are again consistent.

As in the 1^{++} case, we have also made constant q^2 plots of $(d\sigma/d\Omega)^{\pm}_{Lab}/(d\sigma/d\Omega)_{Mott}$ v.s. $\tan^2(\theta/2)$ (see Figs. 74, 75 and 76). Again our measurements were made in the linear region of the $(d\sigma/d\Omega)^{\pm}_{Lab}/(d\sigma/d\Omega)_{Mott}$ curves. Note that both the deviation from linearity and the difference in $(d\sigma/d\Omega)^{+}_{Lab}/(d\sigma/d\Omega)_{Mott}$ and $(d\sigma/d\Omega)^{-}_{Lab}/(d\sigma/d\Omega)_{Mott}$ becomes very large at small angles, as one expects from the $\cot^2(\theta/2)$ term in the 2^{++} relation. However, at a constant incident energy, the difference in e^+ and e^- decreases to zero as we go to small angles (i.e. small q^2) as is shown in Fig. 78 where $(d\sigma/d\Omega)^{\pm}_{Lab}/(d\sigma/d\Omega)_{Mott}$ v.s. θ is plotted for E_o= 10 GeV.

C. Another Theoretical Estimate

Harte[19] has estimated the two-photon contribution to elastic scattering by applying their model for the NNγ (nucleon-photon vertex) vertex to the two-photon diagram.

Their model, which is based on a boot strap calculation, predicts the nucleon electromagnetic form factor to be in the form:

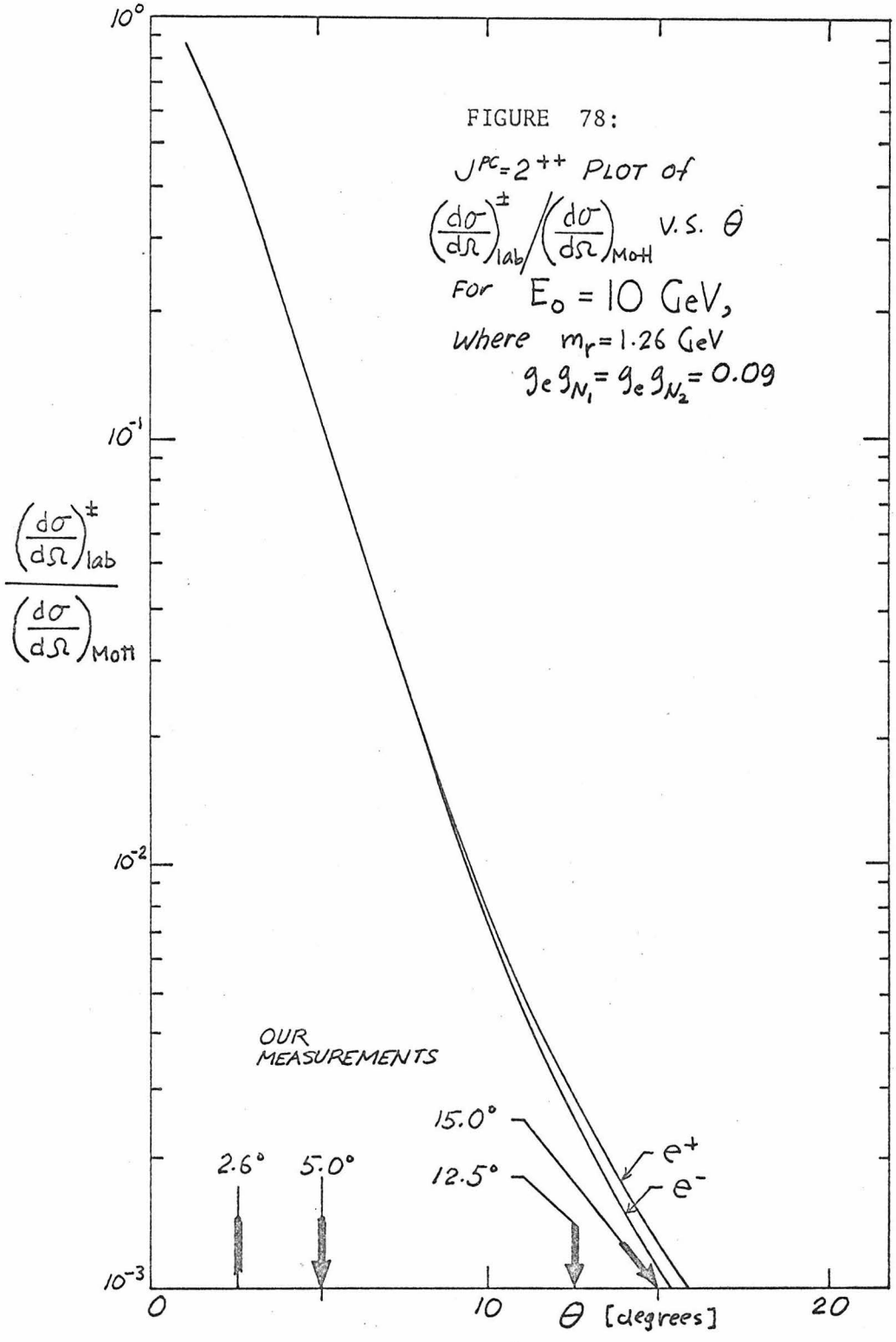

FIGURE 78:

$J^{PC} = 2^{++}$ PLOT of $\left(\frac{d\sigma}{d\Omega}\right)^{\pm}_{lab} \Big/ \left(\frac{d\sigma}{d\Omega}\right)_{Mott}$ V.S. θ FOR $E_0 = 10$ GeV, WHERE $m_f = 1.26$ GeV $g_e g_{N_1} = g_e g_{N_2} = 0.09$

$$G(q^2) \sim \exp(-b\sqrt{-q^2}) \qquad b = \text{constant}$$

They applied this vertex function to each of the two NNγ vertices in the two-photon diagram (see Fig. 79) and obtained the two-photon amplitude in the form:

$$A_2 \sim \alpha^2 \int d^4q' (\text{propagator and spin factors}) \cdot \exp(-b\sqrt{-q'^2(p-q')^2} - \sqrt{-(q-q')^2(p-q')^2})$$

$$\alpha = 1/137$$

They approximate this integral by considering only the case where $|q^2| \to \infty$ and obtain:

$$A_2 \sim \alpha^2 P_2(q^2) \qquad \text{Where } P_2(q^2) \text{ some polynomial or inverse of a polynomial}$$

Therefore, they predict the full scattering amplitude to be:

$$A_1 + A_2 \sim \alpha P_1(q^2)\exp(-b\sqrt{-q^2}) + \alpha^2 P_2(q^2)$$

$P_1(q^2)$=some polynomial or inverse of a polynomial

It is clear from the exponential fall off of the first order amplitude, that the two-photon term will dominate for large q^2.

They consider the simple case where $P_1(q^2)$=constant=c and obtained empirical fits to the parameters c and b by comparing their single photon exchange cross section with electron-proton scattering data. From this, they predict the magnetic form factor to be:

$$G_M^{\pm}(q^2) = |1.5\exp(-2.12\sqrt{-q^2}) \mp \alpha P_2(q^2)|$$

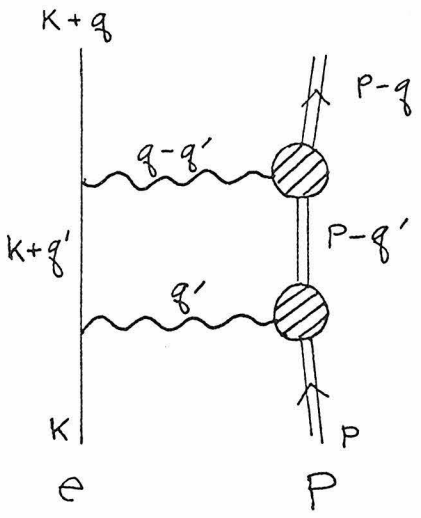

FIGURE 79:

Double vertex diagram used by Harte to calculate the two-photon amplitude

If $\alpha^2|P_2|^2 << |1.5\exp(-2.12\sqrt{-q^2})|^2$, then:

$$G_M^{\pm}(q^2) \simeq 1.5\exp(-2.12\sqrt{-q^2}) \mp \alpha \mathrm{Re}P_2$$

We have used this last relation to fit the experimental G_M's obtained from the recent elastic e^-p scattering data of Coward et al.[20] The values of $\mathrm{Re}P_2(q^2)$ obtained in this manner are shown in Column 3 of Table XVI.

Also shown in Table XVI are the 95% confidence limits of $\mathrm{Re}P_2$ obtained from our measurements of R, where we have used:

$$R = \frac{A_1^2 - 2\alpha A_1 \mathrm{Re}P_2 + \alpha^2|P_2|^2}{A_1^2 + 2\alpha A_1 \mathrm{Re}P_2 + \alpha^2|P_2|^2} \cong \frac{1 - 2A_1\alpha \mathrm{Re}P_2}{1 + 2A_1\alpha \mathrm{Re}P_2} \qquad \text{Where } A_1 = 1.5\exp(-2.12\sqrt{-q^2})$$

$$\text{or} \qquad \mathrm{Re}P_2 = \frac{A_1}{2\alpha}\left(\frac{1-R}{1+R}\right)$$

Note that, with the exception of the $q^2=2.44$ and 3.27 $(\mathrm{GeV}/c)^2$ points (where the accuracy of $\mathrm{Re}P_2$ from the experimental values of G_M was poor), our limits require $\mathrm{Re}P_2$ to be smaller than that obtained with the $G_M = |1.5\exp(-2.12\sqrt{-q^2}) + \alpha P_2|$ fit to the elastic e^-p data.

There is one other possibility, if we assume

$$G_M^{\pm} = |1.5\exp(-2.12\sqrt{-q^2}) \mp \alpha P_2(q^2)|$$

is correct. $P_2(q^2)$ may be very large but totally imaginary. Then the large $|P_2|^2$ term will enable a fit to the e^-p data and the $\mathrm{Re}P_2=0$ a fit to the R data. However, such a large imaginary two-photon contribution appears unlikely as previous measurements of the polariza-

Four Momentum Transfer Squared q^2 $(GeV/c)^2$	$G_M(q^2)$ From $e^-p \to e^-p$ Data of Coward et al.	$ReP_2(q^2)$ from G_M Values on Left	95% Confidence Limits on $ReP_2(q^2)$ from our values of R	
			Lower Limit	Upper Limit
0.690	0.264±.002	0.82±.28	-0.192	0.379
1.54	0.105±.001	0.28±.14	-0.181	0.144
2.44	$(0.540\pm.009)\times10^{-2}$	-0.82±1.24	-0.217	0.086
3.27	$(0.325\pm.013)\times10^{-1}$	-0.69±.89	-0.331	0.151
3.77	$(0.264\pm.002)\times10^{-1}$	1.23±.14	-0.072	0.031
5.00	$(0.160\pm.004)\times10^{-1}$	2.02±.24	-0.058	0.044

TABLE XVI.

Comparison of $ReP_2(q^2)$ deduced from e^-p scattering data and our R data

tion of the proton in e^-p elastic scattering (the proton polarization is proportional to the product of the imaginary part of the two-photon term and the one-photon term) at low q^2's ($\lesssim 1$ $(GeV/c)^2$) found the polarization to be less than 5%.

VII. APPENDICES

A. Energy Shift Due to Earth's Magnetic Field

Because of the long path length between the switchyard bending magnets and the energy defining slit (see Fig.8 - distance from magnets to slit was about 150 feet), it is necessary to consider the effect of the earth's magnetic field on the energy of the beam. This is especially important in a measurement of R, where any momentum shift due to the earth's field will be in opposite directions for electrons and positrons.

Let us first consider the worse case situation where no magnetic shielding is present.

The radius of curvature of a particle with charge e in a magnetic field H, is (in the units shown):

$$r_{[cm]} = \frac{10^4 P_{[GeV/c]}}{3 H_{[KGauss]}}$$

The angular deflection over a path length dl is:

$$d\theta = dl/r = 3 H dl / 10^4 P$$

or for a path of length S:

$$\theta = \int_S d\theta = \int \frac{3 H dl}{10^4}$$

Now:

$$H = H_{BSY} + H_N^e$$

Where:

H_{BSY} = switchyard bending field

H_N^e = normal component of earth's field

If we are using positrons and $H^{+}_{BSY} = |H_{BSY}|$, we obtain a deflection:

$$\theta_{+} = \int \left(\frac{3|H_{BSY}| + 3H_N^e}{10^4 P_{+}} \right) d\ell$$

If, when we use electrons, we take $H^{-}_{BSY} = -|H_{BSY}|$ (i.e., reverse the switchyard field), since the charge also changes sign, we obtain a deflection:

$$\theta_{-} = \int \left(\frac{3|H_{BSY}| - 3H_N^e}{10^4 P_{-}} \right) d\ell$$

To emerge through the momentum defining slits, both $\theta_{+} = \theta_{-} = \theta$.

Writing: $P_{+} = P + \Delta P$ and $P_{-} = P - \Delta P$, where $(P_{+} + P_{-})/2 = P$,

we get:

$$P_{+} = P + \Delta P = \int \frac{3|H_{BSY}|\,d\ell}{10^4\theta} + \int \frac{3H_N^e\,d\ell}{10^4\theta}$$

$$P_{-} = P - \Delta P = \int \frac{3|H_{BSY}|\,d\ell}{10^4\theta} - \int \frac{3H_N^e\,d\ell}{10^4\theta}$$

Therefore the relative fractional error in the beam momentum between e^{+} and e^{-} is:

$$\epsilon = \frac{2\Delta P}{P} = \frac{6}{10^4 \theta P} \int_S H_N^e\,d\ell$$

Now in the region of SLAC, $H^e = 0.514$ Gauss and the dip angle is 61.5°; therefore the vertical field is about 0.45 Gauss. The total angular deflection by the energy defining magnets in the switchyard is $12^{\circ} = 0.209$ radians, and the distance between the bending magnets and the energy slit is 150 feet; therefore we have $\epsilon = 5.90 \times 10^{-4} / P_{[GeV/c]}$. Thus, for our lowest energy beam (worse case - $E_o = 4$ GeV), $\epsilon = 0.0148\%$. This corresponds to a cross section change of 0.074% at $\theta = 12.5^{\circ}$.

Since this is extremely small and since magnetic shielding around the switchyard and the use of "earth's field cancelling" fixed current magnets should have decreased the effective earth's field by at least a factor of 10, we can neglect the energy asymmetry due to the earth's magnetic field.

B. Missing Mass Relation

The axis labelled "MISSING MASS" in Fig. 35 is the equivalent mass of the undetected final state particles if one assumes the detected particle has the mass of an electron.

The missing mass, MM, is easily determined from the 4-momentum conservation equation for the reaction:

$$p_o + P_p = p' + P_x$$

$p_o=(E_o,\vec{p}_o)$=inc. $e^{\pm}$ 4-mom.

$P_p=(M,\vec{0})$=initial proton 4-mom.

$p'=(E',\vec{p}')$=scattered $e^{\pm}$ 4-mom.

P_x=4-momentum of other final state particles

The missing mass is:

$$\begin{aligned} MM^2 = P_x^2 &= (p_o + P_p - p')^2 \\ &= (E_o + M - E')^2 - (\vec{p}_o - \vec{p}')^2 \\ &= E'^2 + E_o^2 + M^2 - 2(E'-E_o)M \\ &\quad -2E'E_o - \vec{p}'^2 - \vec{p}_o^2 + 2\vec{p}'\cdot\vec{p}_o \end{aligned}$$

In this experiment all incident and scattered electron momenta were high enough that $E_o>>m$, $E'>>m$ where m=electron rest mass. Therefore, $E_o=|\vec{p}_o|$ and $E'=|\vec{p}'|$, and using $E'^2-\vec{p}'^2=m^2$, $E_o^2-\vec{p}_o^2=m^2$ and $\vec{p}\cdot\vec{p}_o=|\vec{p}||\vec{p}_o|\cos\theta$ (where θ=electron scattering angle), we get:

$$MM^2 = M^2 + 2(E_o-|\vec{P}'|)M - 2|\vec{P}'|E_o(1-\cos\theta)$$

Hence, the missing mass, MM, was calculated by setting $|\vec{P}'|$ equal to the momentum of the detected particle and θ equal to the angle of the detected particle. E_o was supplied as a constant.

C. Bremsstrahlung

To explain our treatment of bremsstrahlung, let us first define the bremsstrahlung cross section:

$\frac{d\sigma}{dK} dK$ = The total cross section for an electron in the vicinity of an atom to emit a photon with energy in the range k-dk/2, k+dk/2

Thus if a flux I_i of electrons passes through a length L of given material (characterized by single atomic number Z), the probable number of electrons that will bremsstrahlung and emit a photon in the energy range k-dk/2, k+dk/2 will be:

$I_i \mathcal{N} L \frac{d\sigma}{dK} dK$ Where $\mathcal{N}$ = No. of atoms/unit vol.

We are interested in the number of elastic electrons which, by losing energy before or after scattering, will not appear in our hodoscope sample region R_s (cf. Fig. 27), because their momentum is below the lowest momentum accepted in R_s at that angle. If for a given scattering angle our sample region R_s accepts elastic electrons which have lost up to but not more than energy (or momentum) $\Delta E'$ (cf. Fig. 41), then we will not detect those elastic electrons that have lost more energy than $\Delta E'$ after scattering or $\Delta E_o = (E_o/E')^2 \Delta E'$ (where E_o, E' incident and scattered electron energy) before scattering. These are the only ones we will lose if we ignore the possiblity of an electron losing energy both before and after scattering. But since this occurs very rarely, we will ignore such "double bremsstrahlungs."

Thus the number of elastically scattered electrons we will lose by bremsstrahlung radiation will be:

$$N_{Brem_2} = \sum_{\substack{i \\ After}} \int_{\Delta E'}^{E'} \mathcal{N}_i L(i) \frac{d\sigma}{dk} dk \; N_{SCAT}$$

Where: E'=scattered electron momentum
N_{SCAT}=No. of scattered electrons
i =sum over each material with a different atomic number or density, that the scattered electrons pass through to reach the hodoscope
$L(i)$ =thickness of the ith material above
$\mathcal{N}_i$ =atomic density of the ith material above

Now:

$$N_{SCAT} = N_I' \left(\frac{d\sigma}{d\Omega}\right)_{ep} \Delta\Omega \, N_T \, \ell_T$$

Where:
N_I' =No. of incident electrons that have not lost energy $\geq \Delta E_o = (E_o/E')^2 \Delta E'$
$(d\sigma/d\Omega)_{ep}$ =elastic e^-p scattering cross section
$\Delta\Omega$ =solid angle acceptance into R_s
N_T =No. of protons/Vol. in the target
ℓ_T =Length of the target

Since: $N_I' = N_I - N_{Brem_1}$

where N_I =No. of incident electrons
N_{Brem_1}=No. of incident electrons that have lost energy $\geq \Delta E_o = (E_o/E')^2 \Delta E'$

and $N_{Brem_1} << N_I$

$$\therefore \quad N_{SCAT} \cong N_I \left(\frac{d\sigma}{d\Omega}\right)_{ep} \Delta\Omega \, N_T \ell_T$$

Hence we can write N_{Brem_2} as:

$$N_{Brem_2} = \left(\sum_{\substack{i \\ After}} \int_{\Delta E'}^{E'} \mathcal{N}_i L(i) \frac{d\sigma}{dk} dk \right) \left(\frac{d\sigma}{d\Omega}\right)_{ep} N_I \Delta\Omega \, N_T \ell_T$$

However, some of the electrons in N_{Brem_1} will elastically scatter in the target but will not be detected because of their initial

bremsstrahlung. The number of such lost elastic events is:

$$N'_{Brem_1} = N_{Brem_1}\left(\frac{d\sigma}{d\Omega}\right)_{ep}\Delta\Omega\, l_T N_T$$

$$= \left(\sum_{\substack{j \\ before}}\int_{\Delta E_o}^{E_o}\mathcal{N}_j L(j)\frac{d\sigma}{dk}dk\right)\left(\frac{d\sigma}{d\Omega}\right)_{ep} N_I \Delta\Omega N_T l_T$$

Where: j = sum over each material with a different atomic number or density that the electrons pass through before scattering

E_o = initial electron energy

Therefore, the total number of elastic events not detected because of bremsstrahlung losses is:

$$N_{Brem} = N_{Brem_2} + N'_{Brem_1}$$

$$= \left[\left(\sum_{\substack{j \\ After}}\int_{\Delta E'}^{E'}\mathcal{N}_j L(j)\frac{d\sigma}{dk}dk\right) - \left(\sum_{\substack{j \\ before}}\int_{\Delta E_o}^{E_o}\mathcal{N}_j L(j)\frac{d\sigma}{dk}dk\right)\right]\left(\frac{d\sigma}{d\Omega}\right)_{ep} N_I\Delta\Omega N_T l_T$$

Thus, whereas the elastic cross section, neglecting radiative losses, will predict the number of scattered events to be:

$$N_{SCAT} = \left(\frac{d\sigma}{d\Omega}\right)_{ep}\Delta\Omega\, l_T N_T N_I$$

this number will be reduced by bremsstrahlung losses to:

$$N_{SCAT} - N_{Brem} = \left(\frac{d\sigma}{d\Omega}\right)_{ep}\left(1+\delta_B\right)\Delta\Omega N_I N_T l_T$$

where:

$$\delta_B \equiv -\left(\sum_{\substack{j \\ After}}\int_{\Delta E'}^{E'}\mathcal{N}_j L(j)\frac{d\sigma}{dk}dk + \sum_{\substack{j \\ Before}}\int_{\Delta E_o}^{E_o}\mathcal{N}_j L(j)\frac{d\sigma}{dk}dk\right)$$

Since both incident and scattered electron energy are very high, we have used the Born approximation (Bethe Heitler formula) for the

bremsstrahlung cross section, with total screening[21].

$$\frac{d\sigma}{dk} = \frac{4Z^2 r_o^2}{137K}\left\{\left[1 + \left(\frac{E_2}{E_1}\right)^2 - \frac{2}{3}\left(\frac{E_2}{E_1}\right)\right]\log(183\,Z^{-1/3}) + \frac{1}{9}\frac{E_2}{E_1}\right\}$$

Where r_o = Classical electron radius = 2.82×10^{-13} cm
Z = Atomic No. of the material
E_1 = electron energy before bremsstrahlung
E_2 = electron energy after bremsstrahlung

The last term in the above equation is small compared to the first term so we will neglect it:

$$\frac{d\sigma}{dk} \cong \frac{4Z^2 r_o^2}{137K}\left[1 + \left(\frac{E_2}{E_1}\right)^2 - \frac{2}{3}\frac{E_2}{E_1}\right]\log(183Z^{-1/3})$$

From the expression for δ_B above, we will be multiplying this expression by factors like $\mathcal{N}_i$ and $L(i)$. If we measure $L(i)$ in units of X_o, where:

$$X_o \equiv \frac{1}{\mathcal{N}4Z^2 r_o^2 \log(183Z^{-1/3})/137} \equiv 1 \text{ Radiation Length}$$

$\mathcal{N}$ = atomic density

then we can eliminate the i and j sums in δ_B and write:

$$\sum_{i\ \text{After}} \int_{\Delta E'}^{E'} \mathcal{N}_i L(i)\frac{d\sigma}{dk}\,dk = L_A \int_{\Delta E'}^{E'} \left[1 + \left(\frac{E'-k}{E'}\right)^2 - \frac{2}{3}\left(\frac{E'-k}{E'}\right)\right]\frac{dk}{k}$$

where L_A = Total number of radiation lengths of material the scattered electrons pass through before reaching the hodoscopes

and similarly:

$$\sum_{j\ \text{Before}} \int_{\Delta E_o}^{E_o} \mathcal{N}_j L(j)\frac{d\sigma}{dk}\,dk = L_B \int_{\Delta E_o}^{E_o} \left[1 + \left(\frac{E_o-k}{E_o}\right)^2 - \frac{2}{3}\left(\frac{E_o-k}{E_o}\right)\right]\frac{dk}{k}$$

where L_B = Total number of radiation lengths of material the incident electrons pass through before scattering

If one evaluates these simple integrals and uses the approximations $\Delta E_o << E_o$, $\Delta E' << E'$, one obtains:

$$\delta_{Brem} = -\frac{4}{3}\left\{ L_A \left[\log\left(\frac{E'}{\Delta E'}\right) - 0.625 \right] - L_B \left[\log\left(\frac{E'^2}{E_o \Delta E'}\right) - 0.625 \right] \right\}$$

which is the relation given in Section E1 in Chapter III.

D. Relative Solid Angle

The relative solid angle seen by an elastic peak $p=p(\theta)$ in the 8-GeV/c hodoscope is:

$$\langle \Delta\Omega \rangle = \int_{\theta_1}^{\theta_2} d\theta \,(59 - 0.47\vartheta^2)(1 - 0.04\,\delta(P(\theta))^2)$$

θ_1, θ_2 is the angular region covered by the hodoscope

Let us convert ϑ and δ to θ-bins (T) and p-bins (P):

$$\vartheta = \frac{15.6}{54}(T-27) = 0.289\,\tau$$

where $\tau \equiv T - 27$

$$d\theta = d\vartheta = 0.289\,d\tau$$

$$\delta(P(\theta)) = 0.1\,(P(T) - 20)$$

$$= 0.1\left[P_e + \frac{dP}{dT}(T-27) - 20\right] = 0.1\left(P_e - 20 + \frac{dP}{dT}\tau\right)$$

where $P_e \equiv$ P at center of hodoscope (i.e. at T=27)

Therefore if we integrate over the full θ range of the θ-p plane (i.e., over the range $-27 \leq \tau \leq 27$), then calling:

$$a_0 = 0.289$$
$$a_1 = 59$$
$$a_2 = 0.0392$$
$$a_3 = 0.0004$$

we get:

$$\langle \Delta\Omega \rangle = a_0 \int_{-27}^{27} d\tau\,(a_1 - a_2\tau^2)\left[1 - a_3\left(P_e - 20 + \frac{dP}{dT}\tau\right)^2\right]$$

$$= a_0 \int_{-27}^{27} d\tau\left(b_0 + b_1\tau + b_2\tau^2 + b_3\tau^3 + b_4\tau^4\right)$$

where:

$$b_0 = a_1(1 - a_3(P_e - 20)^2)$$
$$b_1 = -2a_1a_3(P_e - 20)\,dP/dT$$
$$b_2 = -a_1a_3(dP/dT)^2 - a_2(1 - a_3(P_e - 20)^2)$$

$$b_3 = 2a_2a_3(P_e-20)\,dP/dT$$
$$b_4 = a_2a_3(dP/dT)^2$$

Therefore:

$$\langle \Delta\Omega \rangle = 54 a_0 \left(b_0 + \frac{b_2}{3} 27^2 + b_4 \frac{27^4}{5} \right)$$

Now the relevant quantity for us is not $\langle \Delta\Omega \rangle$ but $d\langle \Delta\Omega \rangle / dP_e$, i.e., the change in solid angle for a small change in the elastic peak position.

$$\frac{db_0}{dP_e} = -2a_1a_3(P_e-20), \qquad \frac{db_2}{dP_e} = 2a_2a_3(P_e-20),$$
$$\frac{db_4}{dP_e} = 0$$

$$\therefore \quad \frac{d\langle \Delta\Omega \rangle}{dP_e} = 2 \times 54 (P_e-20) a_3 (243a_2 - a_1) a_0$$

Now consider:

$$\xi = \left(\int_{\theta_1}^{\theta_2} d\theta \, (59 - 0.47\vartheta^2) \right) \left[\frac{d(1 - 0.04\,\delta(P)^2)}{dP} \right]_{P=P_e}$$

in our other notation:

$$\int_{\theta_1}^{\theta_2} d\theta \, (59 - 0.47\vartheta^2) = a_0 \int_{-27}^{27} d\tau \, (a_1 - a_2\tau^2) = 54 a_0 (a_1 - 243 a_2)$$

and:

$$\left[\frac{d\,(1 - 0.04\,\delta^2(P))}{dP} \right]_{P=P_e} = \left[\frac{d\,(1 - a_3(P-20)^2)}{dP} \right]_{P=P_e}$$
$$- 2a_3(P_e-20)$$

Therefore:

$$\frac{d\langle \Delta\Omega \rangle}{dP} = \xi = \left(\int_{\theta_1}^{\theta_2} d\theta \, (59 - 0.47\vartheta(\theta)^2) \right) \left[\frac{d\,(1-0.04\,\delta^2(P))}{dP} \right]_{P=P_e}$$

E. Deadtime Losses

1. Deadtime Losses in EVTT Scaler

Let the resolving time of the EVTT scaler be τ. Then if the events are distributed timewise in a Poisson distribution, we can write:

$$\text{Probability of } m \text{ events occuring in time } \tau = P(m) = \frac{a^m e^{-a}}{m!}$$

where a = average No. of events in time τ

Note that the probability of 1 or more events occuring in time τ is: $P(\geq 1) = \frac{ae^{-a}}{1!} + \frac{a^2e^{-a}}{2!} + \ldots = 1 - e^{-a} \cong a$ if $P(\geq 1) \ll 1$

i.e.,

$$a \cong P(1) \quad \text{if } P(\geq 1) \ll 1$$

Now since only one event will be counted in EVTT whenever 1, 2, 3, ... events occur in time τ, the total number of events counted per beam pulse is:

$$EVTT = (T_\ell/\tau)(P(1)+P(2)+P(3)+\ldots) \simeq T_\ell P(1)/\tau$$

Where T_ℓ = pulse length of beam
τ = resolving time (i.e. deadtime) of EVTT scaler

And the number of events lost during a beam pulse is:

$$\begin{aligned} EVTT_{lost} &= (T_\ell/\tau)(2P(2)+3P(3)+\ldots - P(2)-P(3)-\ldots) \\ &= (T_\ell/\tau)P(2) = (T_\ell/\tau)a^2e^{-a}/2 = (T_\ell/\tau)P(1)a/2 \\ &= (T_\ell/\tau)P(1)^2/2 = EVTT/(T_\ell/\tau) \end{aligned}$$

Therefore the actual number of events that reached the input of the EVTT scaler per beam pulse was:

$$EVTT_{actual} = EVTT + EVTT_{lost} = EVTT\left(1 + \frac{EVTT}{2T_\ell/\tau}\right)$$

If we take EVTT as the total number of events applied to the input of the EVTT scaler during the whole run, then:

$$EVTT_{actual} = EVTT\left(1 + \frac{EVTT}{2N_p T_\ell/\tau}\right)$$

Where:
N_p = Total No. of beam pulses during the run

Therefore the fractional error in the EVTT scaler due to deadtime losses is:

$$\frac{EVTT_{actual} - EVTT}{EVTT} = \frac{EVTT}{2N_p T_\ell/\tau}$$

2. Estimating the Deadtime Loss in the Toggle

This is exactly analogous to the above case, differing only in that the sample period $N_p T_\ell/\tau$ is replaced by N_p.

i.e., If probability of m events in a beam pulse is:

$$P(m) = \frac{b^m e^{-b}}{m!}$$

where b = average No. of events per beam pulse

then: $b \simeq P(1)$

$NRD = N_p P(\geq 1) \simeq N_p P(1)$ If each beam pulse is equivalent*

$NLOST \simeq N_p P(2) = N_p P(1)^2/2 \simeq NRD/2N_p$

Therefore:

$$NACTUAL = NRD + NLOST = NRD\left(1 + \frac{NRD}{2N_p}\right)$$

and thus:

$$CC_8 = \left(1 + \frac{NRD}{2N_p}\right)$$

---

* If the beam pulse intensity changed from pulse to pulse then we would require a different "b" in the Poisson distributions for each pulse.

INCIDENT ENERGY E_o (GeV)	SCATTERING ANGLE θ (degrees)	Typical CC_8	Typical C_8
4	12.5	1.0570	1.0621
4	20.0	1.0035	1.0092
4	27.5	1.0005	1.0184
4	35.0	1.0004	1.0189
10	2.6	1.1050	1.1176
10	5.0	1.0230	1.0230
10	12.5	1.0012	1.0077
10	15.0	1.0016	1.0096

TABLE XVII.

Comparison of C_8=EVTT/NRD with CC_8=1 + NRD/2N_p, for Typical Runs. Both CC_8 and C_8 were taken from the same runs.

F. Calculating Elastic Peak Position from E_o, θ, NMR

We begin by deriving a useful relation.

In this experiment, electrons (positrons) scatter off a stationary proton target, i.e.,

$$p_o + P_p = p' + P_p'$$

p_o,p' initial and final electron 4-momentum
P_p,P_p' initial and final proton 4-momentum

can be written in 4-vector notation as:

$$\begin{pmatrix} E_o \\ p_o \\ 0 \\ 0 \end{pmatrix} + \begin{pmatrix} M \\ 0 \\ 0 \\ 0 \end{pmatrix} = \begin{pmatrix} E' \\ p_1' \\ p_2' \\ 0 \end{pmatrix} + \begin{pmatrix} E_p' \\ p^p \\ P \\ 0 \end{pmatrix}$$

Therefore:

$$\begin{aligned} M^2 &= E_p'^2 - \vec{P}_p'^2 = (E_o+M-E')^2 - (p_o-p_1')^2 - p_2'^2 \\ &= E_o^2 + E'^2 + M^2 + 2E_oM - 2ME' - 2E_oE' - (p_o^2 - 2p_o \cdot p_1' + p'^2) \\ &= 2m^2 + M^2 + 2(p_o \cdot p_1' + (E_o - E')M - E_oE') \end{aligned}$$

Since $m \ll E_o, E'$ we can neglect it, thus:

$$E' \simeq |\vec{p}'| \quad \text{and} \quad |\vec{p_o}| \simeq E_o$$

$$\text{and } \vec{p_o} \cdot \vec{p}'_1 = |\vec{p_o}||\vec{p}'|\cos\theta = E_o|\vec{p}'|\cos\theta$$

Therefore: $$E_o|\vec{p}'|(\cos\theta - 1) + (E_o - |\vec{p}'|)M = 0$$

or

$$|\vec{p}'| = \frac{E_oM}{M + E_o(1-\cos\theta)}$$

We are interested in calculating the relative change of the elastic peak position in the θ-p hodoscope plane - in particular, the p change at a given angle. Changes in the peak position will result from genuine momentum changes (e.g., due to changes in incident energy, E_o, or spectrometer angle, θ) or because of a change in the spectrometer magnetic fields.

When talking of the magnetic fields, we will concern ourselves strictly with the two bending magnets B81 and B82 in the 8-GeV/c spectrometer (see Fig. 80), as field measurements were not taken when the 20-GeV/c spectrometer was used.

Thus if we define p' as the apparent elastic momentum measured in the p-hodoscope for a fixed θ-bin, then:

$$\Delta p' = \frac{\partial P'}{\partial E_o}\Delta E_o + \frac{\partial P'}{\partial \theta}\Delta\theta + \frac{\partial P'}{\partial B_1}\Delta B_1 + \frac{\partial P'}{\partial B_2}\Delta B_2$$

B_1, B_2 magnetic fields in B81 and B82, respectively

Using the $|\vec{p'}|$ expression calculated earlier (and using notation $p' \equiv |\vec{p'}|$):

$$\frac{\partial P'}{\partial E_o} = \frac{\partial}{\partial E_o}\left[\frac{E_o M}{M + E_o(1-\cos\theta)}\right] = \left(\frac{P'}{E_o}\right)^2$$

$$\frac{\partial P'}{\partial \theta} = \frac{\partial}{\partial \theta}\left[\frac{E_o M}{M + E_o(1-\cos\theta)}\right] = -\frac{P'^2}{M}\sin^2\theta$$

If we had only one bending magnet, B, then $\partial p'/\partial B$ can be calculated very simply, since $p' \propto 1/\text{deflection} \propto 1/B$. Therefore:

$$p' = k/B \quad \text{or} \quad \frac{\partial p'}{\partial B} = -k/B^2 = -p'/B \qquad k = \text{constant}$$

However, we have two magnets, each at a different distance from the p-focal plane (see Fig. 80). Since a deflection in B81 will appear 13.42/8.87 times as large in the p-hodoscope as would a deflection in B82, we have weighted $\partial p'/\partial B_1$ and $\partial p'/\partial B_2$ accordingly,

i.e.

$$\frac{\partial P'}{\partial B_1} = \left(\frac{-13.42}{8.87+13.42}\right)\frac{P'}{B_1} = -0.602\,\frac{P'}{B_1}$$

$$\frac{\partial P'}{\partial B_2} = \left(\frac{-8.87}{8.87+13.42}\right)\frac{P'}{B_2} = -0.398\,\frac{P'}{B_2}$$

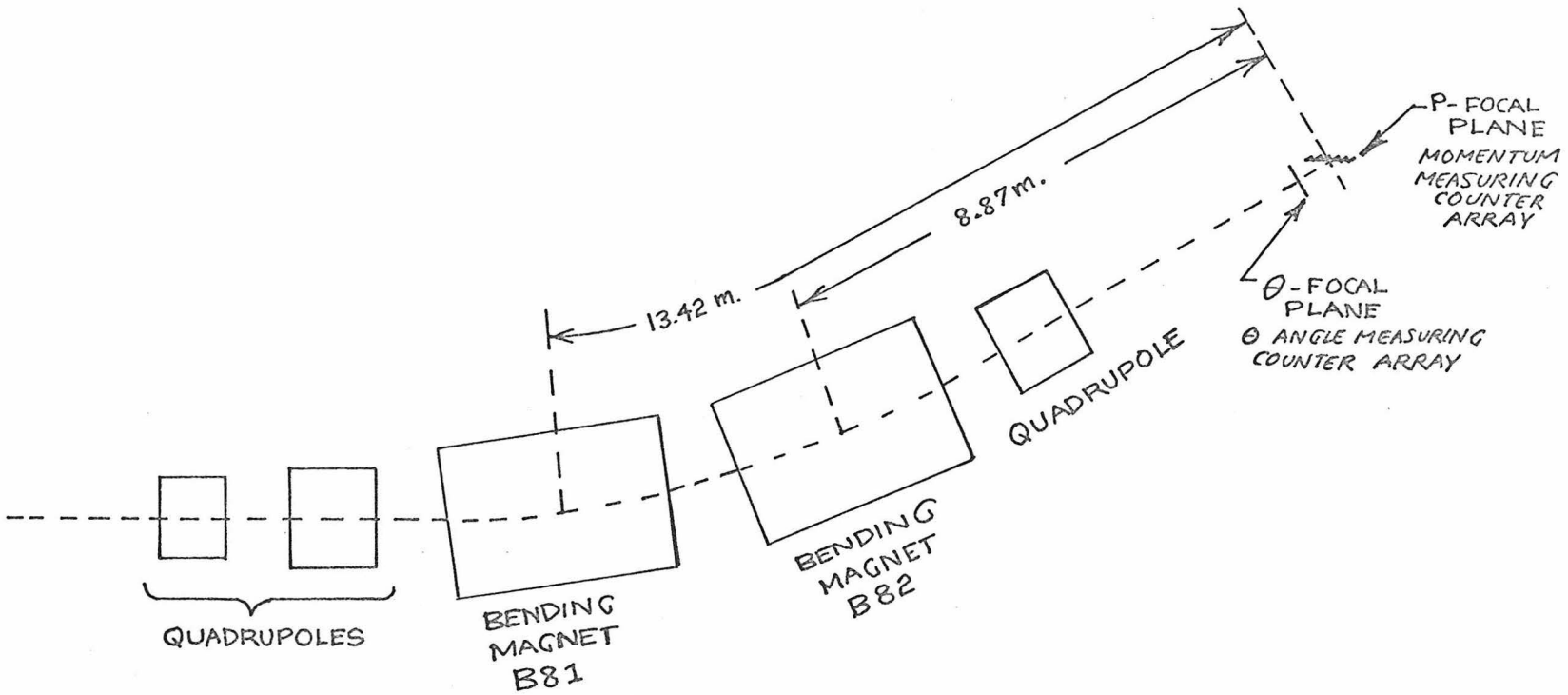

FIGURE 80:

Magnet Positions in the 8-GeV/c Spectrometer

Hence: $$(\Delta P')_{\substack{\text{Due to}\\ \text{Spec.}\\ \text{Fields}}} = \frac{\partial P'}{\partial B_1}\Delta B_1 + \frac{\partial P'}{\partial B_2}\Delta B_2 = -\left(0.602\,\frac{P'}{B_1}\Delta B_1 + 0.398\,\frac{P'}{B_2}\Delta B_2\right)$$

since $B_1 = f_1 k_1$ and $B_2 = f_2 k_2$

k_1, k_2 constants
f_1, f_2 resonant frequencies in the NMR probes located in B81 and B82

We can also write:

$$(\Delta P')_{\substack{\text{Due to}\\ \text{Spec. Fields}}} = -P'\left(0.602\,\frac{\Delta f_1}{f_1} + 0.398\,\frac{\Delta f_2}{f_2}\right)$$

Therefore the total shift in the apparent elastic peak should be:

$$\Delta P' = \left(\frac{P'}{E_o}\right)^2 \Delta E_o - \left(\frac{P'^2}{M}\sin^2\theta\right)\Delta\theta - P'\left(0.602\,\frac{\Delta f_1}{f_1} + 0.398\,\frac{\Delta f_2}{f_2}\right)$$

Since p', E_o, θ, ΔE_o, $\Delta\theta$, f_1, f_2, Δf_1, Δf_2 are all quantities that were measured for each run, the $\Delta p'$ between runs could be calculated.

G. Theoretical Elastic Radiative Tail

To understand our method of generating the radiative tail, let us suppose our incident electron beam has an extremely sharp energy spectrum - so sharp, that were it not for radiative corrections, the elastic peak would appear as a delta function in a fixed angle p-distribution plot. The radiative corrections will degrade such a peak by taking events from the peak and distributing them at lower momenta (see Fig. 81).

Now if our experimental apparatus will accept all events a distance ΔE_1 below the peak (see Fig. 81), then the number of events we will get is (cf. Section E1, Chapter III):

$$(N/Q)_1 = \left(\frac{d\sigma}{d\Omega}\right) e^{-\delta(\Delta E_1)} \left(\Delta\Omega\, I;\, N_T L_T\right)$$

$\left(\Delta\Omega\, I;\, N_T L_T\right)$ ← solid angle & target factors

δ = intrinsic & bremsstrahlung radiative correction

If we increase the acceptance to ΔE_2, then the number of events will be:

$$(N/Q)_2 = \left(\frac{d\sigma}{d\Omega}\right) e^{-\delta(\Delta E_2)} \left(\Delta\Omega\, I;\, N_T L_T\right)$$

Therefore, the number of events in the region between p_1 and p_2 in Fig. 81 is:

$$(N/Q)_{12} = (N/Q)_2 - (N/Q)_1 = \left(\frac{d\sigma}{d\Omega}\right)\left(\Delta\Omega\, I;\, N_T L_T\right)\left(e^{-\delta(\Delta E_2)} - e^{-\delta(\Delta E_1)}\right)$$

$$= \text{Constant} \cdot \left(e^{-\delta(\Delta E_2)} - e^{-\delta(\Delta E_1)}\right)$$

Constant ↑ for a given measurement

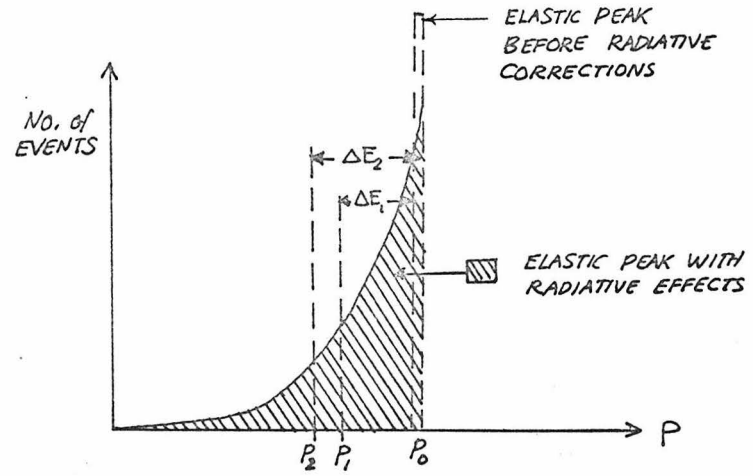

FIGURE 81: Radiative Tail from δ-Function Elastic Peak

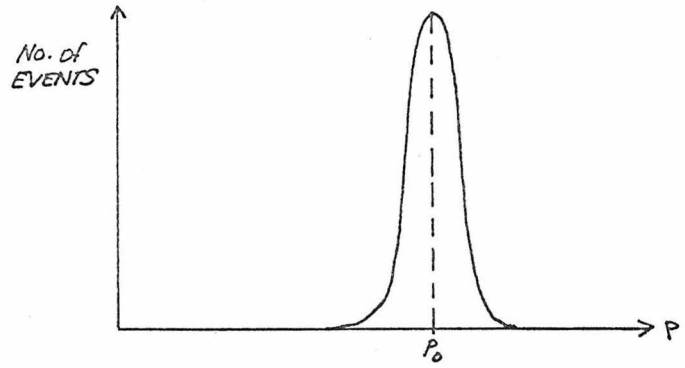

FIGURE 82: Actual Elastic Peak without radiative effects

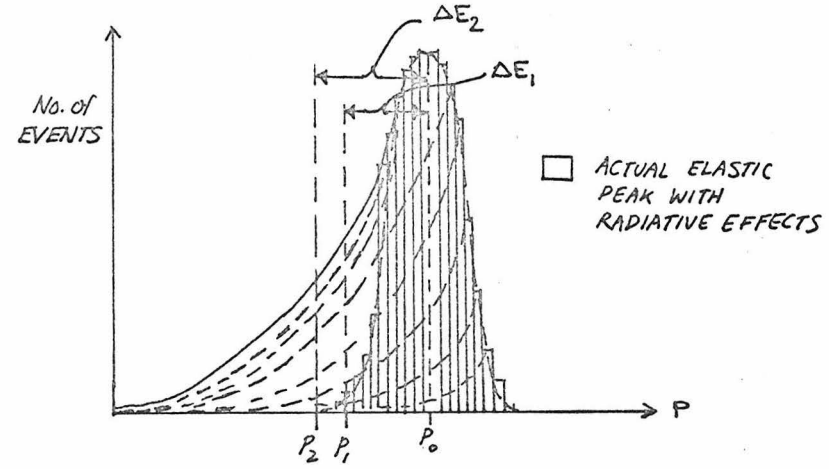

FIGURE 83: Actual Elastic Peak with radiative effects

Thus if we take p_1 very close to p_2, the function $e^{-\delta(\Delta E_2)} - e^{-\delta(\Delta E_1)}$ reproduces the shape of the radiative tail in Fig. 81 to within a constant factor.

However, the actual beam is not sharply defined in energy and the actual elastic peak will have a width even without radiative effects (cf. Section B, Chapter III, p.63), as is shown in Fig. 82. We can represent the shape of the elastic peak before radiative effects by a Gaussian:

$$\frac{1}{\sqrt{2\pi\sigma^2}} \; e^{-\frac{(P-P_o)^2}{2\sigma^2}}$$

p_e = center of elastic peak

σ = some width

To treat this case, we simply visualize the Gaussian as being a composite of a large number of delta function type elastic peaks (see Fig. 83) and sum the radiative tails from each peak. Then:

$$(N/Q)_{12} = \text{Const.} \sum_{\epsilon=-A}^{A} \left(e^{-\delta(\Delta E_2+\epsilon)} - e^{-\delta(\Delta E_1+\epsilon)} \right) e^{-\frac{\epsilon^2}{2\sigma^2}} F(\Delta E_1+\epsilon)$$

Where:

ϵ sum is in small increments $\lesssim \Delta E_2 - \Delta E_1$

$A \gtrsim 2\sigma$ in order to cover the wings of the distribution

$$F(x) = \begin{cases} 1 \text{ if } x>0 \\ 0 \text{ if } x\leq 0 \end{cases}$$

This factor is included to account for the fact there is no radiative contribution to momentum intervals at higher p than the elastic peak p

The actual expression used was:

$$\frac{(N/Q)_{12}}{\text{CONST.}} = \mathcal{F}^{\pm}(p) = \sum_{\epsilon=-25}^{25} \left(e^{-\delta^{\pm}(p+1+\epsilon)} - e^{-\delta^{\pm}(p+\epsilon)} \right) e^{-\frac{\epsilon^2}{2\sigma^2}} F(p+\epsilon)$$

Where: 2σ = 0.667·(Width of the experimental peak at half height - in p-bins)
This width was chosen by matching the theoretical and experimental widths for the leading edge of the elastic peak (leading edge being the high p side).

$\delta(p)$ = Meister and Yennie and bremmsstrahlung radiative correction

p = $\Delta E'$ in p-bin units (0.1% $\Delta p/p$ increments)

REFERENCES

1. M. N. Rosenbluth, Phys. Rev. 79, 615 (1950).

2. D. Yount and J. Pine, Phys. Rev. 128, 1842 (1962).

A. Browman, F. Liu, and C. Schaerf, Phys. Rev. 139,B1079 (1965).

R. L. Anderson et al., Phys. Rev. Letters 17,407 (1966).
Phys. Rev. 166, 1336 (1968).

G. Cassiday et al., Phys. Rev. Letters 19, 1191 (1967).

A. DeHollan, E. Engels, B. Knapp, and L. Hand, Paper 6a
Proceedings of the XIII Int. Conf. on High Energy Physics,
Berkeley (1966).

Bartel et al., Physics Letters 25B, 242 (1968).

Bouquet et al., Physics Letters 26B, 178 (1968).

3. H. Brechna, K. E. Breymayer, K. G. Carney, H. DeStaebler, R. H. Helm, and C. T. Hoard, The Stanford Two Mile Linear Accelerator, editor R. B. Neal (to be published, W. A. Benjamin Inc.), p. 545.

J. Pine, Stanford Linear Accelerator Center Internal Report No. TN-63-82 (1963).

4. G. A. Loew, O. H. Altenmueller, and R. R. Larsen, Rev. Sci. Instr. 35, 438 (1964).

5. J. J. Muray and R. A. Scholl, Stanford Linear Accelerator Center Internal Report No. TN-63-79 (1963).

6. R. L. Anderson, Stanford Linear Accelerator Internal Report No. TN-67 (June 1967).

7. R. S. Larsen and D. Horelick, Stanford Linear Accelerator Center Publication No. 398 (April 1968).

8. D. Yount, Nucl. Instr. Methods 52, 1 (1967).

9. R. E. Taylor, Proceedings of 1967 International Symposium on Electron and Photon Interactions at High Energy, Sept. 5-9, 1967 (SLAC), p.78.

L. Mo and C. Peck, Stanford Linear Accelerator Center Internal Report No. TN-65-29 (1965).

10. B. Richter, Proceedings of 1967 International Symposium on Electron and Photon Interactions at High Energy, Sept. 5-9, 1967 (SLAC), p.309.

L. Mo, Stanford Linear Accelerator Center Internal Report No. TN-65-40.

11. R. P. Feynman, Theory of Fundamental Processes (W. A. Benjamin Inc. 1962), p.133.

12. Y. S. Tsai, Phys. Rev. 122, 1898 (1961).

N. Meister and D. R. Yennie, Phys. Rev. 130, 1210 (1963).

13. Coward et al., Phys. Rev. Letters 20, 292 (1968).

14. N. Meister and D. R. Yennie, Phys. Rev. 130, 1210 (1963).

15. L. Hand and R. Wilson, 1963 Summer Study Report - Part 2, Stanford Linear Accelerator Center Report No. 25.

16. J. M. Jauch and F. Rohrlick, The Theory of Photons and Electrons (Addison-Wesley 1955) Sec. 12-4, p.263.

17. Theories considering two-photon enhancement due to N*(1238):

S. D. Drell and M. Ruderman, Phys. Rev. 106, 561 (1957).

S. D. Drell and S. Fubini, Phys. Rev. 113, 741 (1959).

N. R. Werthamer and M. A. Ruderman, Phys. Rev. 123, 1005 (1961).

18. Theories considering two-photon enhancement due to $J^{PC=1^{++}, 2^{++}}$ mesons:

D. Flamm and W. Kummer, Nuovo Cimento 28, 33 (1963).

S. D. Drell and J. D. Sullivan, Physics Letters 19, 516 (1965).

M. Gourdin, Recontre de Moriond sur les Interactions Electromagnetiques (Jan. 7-14, 1966), Comptes Rendus, Vol. II, p.139; and
Diffusion des electrons de haute energie (Masson et Cie, Paris), p.51.

19. J. Harte, University of California Radiation Laboratory Report No. UCRL-18083 (Feb. 1968).

20. Coward et al., Phys. Rev. Letters 20, 292 (1968).

21. H. W. Koch and J. W. Motz, Rev. of Mod. Physics 31, 920 (1959).